

1-1-2013

Pellet Cladding Mechanical Interactions of Ceramic Claddings Fuels Under Light Water Reactor Conditions

Bo-Shiuan Li
University of South Carolina

Follow this and additional works at: <https://scholarcommons.sc.edu/etd>



Part of the [Nuclear Engineering Commons](#)

Recommended Citation

Li, B.(2013). *Pellet Cladding Mechanical Interactions of Ceramic Claddings Fuels Under Light Water Reactor Conditions*. (Master's thesis). Retrieved from <https://scholarcommons.sc.edu/etd/2366>

This Open Access Thesis is brought to you by Scholar Commons. It has been accepted for inclusion in Theses and Dissertations by an authorized administrator of Scholar Commons. For more information, please contact digres@mailbox.sc.edu.

PELLET CLADDING MECHANICAL INTERACTIONS OF CERAMIC CLADDINGS
FUELS UNDER LIGHT WATER REACTOR CONDITIONS

by

Bo-Shiuan Li

Bachelor of Science
National Tsing Hua University, 2009

Submitted in Partial Fulfillment of the Requirements

For the Degree of Master of Science in

Nuclear Engineering

College of Engineering and Computing

University of South Carolina

2013

Accepted by:

Travis W. Knight, Major Professor

Elwyn Roberts, Reader

Lacy Ford, Vice Provost and Dean of Graduate Studies

© Copyright by Bo-Shiuan Li, 2013
All Rights Reserved.

DEDICATION

I dedicated this thesis to all whom I loved.

ACKNOWLEDGEMENTS

I would like to thank my advisor, Dr. Travis Knight, for supporting me entirely through this research and greatly inspires me as an advisor. I would like to pay my utmost gratitude to Dr. Elwyn Roberts. Through our frequent meetings, his role as a thesis reader provided me with his valuable knowledge of fuel rod performances. None of this would have been possible without Ian's help with coding and the encouragement from my colleagues at USC, Seung-Min, Kallie, Kyle, Jimmy, David, Luke and Dillon.

I would like to thank Dr. Djamel Kaoumi, for giving me the opportunity to work with IVEM, which had broadened my horizon on nuclear material research. Warm accommodation provided by Chya-Yan had made my several visits to Argonne/Chicago by far the best experience I had.

I received many helps from my Taiwanese colleagues at USC, all helps were greatly appreciated. Many thanks to my friends at Taiwan, whom had support me through Facebook and LINE. Owe to the omnipresent internet, loneliness is greatly eased when smartphone is in hand. Conny's enthusiasm toward research had truly motivated me to advance my studies to a higher level.

No words will be enough to express my gratitude toward my family. I love y'all. Thank you Cool Bean for providing my everyday coffee at a fair price. Please support your local barista!!

ABSTRACT

Ceramic materials such as silicon carbide (SiC) are promising candidate materials for nuclear fuel cladding and are of interest as part of a potential accident tolerant fuel design due to its high temperature strength, dimensional stability under irradiation, corrosion resistance, and lower neutron absorption cross-section. It also offers drastically lower hydrogen generation in loss of coolant accidents such as that experienced at Fukushima.

With the implementation of SiC material properties to the fuel performance code, FRAPCON, performances of the SiC-clad fuel are compared with the conventional Zircaloy-clad fuel. Due to negligible creep and high stiffness, SiC-clad fuel allows gap closure at higher burnup and insignificant cladding dimensional change. However, severe degradation of SiC thermal conductivity with neutron irradiation will lead to higher fuel temperature with larger fission gas release.

High stiffness of SiC has a drawback of accumulating large interfacial pressure upon pellet-cladding mechanical interactions (PCMI). This large stress will eventually reach the flexural strength of SiC, causing failure of SiC cladding instantly in a brittle manner instead of the graceful failure of ductile metallic cladding. The large interfacial pressure causes phenomena that were previously of only marginal significance and thus ignored (such as creep of the fuel) to now have an important role in PCMI. Consideration of the fuel pellet creep and elastic deformation in PCMI models in FRAPCON provide

for an improved understanding of the magnitude of accumulated interfacial pressure.

Outward swelling of the pellet is retarded by the inward irradiation-induced creep, which then reduces the rate of interfacial pressure buildup. Effect of PCMI can also be reduced and by increasing gap width and cladding thickness. However, increasing gap width and cladding thickness also increases the overall thermal resistance which leads to higher fuel temperature and larger fission gas release. An optimum design is sought considering both thermal and mechanical models of this ceramic cladding with UO_2 and advanced high density fuels.

TABLE OF CONTENTS

DEDICATION	iii
ACKNOWLEDGEMENTS	iv
ABSTRACT	v
LIST OF TABLES	ix
LIST OF FIGURES	x
LIST OF ABBREVIATIONS	xiv
I. INTRODUCTION	1
1.1 MOTIVATION	1
1.2 OBJECTIVES	2
II. LITERATURE REVIEW	5
2.1 SILICON CARBIDE	5
2.2 CLADDING DESIGNS	8
2.3 FUEL PERFORMANCE CODE: FRAPCON	12
2.3 OTHER FRAPCON MODIFICATIONS	16
III. METHODOLOGY	21
3.1 SiC MATERIAL PROPERTIES MODELING	21
3.2 OTHER SiC PROPERTIES	39
3.3 PELLET CLADDING MECHANICAL INTERACTIONS	43
3.4 SOFT PELLET MODEL	51
IV. RESULTS AND DISCUSSION	60
4.1 LOW BURNUP TEST CASE	60
4.2 HIGH BURNUP TEST CASE	74
4.3 IMPROVED MODELING OF HOOP STRESS & MODIFIED ROD DESIGN	84

V.	CONCLUSIONS.....	89
	5.1 MONOLITHIC SiC CLADDING MODELING.....	90
	REFERENCES	94

LIST OF TABLES

Table 2.1 Thermal neutron absorption cross-section of selected elements	9
Table 3.1 Material properties of monolithic SiC and Zircaloy at room temperature	21
Table 4.1 Initial fuel and cladding dimensions for both cladding design	61
Table 4.2 Comparison for soft/hard contact in Zircaloy/SiC clad fuel rods	78
Table 4.3 Modified fuel rod dimensions	85
Table 4.4 Fuel radial displacement at EOL consider the soft-pellet model	88
Table 5.1 Modeled material properties and their governing parameter	90
Table 5.2 Results of PCMI mitigation	93

LIST OF FIGURES

Figure 1.1 Major concerns of accident tolerant fuel design.....	2
Figure 1.2 Pellet cladding mechanical interactions of Zircaloy cladding.....	3
Figure 2.1 Monolithic and Triplex SiC cladding tube	6
Figure 2.2 Westinghouse Duplex SiC cladding tube... ..	6
Figure 2.3 Crystal structure of (a) α -SiC (b) β -SiC	7
Figure 2.4 Tetrahedral arrangement of Si and C atoms	8
Figure 2.5 Binary phase diagram of SiC.....	8
Figure 2.6 Schematic design of a LWR fuel rod	10
Figure 2.7 Cross-section of a monolithic SiC cladding design.....	10
Figure 2.8 Cross section of a Duplex SiC cladding design.....	11
Figure 2.9 Cross section and SEM cross section of the Triplex SiC cladding design.....	12
Figure 2.10 Simplified FRAPCON-3.4 solution flowchart	14
Figure 2.11 Schematic of fuel rod temperature distribution	15
Figure 2.12 (a) pellet/cladding at open-gap regime and (b) at closed-gap regime with voids originally in the gap relocate into pellet cracks.....	15
Figure 2.13 Schematic of the I&EC sintered annular pellet design.....	17
Figure 2.14 Schematic of the I&EC VIPAC annular pellet design	18
Figure 2.15 Fission gas release for FRAPCON based on the Manzel test	19
Figure 3.1 Thermal conductivity of SiC at elevated temperatures.	23

Figure 3.2 Thermal conductivity degradation of CVD SiC due to neutron irradiation at room temperature.....	24
Figure 3.3 Thermal conductivity of SiC at room temperature in the void-swelling saturable and non-saturable regime	24
Figure 3.4 Thermal conductivity of un-irradiated SiC and Zircaloy vs. temperature.....	26
Figure 3.5 Thermal conductivity of irradiated SiC at room temperature	26
Figure 3.6 Thermal expansion coefficient of SiC vs. temperature	28
Figure 3.7 Thermal expansion coefficients vs. temperature: SiC & Zircaloy	28
Figure 3.8 Linear irradiation-induced swelling strain of SiC vs. DPA.....	30
Figure 3.9 Porosity effect vs. SiC elastic modulus	31
Figure 3.10 Modeling of SiC elastic modulus as a function of porosity	31
Figure 3.11 Temperature effect vs. SiC relative elastic modulus	33
Figure 3.12 Irradiation-induced swelling vs. elastic modulus reduction of CVD SiC. Dotted line is the estimated influence of lattice relaxation on elastic modulus using Tersoff potential.....	33
Figure 3.13 Elastic modulus degradation of SiC & Zircaloy vs. temperature.....	34
Figure 3.14 Maximum flexural strength of monolithic SiC tube.....	35
Figure 3.15 Flexural strength increase as a function of dpa	35
Figure 3.16 Flexural strength of SiC vs. dpa: normalized to un-irradiated strength	36
Figure 3.17 Effect of porosity vs. SiC hardness	38
Figure 3.18 Temperature effect on SiC hardness.....	38
Figure 3.19 Thermal/irradiation induced steady-state creep rate vs. stress at 600K	41
Figure 3.20 Total steady-state creep rate vs. effective stress at 600 K.....	41
Figure 3.21 Cross-sectional view of the pellet evolution during operation.....	44
Figure 3.22 Calculated crack patterns from thermal-induced stress.....	45

Figure 3.23 Radial temperature distribution in a BWR rod at BOL modeling with and without fuel relocation	45
Figure 3.24 Experimental data of % of pellet-cladding gap closure during irradiation	46
Figure 3.25 FRAPCON modeled gap change $\frac{\Delta G}{G}$ as a function of power and burnup	47
Figure 3.26 Gap model showing the relationship between gap width and rod power	49
Figure 3.27 Stiffness recovery model of pellet with cracks.....	50
Figure 3.28 Elastic modulus of UO ₂ as a function of temperature	53
Figure 3.29 Cladding at closed-gap	54
Figure 3.30 Interfacial pressure exerted on pellet at closed-gap	57
Figure 3.31 Flow chart of the soft-pellet model solution scheme.....	57
Figure 3.32 Creep of UO ₂ vs. temperature.....	58
Figure 3.33 Interfacial pressure vs. burnup of the rigid-pellet and soft-pellet model	59
Figure 4.1 Linear heat generation rate vs. time	62
Figure 4.2 Average burnup vs. time.....	62
Figure 4.3 Cladding thermal conductivity degradation vs. burnup	63
Figure 4.4 Cladding inner/outer surface temperature vs. burnup	64
Figure 4.5 Fuel centerline/surface temperature vs. burnup.....	64
Figure 4.6 Gap gas pressure vs. burnup.....	65
Figure 4.7 Gap width & interfacial pressure vs. burnup.....	66
Figure 4.8 Cladding hoop stress vs. burnup.....	67
Figure 4.9 Cladding hoop strain vs. burnup.....	68
Figure 4.10 Fuel surface pressure vs. burnup	69
Figure 4.11 Fuel pellet elastic deformation due to fuel surface pressure	70
Figure 4.12 UO ₂ steady-state creep rate vs. 1/T.....	71

Figure 4.13 Fuel swelling rate using rigid and soft pellet model vs. burnup.....	71
Figure 4.14 Fuel radial displacement using rigid and soft pellet model vs. burnup	72
Figure 4.15 Linear heat generation rate vs. time	75
Figure 4.16 Average burnup & fission gas release vs. time	75
Figure 4.17 Degradation of thermal conductivity vs. burnup	76
Figure 4.18 Gap width & interfacial pressure vs. burnup	78
Figure 4.19 Cladding hoop stress vs. burnup.....	79
Figure 4.20 Cladding hoop strain vs. burnup.....	79
Figure 4.21 Gap width & fuel radial displacement vs. burnup	80
Figure 4.22 Fuel surface pressure vs. burnup	81
Figure 4.23 Fuel elastic strain vs. burnup	82
Figure 4.24 UO ₂ steady-state creep rate vs. 1/T	83
Figure 4.25 Fuel radial displacement using the rigid/soft pellet model vs. burnup.....	83
Figure 4.26 Interfacial pressure vs. burnup using thicker cladding	85
Figure 4.27 Hoop stress vs. burnup using thicker cladding.....	86
Figure 4.28 Fuel centerline temperature vs. burnup using thicker cladding.....	87
Figure 5.1 Two creep mechanisms for cladding hoop stress mitigation.....	93

LIST OF ABBREVIATIONS

ATF	Accident Tolerant Fuel
PCMI.....	Pellet Cladding Mechanical Interaction
UO ₂	Uranium Dioxide
SiC.....	Silicon Carbide
LWR.....	Light Water Reactor
LOCA.....	Loss of Coolant Accident
NRC	Nuclear Regulatory Commission
CVD	Chemical Vapor Deposition
PNNL	Pacific Northwest National Laboratory
EBC.....	Environmental Barrier Coating
I&EC	Internal and External Cooled
VIPAC.....	Vibration Packed
DNBR	Departure from Nucleate Boiling Ratio
DPA.....	Displacement per Atom
MOX	Mixed Oxide
BOL.....	Beginning of Life
EOL.....	End of Life
MPa/GPa	Mega/Giga Pascal
DBTT	Ductile to Brittle Transition Temperature
MATPRO.....	Material Database for Fuel Performance Modeling

GWD/MTUGigawatt Day per Metric Ton Uranium
Crud..... Chalk River Unidentified Deposit
LHGR..... Linear Heat Generation Rate
PWR.....Pressurized Water Reactor
FGR..... Fission Gas Release

CHAPTER I

INTRODUCTION

1.1 Motivation

The long history of zirconium cladding design fuel has provided the nuclear industry with reliable power generation and considerable low risk of fuel failures. However, after three major nuclear accidents: Three Mile Island, Chernobyl, and Fukushima Daiichi, the research and development of the nuclear industry for fuel rods has aimed toward the accident tolerant fuel (ATF), which has higher safety margin that is capable of enduring longer time under a loss of coolant accident scenario (LOCA), and also maintaining or even improving its performance during normal operations [1].

Interests had been drawn to ceramic cladding materials, one of the most promising candidate cladding materials for new light water reactor (LWR) fuel design is silicon carbide (SiC), mainly due to its high temperature strength, dimensional stability under irradiation, and better corrosion resistance compared to the conventional zirconium-based cladding. However, the brittle nature of ceramic material is a major drawback which may limit its usage after the contact of pellet and cladding. In addition, the significant degradation of thermal conductivity under irradiation may also deteriorate its performance [2]. Considering all issues, investigations are necessary to assess the performance of ceramic cladding designed fuel before applying it to practical use.

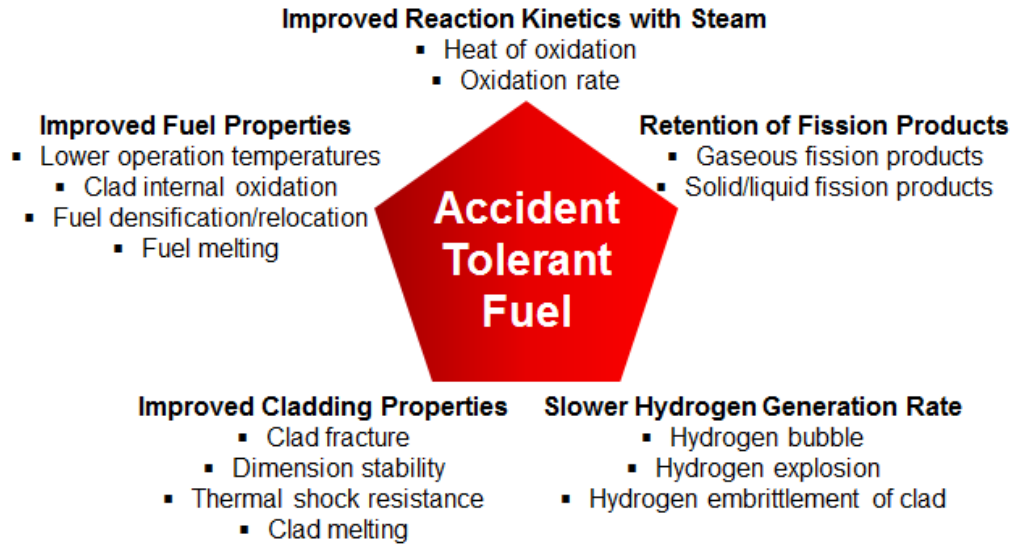


Figure 1.1 Major concerns of accident tolerant fuel design [1]

1.2 Objectives

The objective of this research is to investigate the pellet-cladding mechanical interactions (PCMI) of advanced ceramic claddings with ceramic fuels. PCMI creates significant interfacial pressure that deforms the ductile metallic cladding plastically shown in **Fig. 1.1.2**. For ceramic cladding that possesses higher stiffness, this disastrous deformation may be insignificant.

Monolithic SiC-clad fuel is used for the PCMI investigation. Due to the differences in material properties, the effect of PCMI may have large discrepancy between metallic and ceramic cladding. The performance of monolithic SiC cladding designed fuel under must therefore be evaluated, by using the Nuclear Regulatory Commission (NRC) validated fuel performance code, FRAPCON-3.4 [3]. This work is accomplished through four steps.

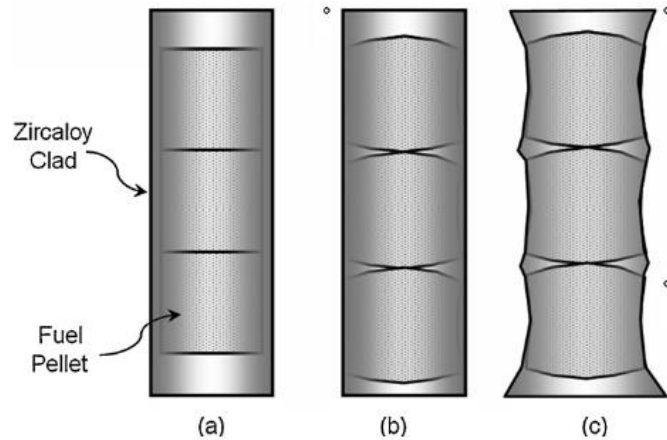


Figure 1.2 Zircaloy cladding deformation after PCMI [4]

(a) Implementation of SiC thermal and mechanical properties:

FRAPCON-3.4 only allows the user to choose cladding materials from a selection of zirconium-based alloys. High-purity, monolithic SiC material properties (thermal and mechanical) are implemented into the material module.

(b) Modification of pellet-cladding deformation models:

FRAPCON-3.4 uses a rigid pellet model (FRACAS-I) for pellet-cladding mechanical calculations. It neglects all stress-induced deformations of the pellet. For the magnitude of interfacial pressure created and the ductile nature of Zircaloy claddings, this rigid pellet model may give a reasonable approximation. For ceramic SiC cladding with higher interfacial pressure and brittle nature, this model may fail to capture important behaviors. Therefore, the “soft-pellet” model is developed in this work.

(c) Fuel performance simulation under LWR condition:

With the implementation of SiC material properties, the newly developed FRAPCON-USC can now estimate the fuel performance of SiC-clad fuel. Two testing cases: low and high-burnup under LWR conditions was used to compare the performance

of SiC-clad fuel with the conventional Zircaloy-clad fuel. The results will show the advantages and disadvantages of SiC-clad fuel.

(d) Evaluation of the soft-pellet model

Although not implemented into FRAPCON-USC, the significance of stress-induced pellet deformations such as elastic deformation and creep may rise due to the PCMI-created large interfacial pressure. Evaluations and simple calculations are made to estimate its significances to the hoop stress accumulated on the ceramic cladding.

CHAPTER II

LITERATURE REVIEW

2.1 Silicon Carbide

2.1.1 Silicon Carbide

Silicon carbide has been considered for application in high temperature, high irradiation environments since first investigated by Rovner and Hopkins for nuclear applications [5]. It has also been considered as a structural coating on fuel kernels for high-temperature gas-cooled reactor for many years [6], and as an inert matrix for fuel pellets [7]. SiC has several advantages over the conventional zirconium-based alloys. It possesses better dimensional stability under irradiation, more resistant to corrosive environment, moderate degradation of mechanical properties at elevated temperatures, insignificant creep rate at high temperature, and better neutron efficiency by having lower neutron absorption cross section [8].

One of the main obstacles preventing the application of SiC as a structural material is its brittle behavior, as it cannot dissipate accumulated stresses after PCMI through plastic deformation and creep. As a result, SiC does not demonstrate the graceful failure mechanism like a ductile metal does. It fractures immediately once the hoop stress reaches the flexural strength [9]. Another concern is the severe degradation of SiC thermal conductivity with irradiation. Stoichiometric SiC possesses excellent thermal conductivity as-fabricated, but rapidly degrades to a much lower thermal conductivity as

it reaches the saturation dose. This undesired property is due to the accumulation of irradiation-induced defects [10].

2.1.2 Silicon Carbide Composites

In order to make practical use of SiC as structural materials, additional strength and flexibility are provided by woven SiC fibers. The composite consists of SiC fibers arranged parallel or braided, bonded together with a chemical vapor deposited (CVD) SiC matrix. The fibers provide strength and the ability to withstand localized fractures without completely failing the structure, while the matrix serve as a hermetic seal to keep in all fission products. **Fig. 2.1** and **2.2** show the monolithic, Duplex, and Triplex SiC cladding tube [11, 12]



Figure 2.1 Monolithic SiC tube (left) and Triplex SiC tube (right) [11]

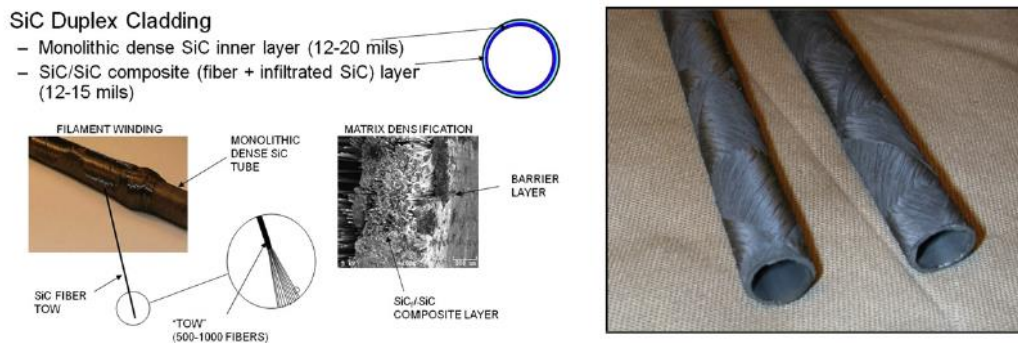


Figure 2.2 Westinghouse Duplex SiC cladding tube [12]

2.1.3 Crystal Structure

The material properties of silicon carbide strongly relate to its crystal structure. The large number of polytypes (over 200 crystal structures) also increases its complexity. Various polytypes is a result from the different stacking of bilayers, shown in **Fig. 2.3** [13]. Rhombohedral and hexagonal SiC polytypes are called α -SiC, where cubic polytype is called β -SiC. In **Fig. 2.4**, a tetrahedral arrangement of Si and C atoms indicates the crystal structure of β -SiC.

The bonds between the Si and C atoms have a primarily covalent nature, with slightly ionic bonding characteristics due to silicon's higher electronegativity. The most stable SiC structure is comprised of Si and C in a stoichiometric (1:1) amounts, because of its dominating covalent bonding. For stoichiometric SiC, phase stability is strongly related to temperature. The cubic structure of β -SiC is more stable than other type of structures under 2273 K, where α -SiC dominates at higher temperature as illustrated in **Fig. 2.5** [14].

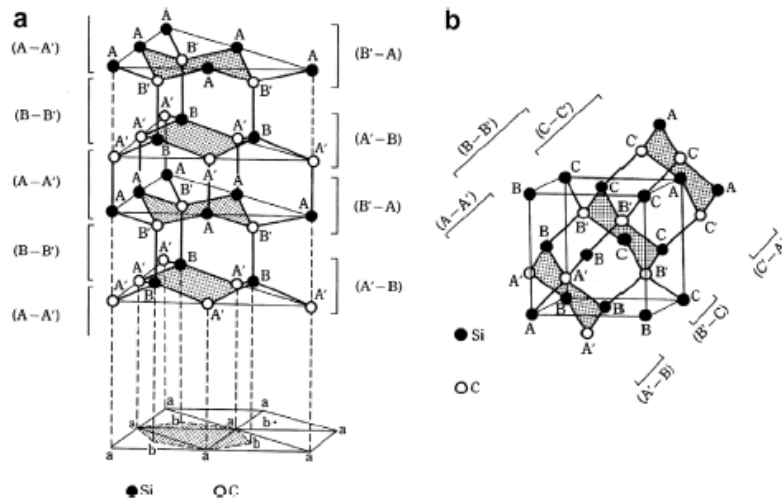


Figure 2.3 Crystal structure of (a) α -SiC (b) β -SiC [13]

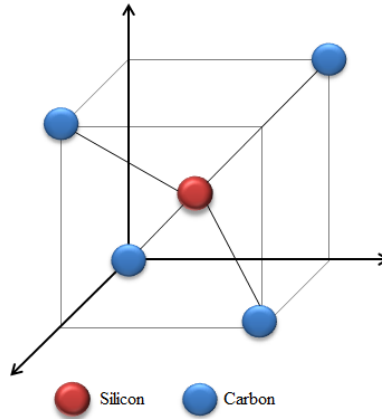


Figure 2.4 Tetrahedral arrangement of Si and C atoms

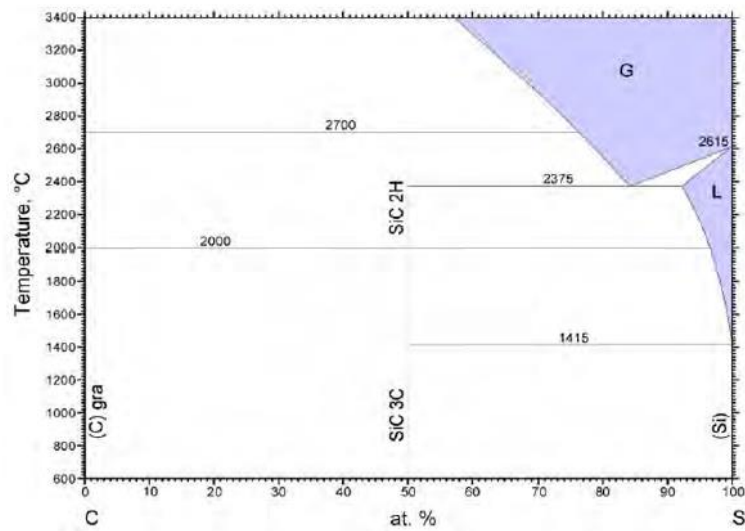


Figure 2.5 Binary phase diagram of SiC [14]

2.2 Cladding Designs

2.2.1 Zirconium Alloy Cladding

Zirconium-based cladding has been adapted universally in the fuel rod designs of current commercial LWRs, based on a combination of desirable properties, e.g., high mechanical strength, high melting temperature (1852°C), good corrosion resistance, and particularly the low thermal neutron absorption cross-section, which can translate directly

into neutronic economy. To support this beneficial feature, **Table 2.1** shows various thermal neutron absorption cross-sections of selected elements. Minor amounts of alloying elements are added to optimize the properties of cladding, i.e. Sn, Fe, Cr, Nb, and Ni. The addition of those elements enhances the cladding performance by the formation of intermetallic precipitates and secondary phase particles.

The issues of material properties degradation of cladding will become more detrimental if nuclear vendors were to extend the lifetime of current design cladding. The excessive hydrogen pickup of zirconium cladding will lead to the precipitation of zirconium hydrides. These hydrides have a poor mechanical strength and are brittle at room temperature, causing degradation of the mechanical strength and ductility. Accumulation of irradiation-induced dislocation loop and dissolution of secondary phase particle will also greatly influence the in-reactor performance of cladding. Therefore, to extend the lifetime and burnup of current fuel rods, new types of cladding materials will be needed.

Table 2.1 Thermal neutron absorption cross-section of selected elements

Examples of the absorption cross-section for thermal neutrons.

Element	Z	Cross-section for absorption (10^{-28} m ² /atom)
O	8	0.0002
C	6	0.003
Be	4	0.01
Zr	40	0.2
Si	14	0.2
Al	13	0.2
Pb	82	0.2
H	1	0.3 (² H: 0.0005)
Fe	26	2.6
Cr	24	3.1
Ni	28	4.5
Ag	47	63
Li	3	71
In	49	190
B	5	760
Cd	48	2400
¹⁵⁷ Gd	64	250,000
²³⁵ U	92	545 (fission), 100 (capture)

2.2.2 SiC Monolithic Cladding

Chemical vapor deposition (CVD) is one of the most favorable processing methods for SiC in nuclear applications, because of its capability to produce high density, purity, and crystalline structure [13]. Due to its advantages, the CVD method was applied to process the β -SiC matrix in the monolithic cladding. Schematic design of a typical LWR fuel rod is shown in **Fig. 2.6**. The cross section of a monolithic SiC cladding fuel rod is shown in **Fig 2.7**, where the dense SiC monolith layer acts as the hermetic layer for fission products.

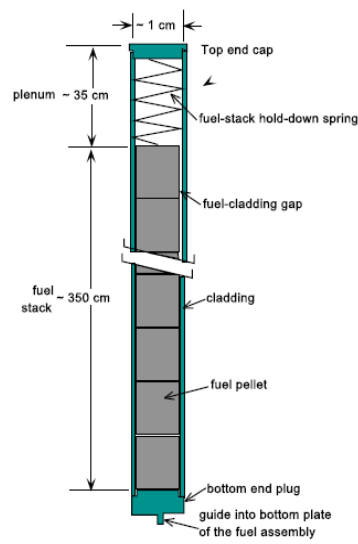


Figure 2.6 Schematic design of a LWR fuel rod [15]

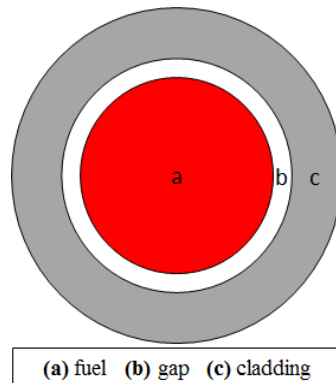


Figure 2.7 Cross-section of a monolithic SiC cladding design

2.2.3 SiC Duplex Cladding

Gamma Engineering, in collaboration with MIT, have investigated the application of SiC as a fuel cladding material for LWRs. They adapt the duplex design concept shown in **Fig.2.8** that combines SiC monolith with SiC/SiC woven fibers to create a composite duplex cladding where the Zircaloy cladding is replaced [16]. The inner monolithic SiC layer provides the hermetic seal necessary to maintain structure stability of cladding and to contain the radioactive fission products. The outer composite is formed by SiC fibers woven around the monolith, and infiltrated with carbon-rich vapor to form a SiC matrix, bonding the fiber and monolith together. The composite layer provides additional strength to the cladding, and mitigates the propagation of cracks by allowing fibers to slide a small distance after matrix cracking occurs.

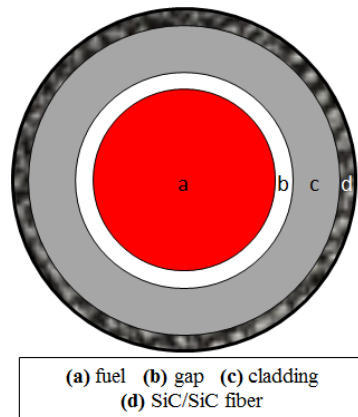


Figure 2.8 Cross section of a Duplex SiC cladding design

2.1.3.3 SiC Triplex Cladding

Recent developments of advanced SiC cladding at MIT have progressed toward the three-layered Triplex design [2], shown in **Fig 2.9**. It consists three functional layers: the monolithic SiC layer, the composite layer woven with SiC fiber, and the new outer environmental barrier coating (EBC) layer. The EBC is a thin coating (50~150 μm) at the

outmost of the cladding to provide additional protection from corrosion. Studies have shown that, when loaded internally, the composite and EBC shared 21.6% ~ 37% of the total hoop stress [17]. However, the monolith is still the primary bearer of the stresses.

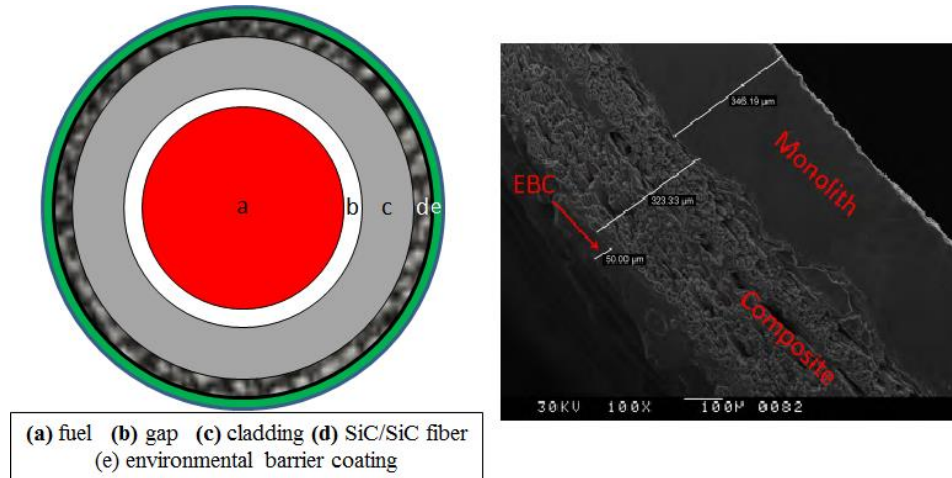


Figure 2.9 Cross section and SEM cross section of the Triplex SiC cladding design

2.3 Fuel Performance Code: FRAPCON-3.4

2.3.1 Motivation of developing fuel performance code

The fuel element in a LWR is a rather simple object; however, it gets more complicated as material properties degrade during reactor service life. These changes include the dimensions and the material properties in both fuel pellet and cladding. Will the fuel elements able to serve its primary function, which is to generate power without failure? The ability to accurately predict the performance of fuel rods under extended service life is the major objective of nuclear vendors and regulatory for both economic and safety issues.

To achieve this goal, the U.S. Nuclear Regulatory Commission (NRC) has sponsored an extensive program for analytical computer code development. The steady-state fuel performance code, FRAPCON, was developed by the Pacific Northwest

National Laboratory (PNNL) to estimate the performance of a single fuel rod, and most important of all, to determine the integrity (safety margins established by NRC) of fuel rods during operation [3].

2.3.2 Code structure

FRAPCON calculates the performance of a single fuel rod under LWR condition when initial fuel and cladding geometry, fuel enrichment, coolant condition, neutron flux, power history, and axial power shape are inputted. It also allows the user to specify the mesh size radially and axially for FRAPCON's finite calculations of pellet heat conduction and fission gas release. FRAPCON takes these inputs and uses material properties of the specified fuel and cladding types (fuel: UO_2 and MOX, cladding: Zircaloy-2, Zircaloy-4, Zirlo, M5) that are given in the material database [18]. **Fig. 2.10** is a simplified flowchart of FRAPCON-3.4, showing its iterative calculation procedures.

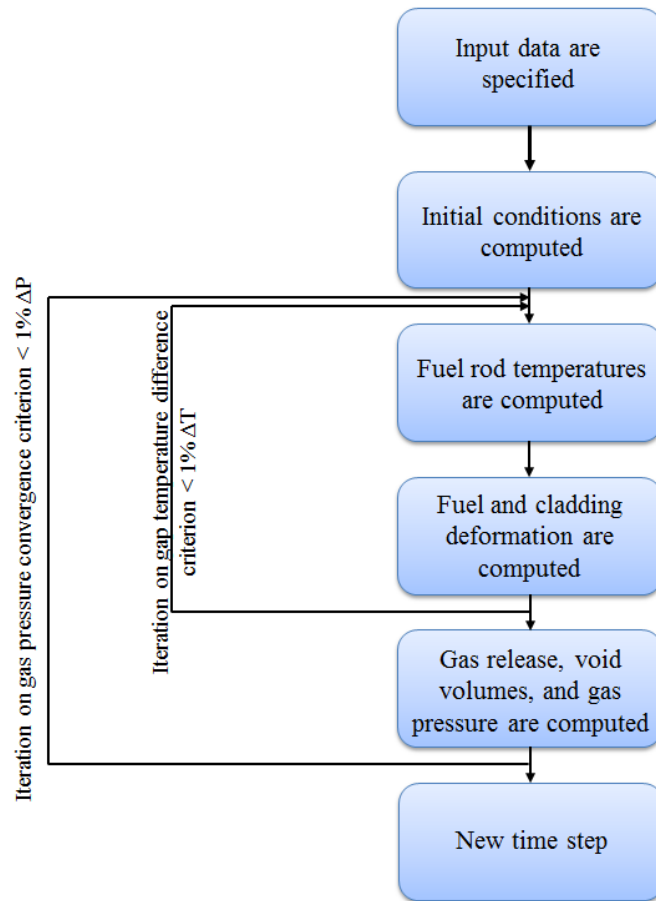


Figure 2.10 Simplified FRAPCON-3 solution flowchart [3]

2.3.3 Thermal-mechanical coupling

The coupling of thermal and mechanical modeling is very important because it will determine the existence of the fuel-cladding gap. The gap thermal conductance depends on its width and therefore changes the temperature distribution throughout the fuel and cladding shown in **Fig. 2.11**. Due to UO_2 's low thermal conductivity, temperature gradient will induce high level of thermal stresses, eventually cracks the fuel into fragments and relocate. Void space that originally exists as the gap is then relocated into the fuel as pellet fragment jumps outward.

The relocation model provides a modified fuel-cladding gap size by considering the shift of voids from gap into cracks in the fuel pellet shown in **Fig. 2.12** for more realistic fuel thermal and mechanical calculations. After 50% of the relocated volume is recovered, FRAPCON then assumes the pellet to be a rigid structure, and therefore, hard-contact occurs between the fuel and cladding.

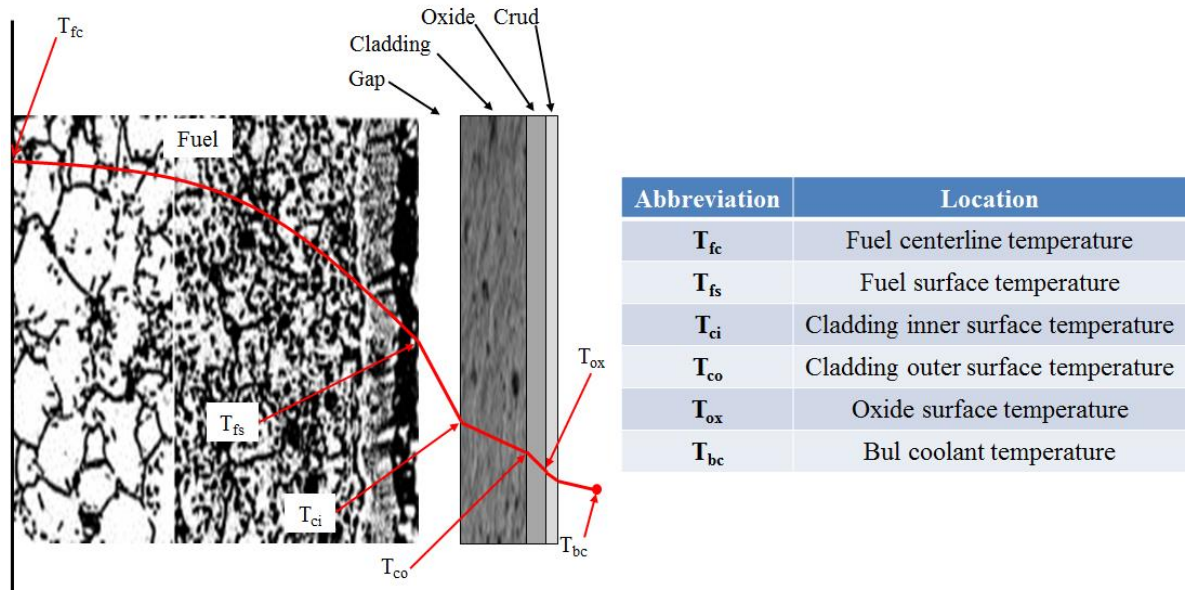


Figure 2.11 Schematic of fuel rod temperature distribution [3]

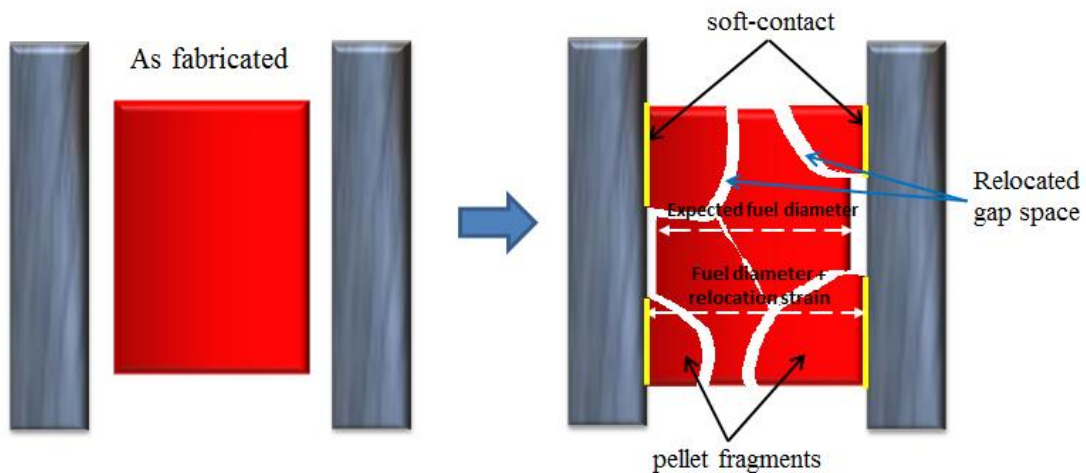


Figure 2.12 (a) pellet/cladding at open-gap regime and (b) at closed-gap regime with voids originally in the gap relocate into pellet cracks

2.4 Other FRAPCON Modifications

2.4.1 Implementation of internally and externally-cooled annular fuel rods

The concept of creating an annular fuel pellet with central void for better fission heat removal was first investigated by Caner et al. [19]. The benefit of reducing the fuel temperature is to reduce the fission gas release, swelling, and chances of overheating. However, the function of central void is limited because heat can only be removed through the outer surface of the pellet, and it creates a channel for fuel and debris relocation.

Recently, MIT had developed an internally and externally-cooled (I&EC) annular fuel rod design [20], which creates an open channel through the center of the fuel to allow removal of heat at the inner surface of fuel rod. One method to utilize the I&EC annular fuel rod is through the sintered annular pellet. Annular pellets can be manufactured to achieve the same density as the standard pellets, but are more difficult to process due to their fine dimensions. The asymmetry of the pellet-cladding gap rise another concern [21]. The outer gap closes first, causing larger gap conductance at the fuel's outer surface. As a result, the heat flux through the fuel rod's outer diameter will increase, which reduce the departure from nucleate boiling ratio (DNBR). Three possible methods can be done to alleviate this problem: **(1)** increase the initial radial gap, **(2)** decrease the thermal conductivity of the outer gap, and **(3)** decrease the inner gap [20].

FRAPCON was modified by Yuan et al. [22] to model the performances of I&EC annular fuel rods with Zircaloy cladding and sintered annular pellets, which is shown in **Fig. 2.13** The modifications were focused on adding parameters for the simultaneous

calculations of the inner and outer cladding surface heat removal and also on the various fuel behaviors, where previously only the outer surface was of concern.

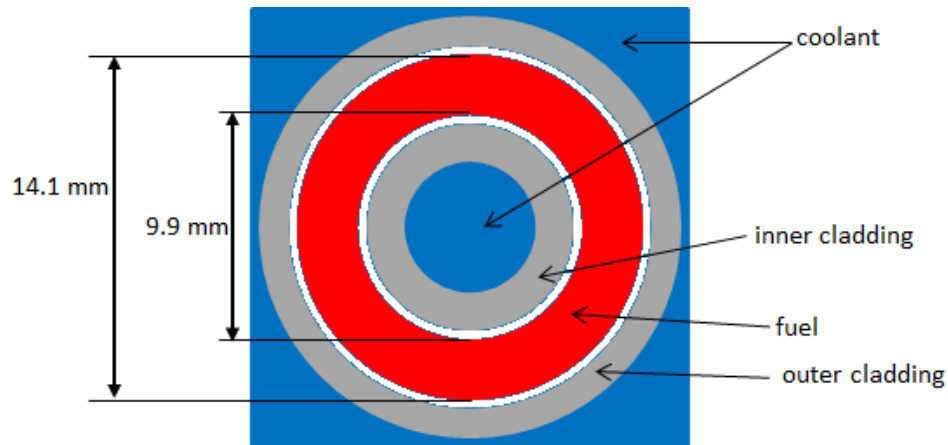


Figure 2.13 Schematic of the I&EC sintered annular pellet design [22]

2.4.2 Implementation of the Vibration Packed Fuel (VIPAC)

Another new concept of fuel design adapted is the Vibration Packed (VIPAC) fuel [23]. It can be manufactured by crushing the fuel into shards, and then compacted into the fuel rods via vibration and compressive impacts.

The main advantages of VIPAC fuel, as shown in **Fig. 2.14**, are easy loading and simple fuel manufacturing. These factors can improve the economic values of VIPAC fuel. Lack of fuel-cladding gap means the initial thermal resistance at the gap interfaces is greatly reduced. Due to its annular design, the asymmetry problem of earlier outer gap closure is found again. VIPAC fuel also shows fewer responses with chemical and mechanical interaction.

The main difficulty with VIPAC is to achieve acceptable fuel smear density. High density of fuel brings the benefits of maximizing fuel loading and higher thermal conductivity. Current VIPAC fabrication is able to achieve up to 86% of theoretical

density. It is possible that the density could further be increased through a selection of grain size, grain mixing ratios, and powdered uranium metal.

VIPAC fuel is also implemented into modified FRAPCON, which already has the I&EC annular fuel design. The major differences in modeling the annular VIPAC fuel rods performances are: (1) the pellet/clad gaps are always closed, (2) radial relocation of fuel is removed, and the (3) thermal expansion contracts the inner annulus diameter but expands the outer diameter.

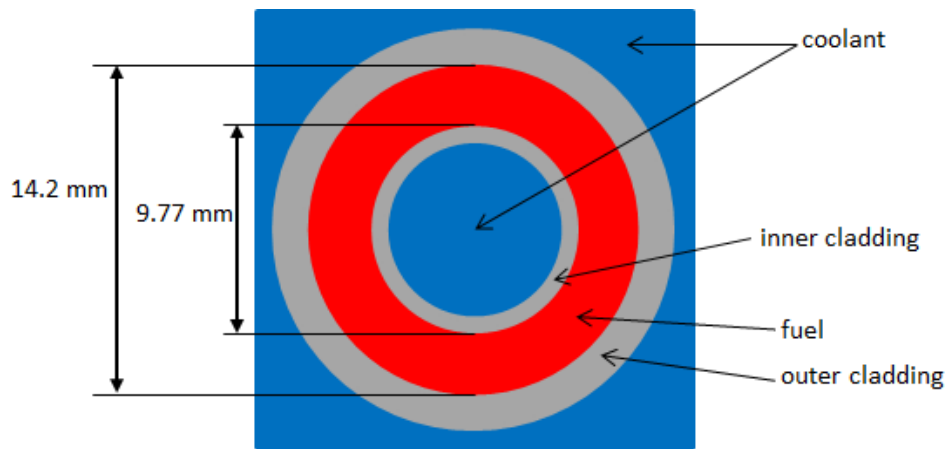


Figure 2.14 Schematic of the I&EC VIPAC annular pellet design [23]

2.4.3 Implementation of the high-burnup fission gas release model

The validated maximum burnup for FRAPCON is 62 MWd/kgU [3]. This burnup limit is based on the experimental data under this condition. This burnup limit may be sufficient for current fuel rods in LWRs, but future investigations are interested in the extension of maximum burnup because of applying stronger cladding materials and improved fuel rod designs. To achieve these objectives, modifications are necessarily for current FRAPCON in order to allow modeling of LWR fuel rods performance at a higher burnup.

Modifications of FRAPCON by Long et al [24] investigated the fission gas release of fuel rod at very high burnup as shown in **Fig. 2.15**. Because fission gas release is considered to be the key parameter for fuel rod performance at high burnup. This new fission gas release model treats the buildup of fission gases at the rim region of the pellet, and adds a threshold fission gas release that is caused by gas saturation at high burnup. These modifications were made to adjust the current UO_2 fission gas release model with the actual phenomenon of fission gas release at high burnup, therefore, the updated model is more capable of predicting fission gas release accurately. Overall, the threshold release model replaces the standard linear athermal model, with an exponential fission gas release model at higher burnup.

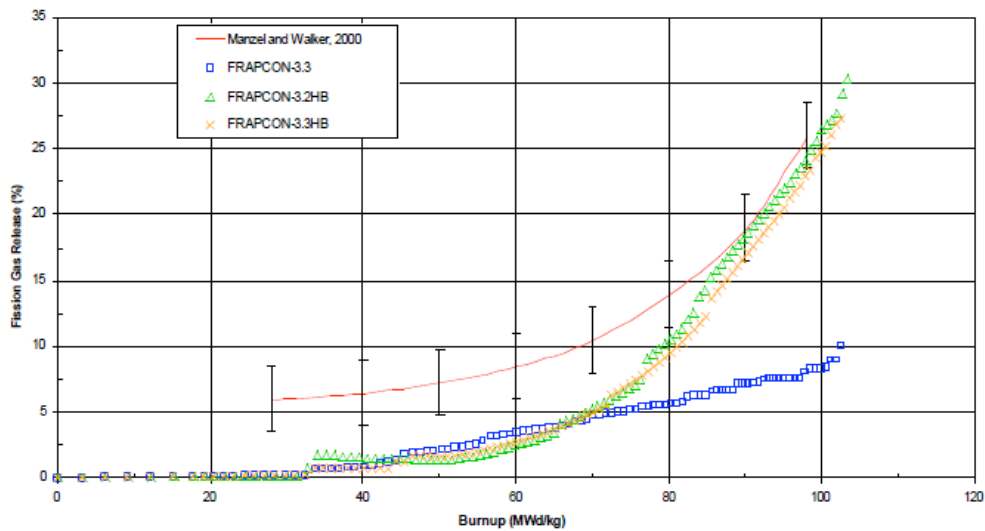


Figure 2.15 Fission gas release for versions of FRAPCON based on the Manzel test [24]

2.4.4 Implementation of the SiC Duplex cladding model

SiC has been initially investigated for applications in gas-cooled fission reactor, and the first wall of fusion reactor. Since then, large numbers of experiments have been conducted to measure the material properties of SiC its composites under reactor

conditions. This information can be compiled to obtain the their relationships [13]. In FRAPCON, each material property is governed by an individual subroutine, so experimental results fit quite well with the existing code structure.

To simplify the complexity of adding another coaxial composite cladding layer into FRAPCON's solution scheme, the monolithic and composite layers of the duplex cladding was treated as one homogeneous material in the modeling by Carpenter et al. [16]. The modeling adapts the material properties of the SiC/SiC composite because it provides the cladding with the ability to liberate the accumulated excessive stresses from PCMI and possesses similar properties but less stiffness compare to monolithic SiC. This approach minimizes the modifications that are needed to the code, and provide an estimation of the cladding performance of the Duplex SiC-clad designed fuel rods.

CHAPTER III

METHODOLOGY

3.1 SiC Material Properties Modeling

Material properties of SiC can be modeled as a function of temperature, neutron flux, burnup. The material properties of the high-purity β -SiC are implemented into FRAPCON to model the fuel performance using SiC cladding. The material properties of SiC are largely-scattered due to its strong dependence on crystal structure, impurity level, and as-fabricated porosity. It is difficult to find the appropriate equations for modeling material properties unless a specific fabrication method is being defined. In current modeling, the chemical vapor deposited monolithic SiC cladding is assumed to possess high-purity and dense microstructure.

Table 3.1 Material properties of monolithic SiC/Zircaloy at room temperature

Material Properties	SiC (monolithic)	Zircaloy
Theoretical Density (g/cm ³)	3.21	6.55
Melting Temperature (K)	3000	2150
Thermal Conductivity (W/m-K)	350	13
Thermal Expansion Coef. (10 ⁻⁶ /K)	2.2	5.7
Elastic Modulus (GPa)	384	92
Flexural/Yield Strength (MPa)	**261~551	*268~387
Poisson's Ratio	0.21	0.41

3.1.1 Thermal Conductivity

Thermal conductivity of cladding is very important because not only does it affect the temperature of the cladding but also the temperature of the fuel. Higher thermal conductivity decreases both average cladding temperature and average fuel temperature, and general leads to a better performance over the fuel rod lifetime. The significant difference in material properties reflected in the thermal behaviors of Zircaloy vs. SiC. Therefore, it is vital to develop an accurate SiC thermal conductivity model under reactor condition.

Previous research conducted by Snead et al. [13] had discussed the thermal conductivity of SiC over a wide range of temperature, shown in **Fig. 3.1**. Two distinctive regions are indicated: **(1)** at temperature lower than 200 K, the thermal conductivity of SiC increase rapidly with temperature due to the large contribution of specific heat **(2)** beyond 200 K, the thermal conductivity of SiC decreases significantly with temperature due to the phonon-phonon scattering effect. The magnitude of thermal conductivity also depends on the microstructure of SiC [25], whereas below 300 K, the thermal conductivity increases monotonically with grain size. The grain size effect becomes less significant with increasing temperature due to the domination of phonon-phonon scattering effect.

The goal of this research is to model the fuel performance under LWR and eventually gas-cooled fast reactor conditions. Only the relationship between thermal conductivity and temperature above 200 K will be discussed. It can be expressed as:

$$k(T) = [-0.0003 + 1.05 \times 10^{-5}T]^{-1} \quad (3.1)$$

where

$k(T)$ = thermal conductivity of SiC (W/m-K)

T = cladding temperature (K)

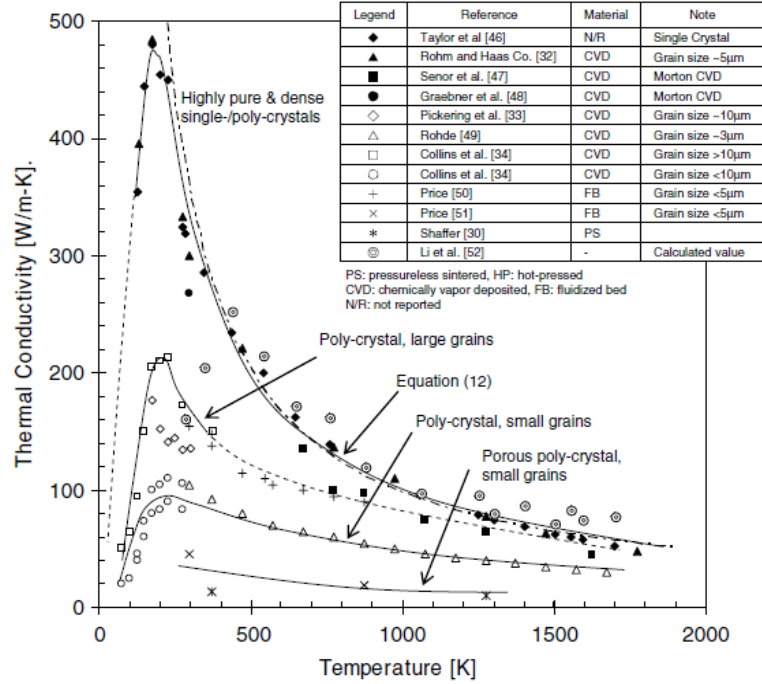


Figure 3.1 Thermal conductivity of SiC at elevated temperatures [13]

The thermal conductivity modeling of in-reactor SiC was based on the equation developed by Carpenter et al. [16]. Irradiation decreases the thermal conductivity dramatically by inducing point defects and defect-clusters in the SiC crystal, with a saturated concentration at 1 dpa [26]. The degradation of thermal conductivity in SiC composites is similar, but starts with a lower value of thermal conductivity due to the anisotropy introduced by the fibers.

The rapid decrease and saturation of thermal conductivity of SiC is reported by several authors based on their experimental results [13]. All reported values of thermal conductivity of SiC were found to degrade significantly at a very low exposure of 0.001 dpa. One point of particular interest is the increase of room temperature thermal

conductivity at the non-saturable regime, where the irradiation-induced void swelling again dominates the microstructure evolution. Unlike the behavior at the saturable regime, void-swelling at high-temperature regime does not contribute to the reduction but to the increase of thermal conductivity. Therefore, it is difficult to model the thermal behavior of SiC outside of the saturated regime accurately.

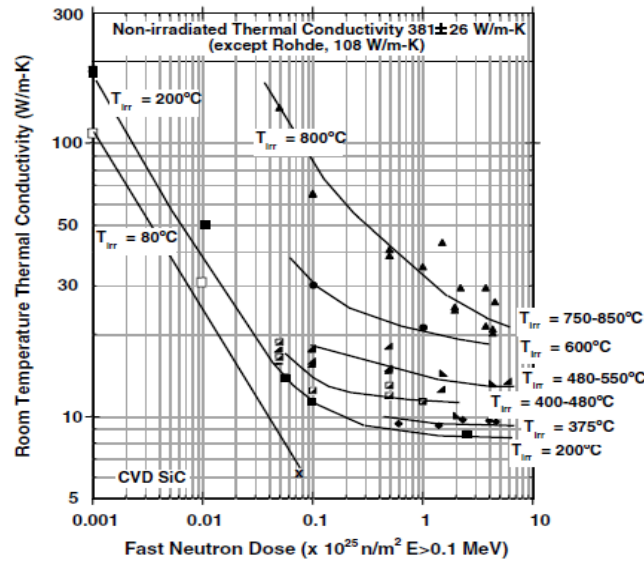


Figure 3.2 Thermal conductivity degradation of CVD SiC due to neutron irradiation at room temperature [13]

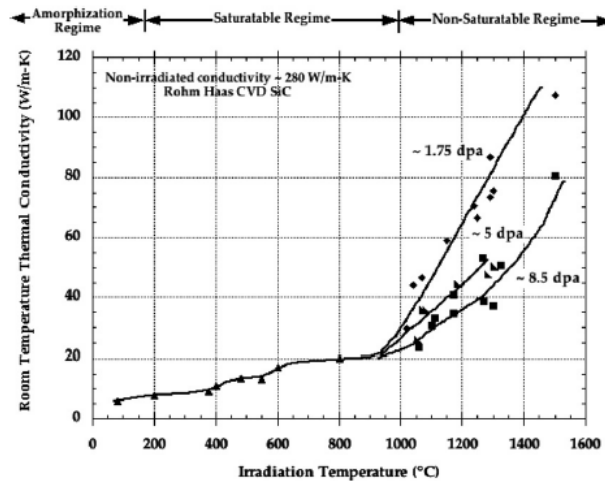


Figure 3.3 Thermal conductivity of SiC at room temperature in the void-swelling saturable and non-saturable regime [27]

In Carpenter's thermal conductivity modeling, the term d_0 serves as the effective dpa for $k(T) > k_{sat}$, the thermal conductivity after reaching d_{sat} , which is the saturation dose. From the measurements by Snead and Bourgoïn on fully amorphous SiC, it is observed that the thermal conductivity saturates at 1 dpa at 3.6 W/m-K regardless of the temperature [27, 28].

$$d_0 = d_{sat} \left[\frac{k_{sat}}{k(T)} \right]^{2.5} \quad (3.2)$$

The thermal conductivity of Zircaloy in FRAPCON is only modeled as a function of temperature, which increases slightly with temperature. However, the thermal conductivity of SiC is modeled as a function of both temperature and dose:

$$k(T, DPA) = k_{sat} \left[\frac{(d+d_0)}{d_{sat}} \right]^{-0.4} \quad (3.3)$$

The thermal conductivity of SiC at a given temperature and dose can be modeled by applying **Eq. 3.3**. Thermal conductivity soon becomes a weak function of temperature with increasing dose and saturates after reaching the saturation dose. It is plotted as a function of temperature in **Fig. 3.4** to compare with Zircaloy, and also as a function of dose to show the significant degradation at the BOL.

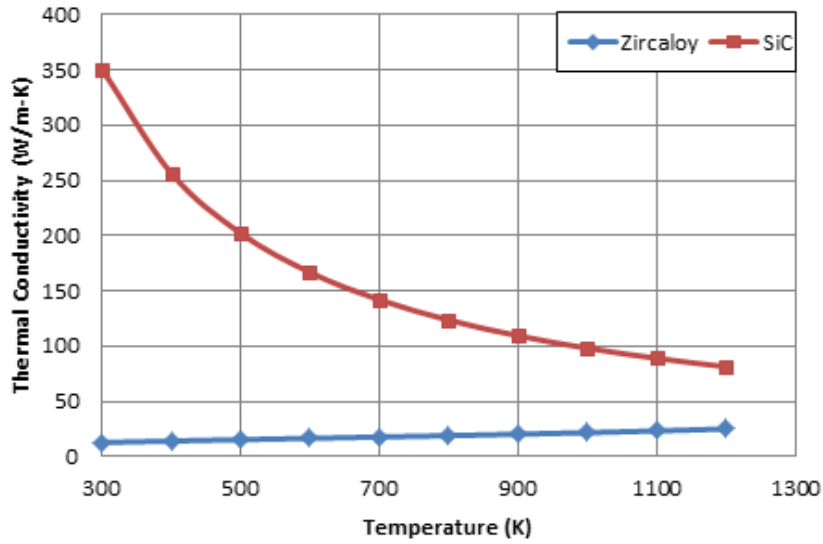


Figure 3.4 Thermal conductivity of un-irradiated SiC and Zircaloy vs. temperature

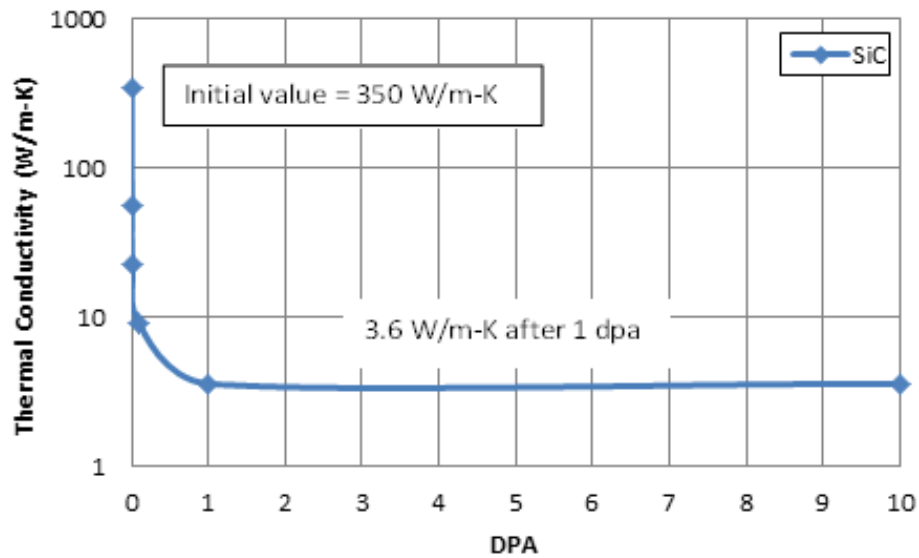


Figure 3.5 Thermal conductivity of irradiated SiC at room temperature

3.1.2 Thermal Expansion

Thermal expansion of the cladding and fuel is responsible for the significant change in pellet-clad gap size at BOL due to the difference in thermal expansion coefficient. During operation, the cladding and fuel temperature does not vary

significantly during normal operation, so the difference in cladding/fuel deformation from thermal expansion is small. The fuel-cladding gap width controls the thermal resistance of the heat flow from the fuel to the cladding, and hence significantly affects the overall fuel rod temperature.

The interatomic distance between Si-Si and Si-C atoms in SiC lattice is a function of temperature. The rise of temperature increases the total energy of atoms, causing atoms to vibrate and move slightly apart from their original lattice position. This microscopic effect results in a macroscopic effect of thermal expansion. In the strong covalent bonding of SiC, the vibration and dimensional changes are small, and results a low thermal expansion coefficient with weak temperature dependency compared to Zircaloy.

The thermal expansion coefficient for SiC has been reported over a wide temperature range shown in **Fig. 3.6**. **Eq. 3.4** is valid over the temperature range from 125~1273K. For temperature above 1273K, the thermal expansion coefficient is modeled as a constant, which can be shown in **Fig. 3.7**.

$$\alpha = -1.8276 + 0.0178T - 1.5544 \times 10^{-5}T^2 + 4.5246 \times 10^{-9}T^3 \text{ (} 10^{-6}/K \text{)}$$

$$125 \text{ K} < T < 1273 \text{ K} \quad (3.4)$$

$$\alpha = 5 \times 10^{-6} \text{ 1/K} \quad T > 1273 \text{ K} \quad (3.5)$$

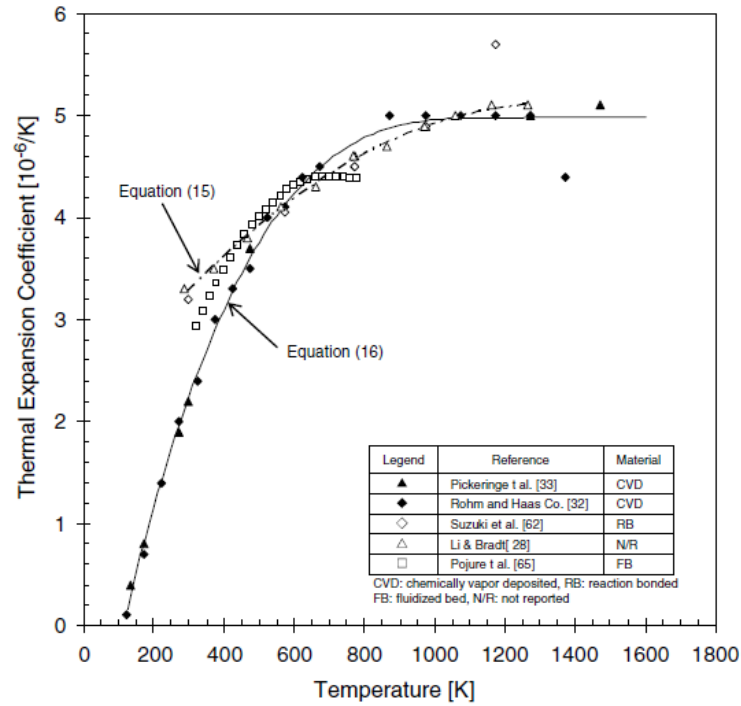


Figure 3.6 Thermal expansion coefficient of SiC vs. temperature [13]

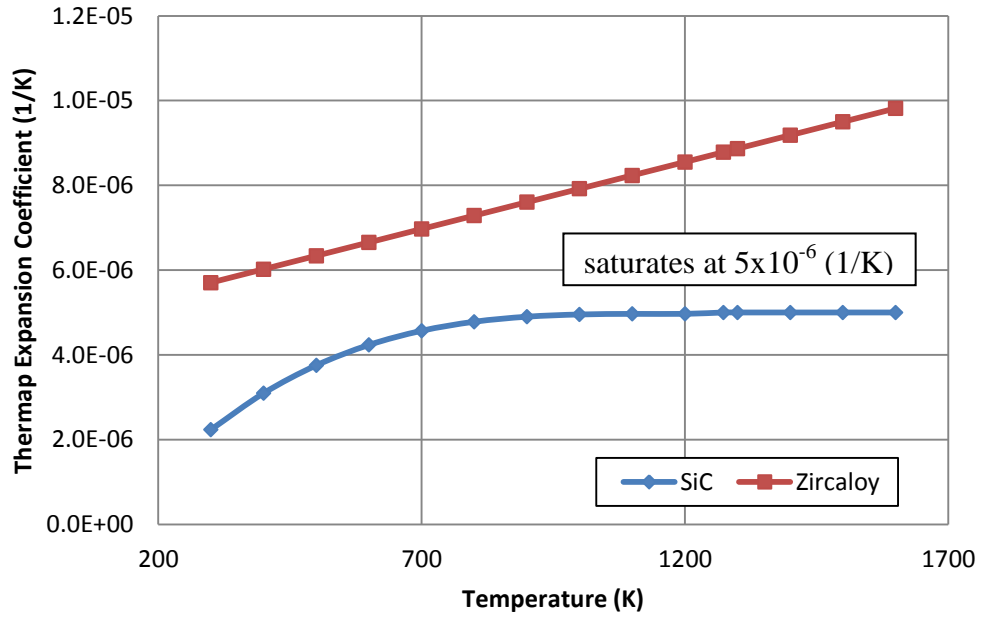


Figure 3.7 Thermal expansion coefficients vs. temperature: SiC & Zircaloy

The only report on the effect of neutron irradiation on thermal expansion coefficient was found in Price's result [29]. The report indicated no significant change in thermal expansion coefficient after irradiation; therefore, the current model neglects the irradiation effect to thermal expansion.

3.1.3 SiC Irradiation Swelling

SiC cladding irradiated by neutrons undergoes volumetric swelling. It plays an important role in determining the gap width and also to the volume between the top/bottom of fuel rods. Swelling, thermal expansion, elastic deformation of the cladding together with the fuel deformation will determine the gap width, and ultimately the time for pellet cladding mechanical interaction.

Recent SiC swelling model by Huang et al. [30] attributes the linear temperature dependence of swelling saturation to the formation and growth of small interstitial clusters from collision cascades initiated by neutron bombardments. These irradiation-induced interstitial clusters grow with elevated temperature and absorb mobile carbon interstitials. However, the cascade recombination events at higher temperature decrease the density of clusters sharply. Overall, SiC swelling follows linear dependency with temperature, and saturates at a fast neutron fluence of approximately 10^{25} n/m² at temperature below 1273 K.

Based on the experimental data provided by Snead et al.[31], the swelling of SiC reaches 95% of its saturated value after 1 DPA. In the current model, it is assumed that the swelling contributes equally in the plane and through the thickness of the monolithic layer, which equates to a maximum of 0.67% linear strain. For temperature below 1273 K, the linear strain is modeled using **Eq. 3.6**, as shown in **Fig. 3.8**.

$$\frac{\Delta L}{L} = 0.0067(1 - e^{-3DPA}) \quad (3.6)$$

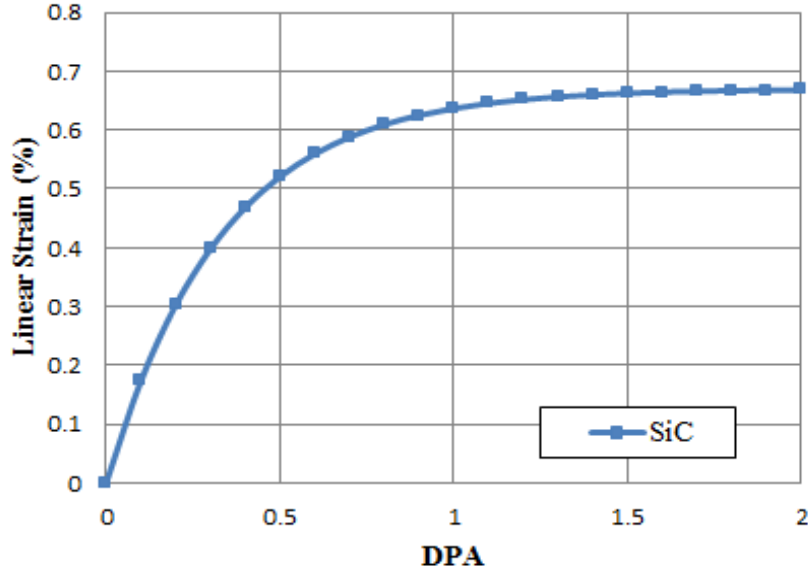


Figure 3.8 Linear irradiation-induced swelling strain of SiC below 1273 K vs. DPA

3.1.4 Elastic Modulus

The elastic modulus describes a material's dimensional response due to tensile or compressive force in the elastic deformation regime. This modulus can be obtained by plotting the stress vs. strain curve for an isotropic sample. The linear relationship of the curve indicates the elastic region and its slope is the elastic modulus.

Dense structure of CVD SiC usually exhibits the highest elastic modulus. Differ in manufacturing, the as-fabricated porosity and impurity concentration strongly affects the elastic modulus [32, 33]. Unlike thermal properties, neither grain size nor crystal structure have a significant effect on the modulus of SiC. The effect of porosity on the elastic modulus at room temperature is presented in **Fig. 3.9**. The elastic modulus, E , at room temperature can be expressed as below:

$$E = E_0 \exp(-CV_p) \quad (3.7)$$

where

$E_0 = 460$ GPa (elastic modulus of the pore-free CVD SiC)

$C = 3.57$

V_p = porosity %

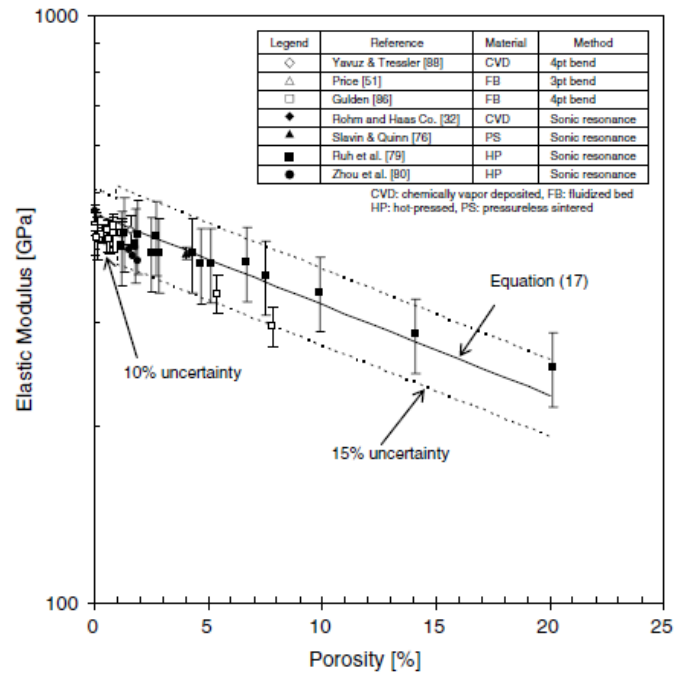


Fig. 3.9 Porosity effect vs. SiC elastic modulus [13]

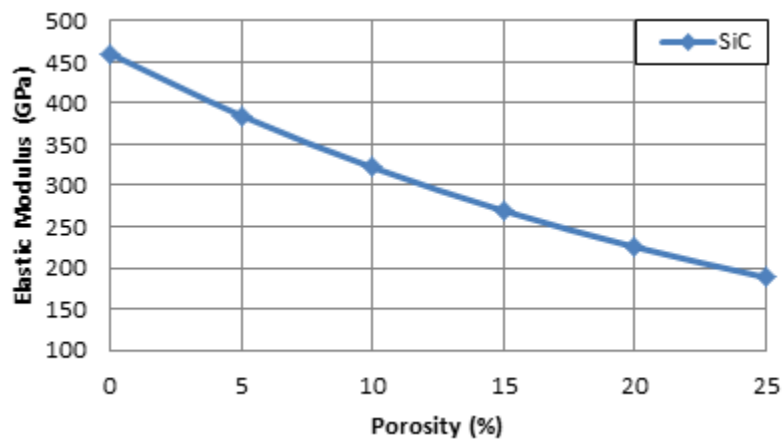


Figure 3.10 Modeling of SiC elastic modulus as a function of porosity

The elastic modulus of SiC has been reported to decrease with elevated temperature and irradiation-induced swelling, shown in **Fig. 3.11** and **3.12**. Higher temperature softens the residual silicon, causing re-distribution of silicon which may degrade the elastic modulus. Another mechanism responsible is the grain boundary relaxation, which can aggravate the degradation of elastic modulus by increasing the intergranular porosity [34]. The elastic modulus as a function of temperatures can be expressed as:

$$E = E_0 - B \exp\left(-\frac{T_0}{T}\right) \quad (3.8)$$

where

$$E_0 = 460 \text{ GPa}$$

$$B = 0.04 \text{ GPa/K}$$

$$T_0 = 962 \text{ K}$$

Lattice expansion/relaxation of SiC induced by irradiation is the major cause for the elastic modulus reduction, as the elastic modulus decrease with the point-defect swelling of SiC. Irradiation-induced swelling is an isotropic volumetric expansion that causes lattice relaxation because the accumulated point defects and clusters are not mobile during the irradiated temperature. Little is known for elastic modulus degradation beyond the saturation regime. However, the defects responsible for swelling in this regime are mainly voids and other relative larger defects that have a minor effect on elastic modulus as compared to point defects. An estimation of swelling on elastic modulus was based on using the Tersoff potential [35]. It predicted a linear lattice swelling of 1% will cause approximately 10% reduction in elastic modulus. Due to low-

swelling in LWR condition, and highly-scattered data, the degradation of elastic modulus by irradiation is not being modeled.

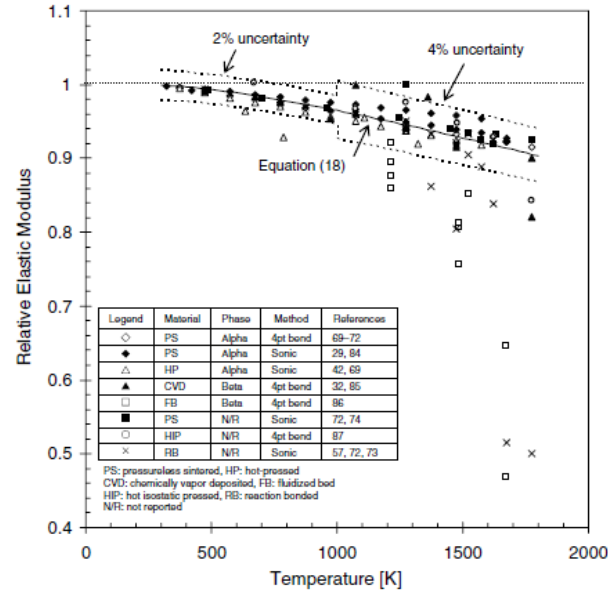


Figure 3.11 Temperature effect vs. SiC relative elastic modulus [13]

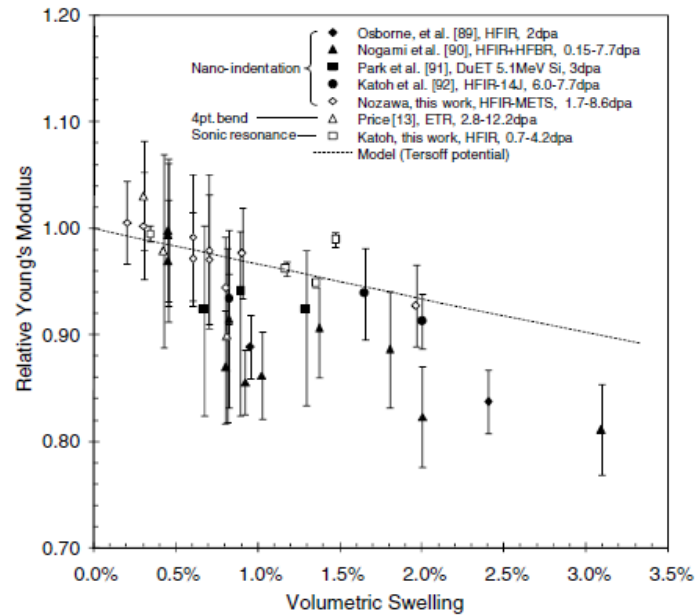


Figure 3.12 Irradiation-induced swelling vs. elastic modulus reduction of CVD SiC. Dot line is the effect of lattice relaxation on elastic modulus using Tersoff potential [13]

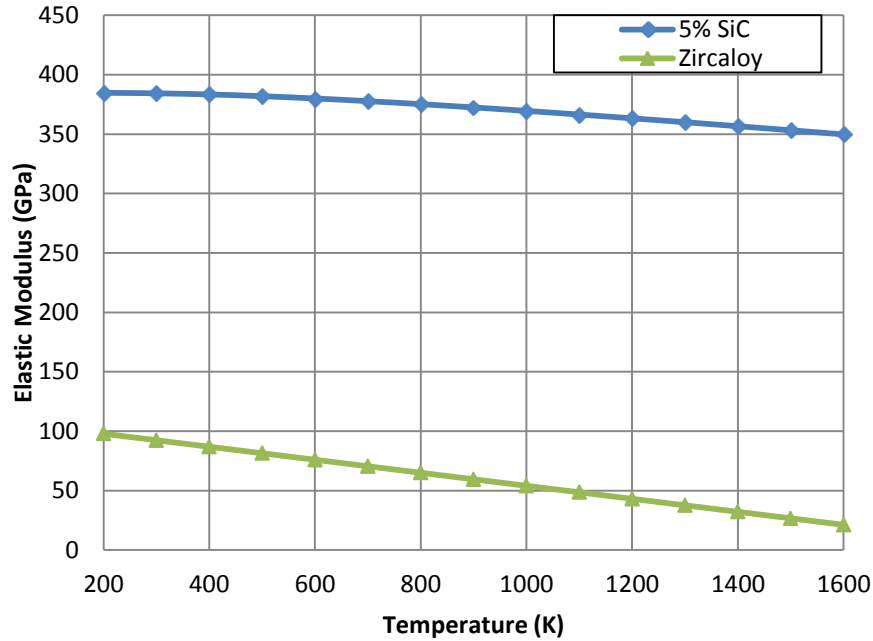


Figure 3.1.13 Elastic modulus degradation of 5% porosity SiC/Zircaloy vs. temperature

3.1.5 Flexural Strength

Flexural strength is the mechanical parameter of a brittle material that determines the ability to resist deformation under load, usually measured by the transverse bending test. Maximum flexural strength represents the highest stress experienced of the material at the moment of rupture.

The flexural strength of CVD SiC is shown in **Fig. 3.15**, as a function of dose [36]. It undergoes a modest increase by irradiation, and quickly saturates at 1 dpa. While the increase in flexural strength is significant, the temperature effect is obscure. From **Fig. 3.16**, flexural strength for CVD SiC increases at doses less than 10 dpa. However, for doses larger than 10 dpa, the effect of irradiation on flexural strength remains unclear. Mechanical testing by Ross et al. [9] reports a wide range of maximum flexural strength of monolithic SiC tube which is shown in **Fig. 3.14**, where the maximum flexural

strength range from 263 to 551 MPa, depending on the providing vendor. It is interesting that in all their tests, the monolithic SiC tubes fail at 0.2% strain in a brittle fashion.

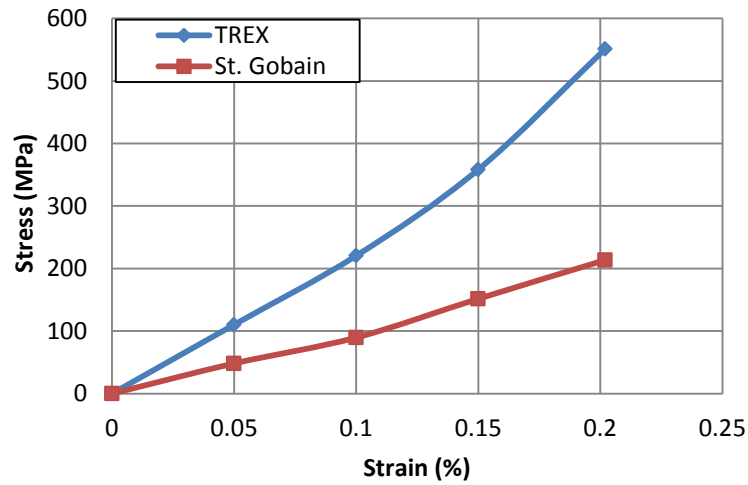


Figure 3.14 Maximum flexural strength of monolithic SiC tube of two vendors [9]

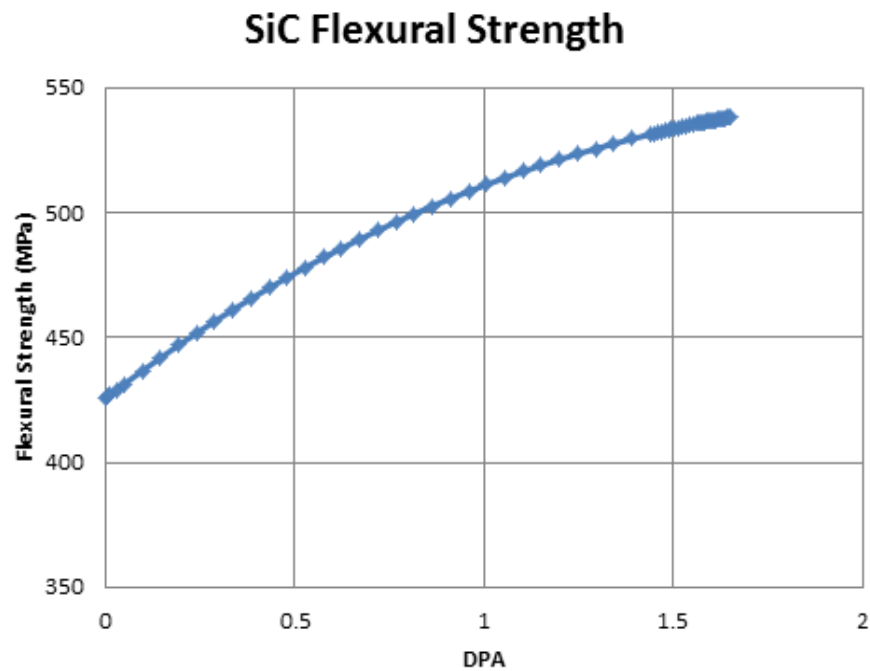


Figure 3.15 Flexural strength increase as a function of dpa

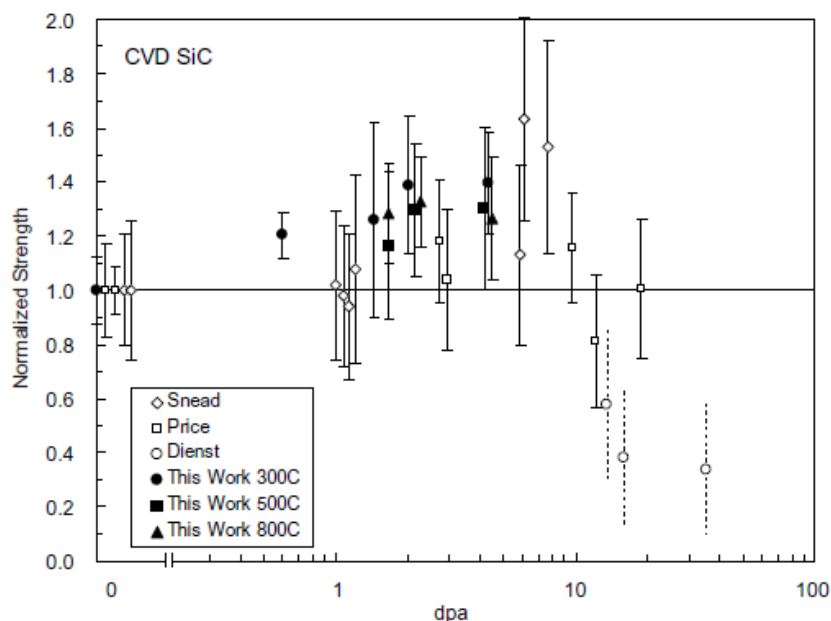


Figure 3.16 Flexural strength of CVD SiC vs. dpa: normalized to un-irradiated strength

FRAPCON-USC does not calculate for SiC cladding's maximum flexural strength for determination of cladding failure. For conservative estimation, the maximum flexural strength for failure analysis of monolithic SiC cladding will adapt the lower strength of 263 MPa.

3.1.5 Poisson's Ratio

. Poisson's ratio describes the deformation of material perpendicular to the direction of stress. The Poisson's ratio of SiC depends mostly on its stoichiometry, crystallinity, impurity level, and porosity. High-purity CVD SiC exhibits the highest Poisson's ratio of 0.21. Unlike other properties, the temperature and burnup effect is very insignificant. Therefore, it is modeled as a constant value of 0.21 over the burnup range in current FRAPCON-USC [13].

3.1.6 Shear Modulus

The shear modulus describes a material's response to shear stress, and is expressed as a function of the elastic modulus and the Poisson's ratio. The shear modulus at room temperature after correcting for porosity is about 195 GPa. Possessing the same trend as elastic modulus, the shear modulus of SiC also decreases with increasing temperature. The shear modulus is modeled using **Eq. 3.9**, as an isotropic material:

$$G = \frac{E}{2(1+\nu)} \quad (3.9)$$

where

E = elastic modulus

$\nu = 0.21$ (Poisson's ratio)

3.1.7 Hardness

SiC possess extremely high hardness due to its strong covalent bonding. It is generally dependent on the fabrication method, composition, and impurity levels. Ryshkevitch [37] reports the effect of porosity on the hardness of several oxide materials, which the relationship can be expressed by **Eq. 3.10**. Hardness is one of the parameters used in the calculation for the fuel-cladding conductance once hard-contact occurs. As the contact pressure increases, the point of contact will enlarge because of the localized plastic deformation, and therefore improves the thermal conductance.

$$H_v = 27.7 \exp(-5.4V_p) \quad (3.10)$$

where

H_v = Vicker's hardness (GPa)

V_p = porosity (%)

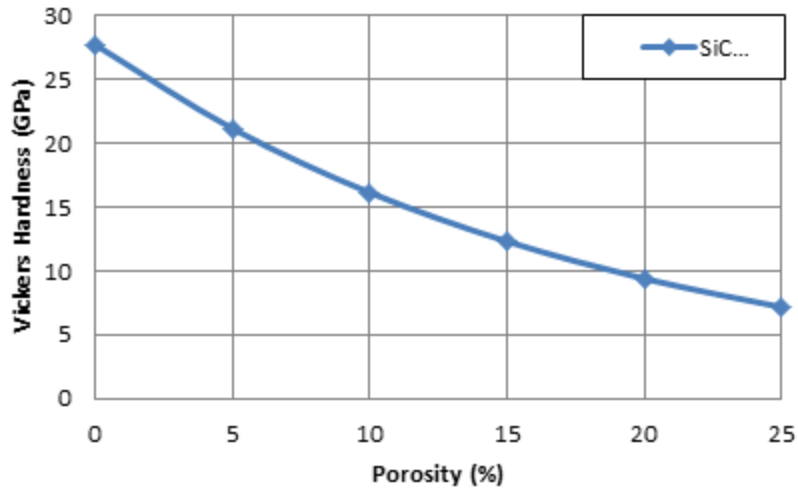


Figure 3.17 Effect of porosity vs. SiC hardness

Fig. 3.18 shows the Vickers hardness for SiC with different porosity at elevated temperatures. It can be categorized into two temperature regimes: athermal and thermally-dependent regime. The hardness of SiC stays constant at lower temperature and will decrease rapidly after passing the ductile-to-brittle temperature (DBTT). It is also interesting to note that DBTT increases slightly with porosity.

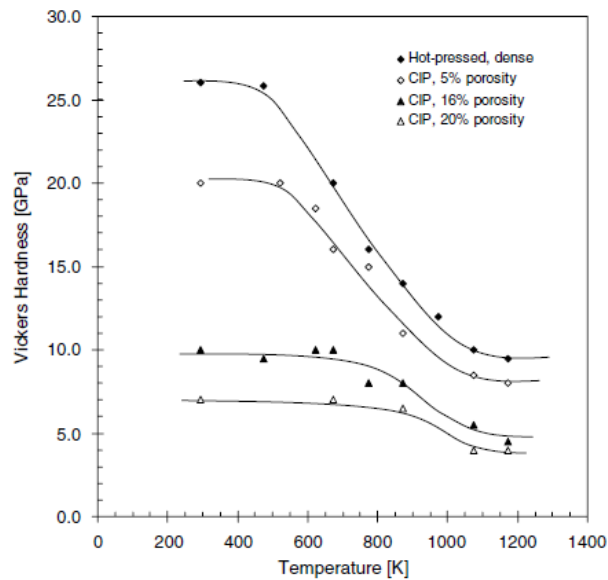


Figure 3.18 Temperature effect on SiC hardness [13]

3.2 Other SiC Properties

3.2.1 Plastic Deformation

Monolithic SiC is assumed to be a perfect elastic solid that will fail immediately in a brittle manner upon reaching yield strength. All plastic deformations are prohibited in this modeling using FRAPCON-USC.

3.2.2 Creep

Creep of SiC under elevated temperature and neutron irradiation is categorized into two parts: the thermal-induced creep and the irradiation-induced creep. Each regime is individually discussed and evaluated for its significance under the modeling condition.

(a) Thermal-Induced Creep:

The thermal-induced creep has been observed only at very high temperatures (above 1673 K) for high-purity, polycrystalline β -SiC [34, 38], from experiments by DiCarlo [39]. Experimental data for the steady-state creep rate of SiC were reported by Gulden [34], and Carter et al. [38] were not consistent with each other, mainly because of the different material quality and the loaded crystallographic direction. A general power-law steady-state creep rate equation is obtained from experimental data:

$$\dot{\epsilon} = A_s \left(\frac{\sigma}{G} \right)^n \exp \left(\frac{-Q}{k_b T} \right) \quad (3.11)$$

where

$A_s = 2 \times 10^3$, n is the stress exponent 2.3, Q is the activation energy 174 kJ/mol, σ is the applied stress (MPa), G is the shear modulus (GPa), k_b is the gas constant 8.314 J/mol-K, and T is the temperature in Kelvin.

(b) Irradiation-Induced Creep

The role of irradiation is to induce creep at a temperature where thermal creep is negligible, usually below $0.5 T_m$ for most materials. In metals, the irradiation-induced creep is proportional to the applied stress, neutron flux, and the creep compliance [40]. First results published for the irradiation-induced creep of SiC was by Price [41]. A linear-averaged steady-state creep compliance of $2 \times 10^{-6} (\text{MPa-dpa})^{-1}$ is used for doses at 0.6~0.7 dpa at all temperature. A conversion rate from displacement per atom to neutron flux is also used for irradiation-induced creep modeling [42]:

$$1 \text{ dpa} = 10^{21} \frac{n}{\text{cm}^2} \quad (3.12)$$

The irradiation-induced steady-state creep can be plotted as a function of applied stress (MPa), neutron flux ($\text{n/cm}^2\text{s}$), and creep compliance:

$$\dot{\epsilon} = \sigma B \phi \quad (3.13)$$

(c) Comparison Between SiC and Zircaloy Creep

The thermal and irradiation-induced steady-state creep rate of Zircaloy can be calculated using material properties from MATPRO [18] using cladding average temperature, neutron flux, and effective stress. Steady-state creep rate for both cladding type were modeled as a function of effective stress under typical LWR condition, assumed cladding average temperature of 600 K, and fast neutron flux of $2.21 \times 10^{16} \text{ n/m}^2\text{s}$ (test case 1 used in Chapter 4). A comparison of modeled cladding steady-state creep rate for both materials is shown in **Fig. 3.19**.

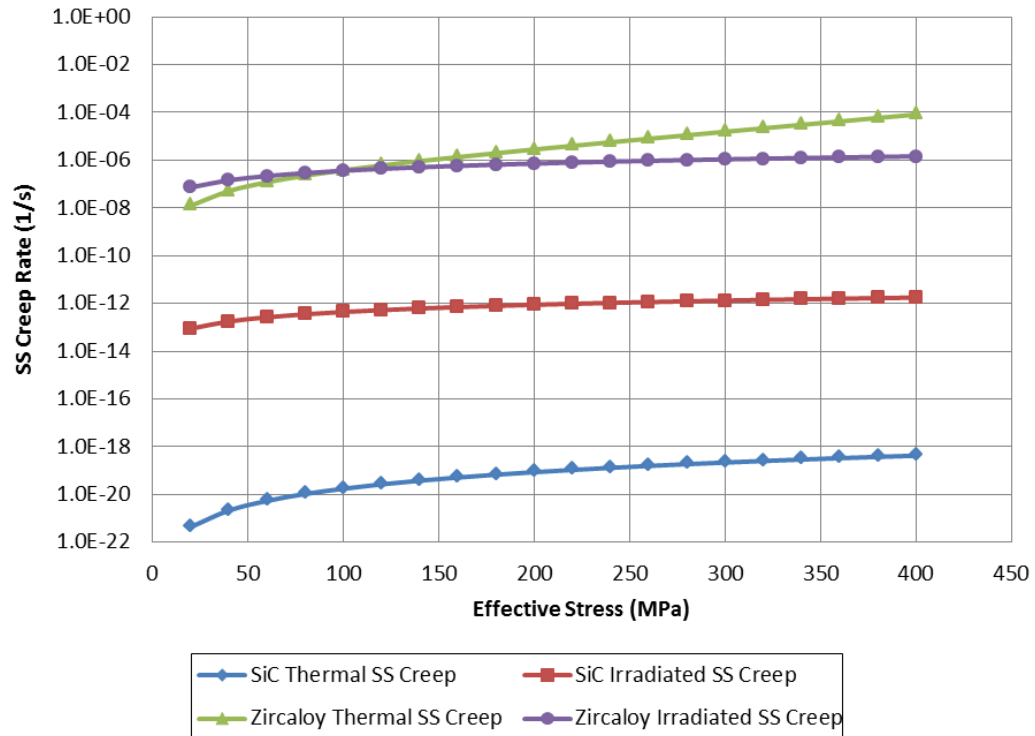


Figure 3.19 Thermal/irradiation induced steady-state creep rate vs. effective stress at 600K

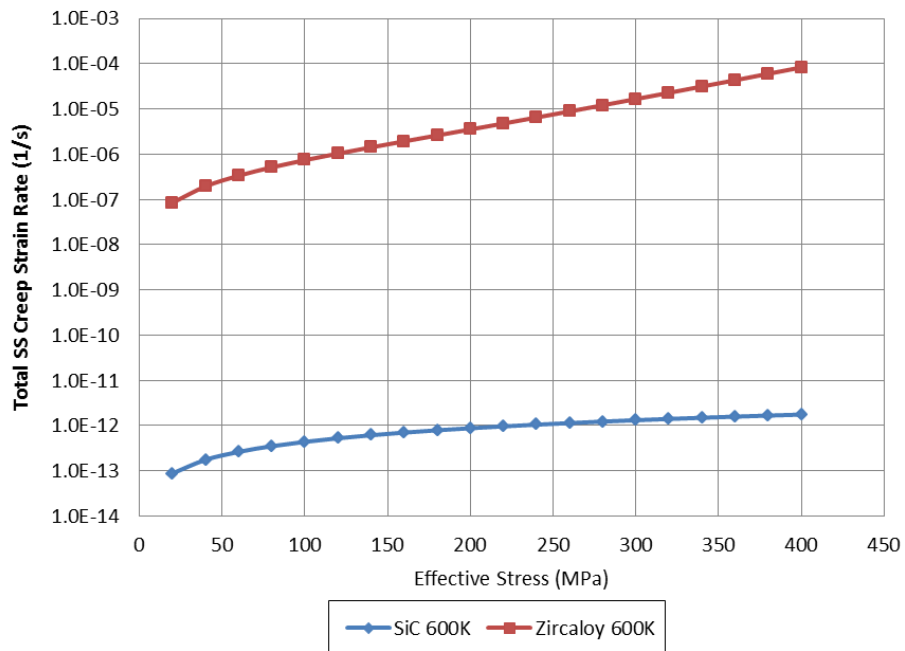


Figure 3.20 Total steady-state creep rate vs. effective stress at 600 K

From **Fig. 3.20**, the total steady-state creep rate of SiC is at least 5 orders of magnitude lower than the steady-state creep rate of Zircaloy. According to this result, the steady-state creep of SiC is neglected in the current FRAPCON-USC modeling under LWR condition.

3.2.3 Oxidation

The data for the oxidation behavior of SiC in LWR environment is limited. The oxidation kinetics of SiC is very complex, which depends on the atmosphere, oxygen partial pressures, temperatures, and SiC microstructures. It is not known whether exposure to coolant will result in the formation of a protective oxide layer on the surface of the SiC cladding as with Zircaloy, which leads to weight gain and reduced thermal conductivity. There may also be a corrosive effect that results in a weight loss, thinning of the cladding or increase in porosity. In light of insufficient data and the complexity of oxidation behavior, the oxidation rate is set to zero in FRAPCON-USC modeling.

3.2.4 Emissivity

Emissivity is the fraction of thermal radiation emitted by the surface of a body relative to a blackbody. The closer to unity, the better the surface is at emitting/absorbing thermal radiation. The emissivity can be changed through applications of different surface coating and changing the surface roughness. A value of 0.8 is used for SiC composite by Carpenter [16]. Due to lack of emissivity data for CVD SiC, 0.8 is also used in the FRAPCON-USC modeling.

3.2.5 Phase Transition

SiC exists in two crystalline structures, α and β phase. Only the β phase is found at temperature below 2300 K, and possesses high-purity microstructure. SiC will start to decompose at 2600 K, atmospheric pressure. This is well above the temperature range of interest for LWR cladding. Therefore, the phase change of SiC is not modeled in FRAPCON-USC.

3.2.6 Crud Accumulation

When coolant flows through the core, corrosion products from other components that are suspended in the water will begin to accumulate on the cladding surface. This accumulation is modeled as either a constant or a growing layer on top of the oxide layer. It will have to be determined experimentally for the monolithic SiC cladding's affinity for accumulating the deposits based on material and surface texture. In current modeling, the rate of crud accumulation and thermal resistance is set equal to that of Zircaloy cladding.

3.3 Pellet-Cladding Mechanical Interactions

The deformation of both pellet and cladding will determine the status of pellet-cladding gap. Gap width determines the gap conductance, hence the temperature distribution in pellet and cladding. The thermal and mechanical analyses are equally important and should be closely coupled. Theoretically, both analyses should be solved simultaneously, but FRAPCON solves them separately and provides coupling through an iterative scheme. At the end of each analysis, either a new open-gap size or a closed gap with pellet-cladding interfacial pressure is obtained.

An intermediate “soft-contact” regime exists before true PCMI (hard-contact) occurs. This process will be discussed in more detail in the fuel cracking/relocation section. After the partial recovery of pellet cracks, fuel swelling starts to dominate the stress/strain calculations of the fuel rod (soft pellet model), which usually accumulates a large interfacial pressure, P_{int} , between pellet surface and cladding. **Fig. 3.21** shows the evolution of fuel and gap width at various regimes.

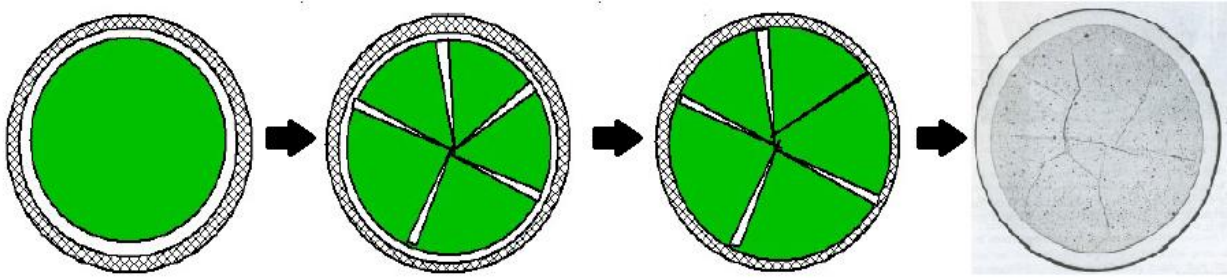


Figure 3.21 Cross-sectional view of the pellet evolution during operation

3.3.1 Fuel Cracking and Relocation Modeling

Fuel relocation phenomenon was drawn to attention when the measured fuel pellet centerline temperature at BOL was found to be lower than the value predicted by fuel performance code which predicts the fuel-clad gap based on only the fuel and cladding thermal expansion [43]. It is later observed that pellets crack at startup due to the thermal stresses induced by the thermal expansion differences at the hot pellet center and cold periphery.

The maximum thermal stress, $\sigma_{t, \max}$, at pellet periphery in an un-cracked pellet submitted to a parabolic temperature gradient must be compared with the fracture stress of UO_2 , which is approximately 130 MPa. Consider UO_2 material properties, radial cracks are assume to initiate in the pellet periphery at a low linear heat rate of 5 kW/m. Oguma [44] proposed a linear model of crack numbers vs. linear heat rate as illustrated in

Fig. 3.22. The consequences of cracking are very important in fuel performance modeling. Because of the larger thermal expansion of the fragments and the vibration induce the cracked pellet fragments to move outward. This phenomenon is called fuel “relocation” and has a strong impact on the fuel temperature as shown in **Fig. 3.23**. These new crack volumes within the pellet are compensated by a reduction in gap volume. This gap reduction, or alternatively, can be interpreted as increase in pellet diameter due to pellet cracking. Gap change during irradiation is a major factor influencing fuel rod performance including fuel temperature, fission gas release, and initiation of PCMI.

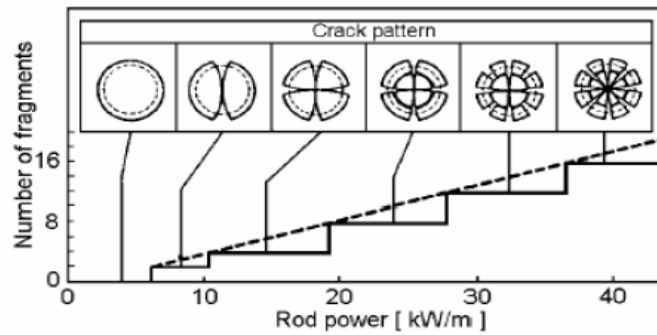


Figure 3.22 Calculated crack patterns from thermal-induced stress [44]

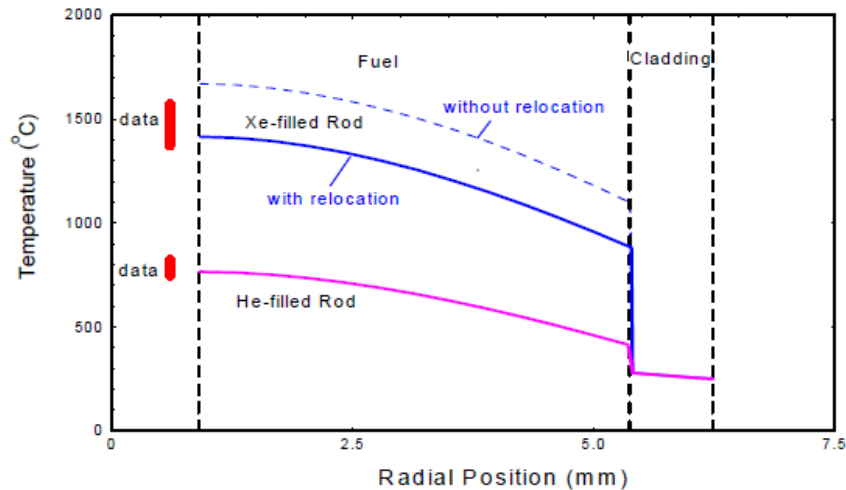


Figure 3.23 Fuel radial temperature distribution at BOL with/without relocation [45]

The change of gap size with irradiation is measured experimentally in order to calculate the relocation strain [46]. Results in instrumented fuel rods, as shown in **Fig. 3.24**, indicates that $40 \pm 20\%$ of the initial gap is eliminated during the first heat-up to full power. The change in gap volume in FRAPCON is modeled as a function of linear heat generation rate and burnup shown in **Fig. 3.25**. The overall relocation strain is calculated using Eq. 14.

$$\varepsilon_{relocation} = \frac{G_c \times \frac{\Delta G}{G}}{R_{f, cold}} \quad (3.14)$$

Where

G_c = cold gap width

$R_{f, cold}$ = cold-pellet radius

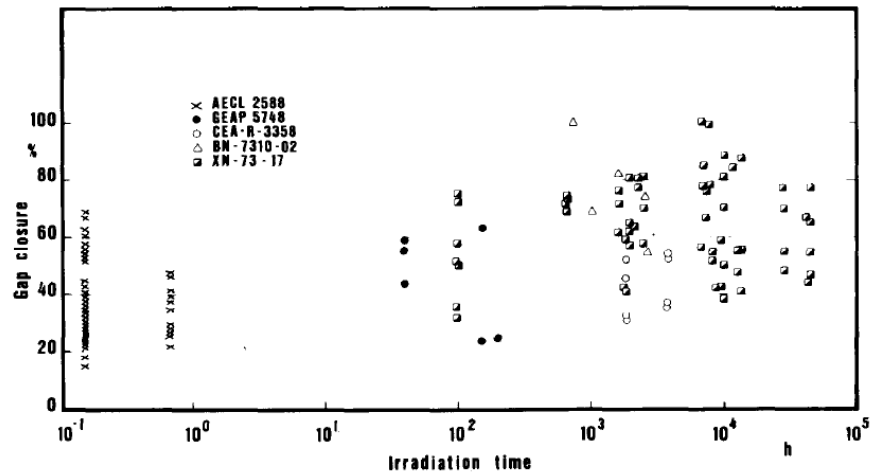


Figure 3.24 Experimental data of the % of gap closure under irradiation [46]

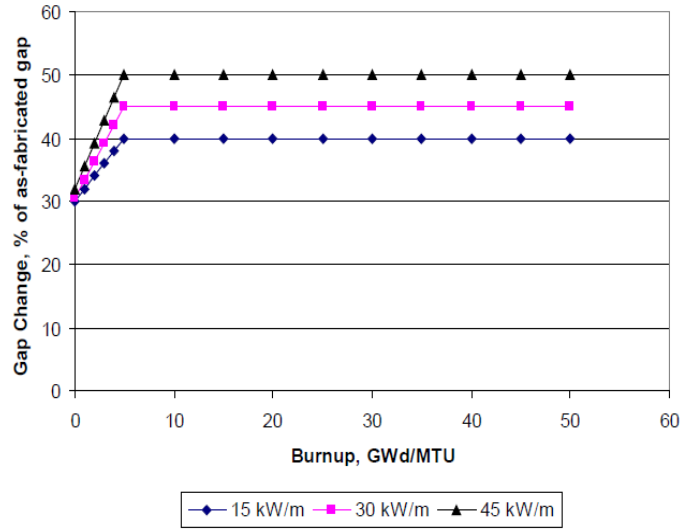


Figure 3.25 FRAPCON modeled gap change $\frac{\Delta G}{G}$ as a function of power and burnup [3]

3.3.2 Gap Width Model: Considering Fuel Deformation

Oguma's pellet crack and relocation model introduces a gap model with different PCMI regions and a critical void ratio for determination of the hard-contact PCMI condition [44]. The gap model is divided into four regions, and is discussed individually as shown in **Fig. 3.26**.

Region I

Both cladding and fuel deformations contribute to the change in gap width at this region. The thermal expansion differences between pellet and cladding, fuel swelling/densification, and the creep of fuel and cladding are all considered in the calculation of gap width. For the case of SiC-clad fuel, the decrease in gap width is slower due of the negligible cladding creep.

Region II

The gap decreases abruptly due to pellet cracking and the subsequent pellet jumping. The phenomenon of pellet jump, which occurs after pellet cracking, is a phenomenon that relates to the fuel's material properties (fracture strength, elastic modulus, and thermal conductivity) of the fuel. It results in a rapid decrease in the gap size. In typical BWR fuel rods, the UO₂ fuel pellet cracks at a rod power of 6~9 kW/m and a subsequent gap decrease of 40~60 μm during the early rise of power.

Region III

From the end of the pellet jump until the onset of hard PCMI, this region is termed as the “soft contact” region. At first, fuel fragments and cladding are only in contact with cladding at a few points. As power increases, pellet diameter increases due to additional thermal expansion and swelling, accommodating some of the void spaces. However, there are also spaces within the rod where the pellet fragments can relocate under a weak constraint from the cladding. Hard-contact will not occur until fuel fragments have filled up a certain volume of the void spaces. A critical void ratio β is used to determine the point of hard contact.

$$\beta = \frac{2G}{D_c} \text{ (unitless)} \quad (3.15)$$

D_c = cladding inner diameter (mm)

G = effective gap (μm)

Region IV

Hard-contact will be initiated when the critical void ratio is achieved by the accommodation of the void spaces by fuel fragment swelling and thermal expansion. The

cracked fragments once again return to a rigid body and initiates hard-contact. This concept is based on the assumption that hard-contact occurs due to a loss of compressibility in the cracked pellets. The compressibility arises from a reduction of the void space in which pellet fragments are movable.

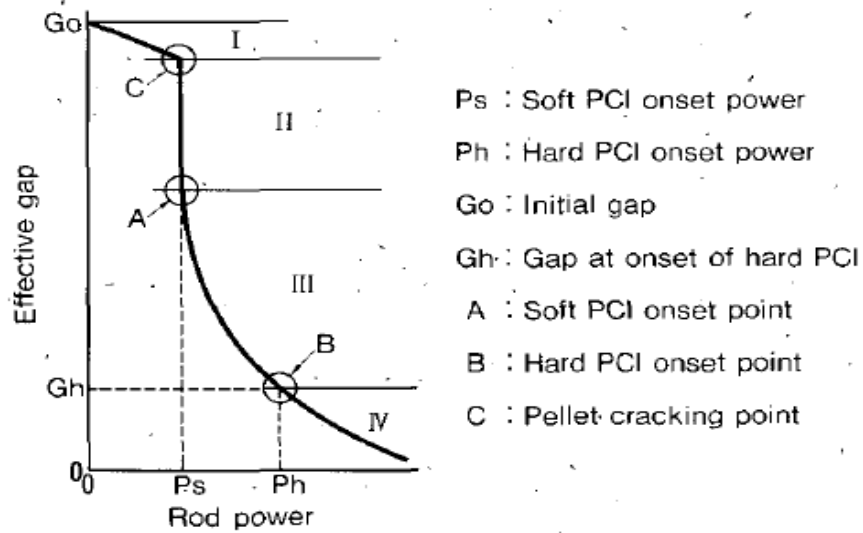


Figure 3.26 Gap model showing the relationship between gap width and rod power

3.3.3 Modeling of elastic modulus recovery in FEMAXI

FEMAXI models fuel relocation using the concept of pellet elastic modulus recovery [47]. When a pellet is subjected to a tensile thermal stress due to thermal expansion, it is assumed that cracks are generated and the elastic modulus is decreased to approximately 1/100 of its original value. When the pellet is in a compressive stress due to PCMI, it is assumed that the elasticity of pellet will gradually recovers with the decreasing relocation strain. In **Fig. 3.27**, E_c is the reduced elastic modulus of cracked pellets, ϵ_e is the tensile strain due to elastic compression, and ϵ_{rel} is the recovered relocated strain.

When the pellet is not in contact with the cladding, thermal stress in the pellet is mostly relieved by the production of cracks. The pellet can expand without constraint and the gap is narrowed. However, when the pellet is in contact with the cladding, compressive strain inside the pellet will increase due to the cladding restraint. Void space generated by relocation is then compressed, and the pellet stiffness increases. This can be modeled by increasing the elastic modulus linearly with relocation strain recovery. This is the process where a mechanical interaction is gradually increased between a cracked/relocated pellet and the cladding. Elasticity of a pellet completely recovers to its original value when pieces of the cracked pellet are compressed by cladding and therefore fill the void spaces. A strong interaction between pellet and cladding is then assumed.

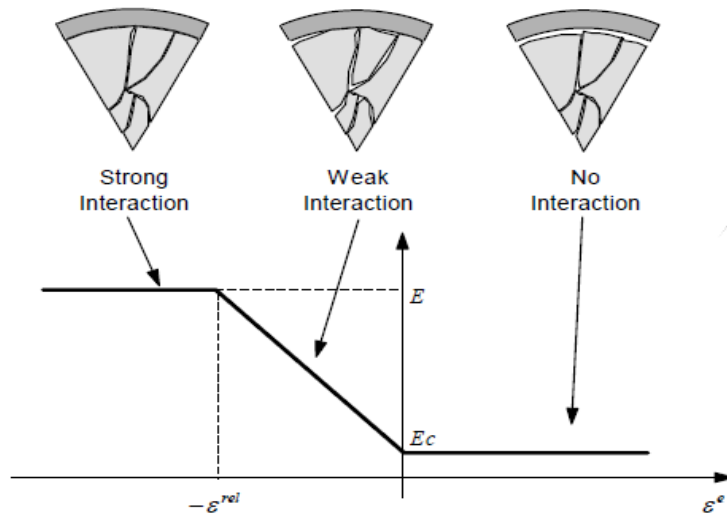


Figure 3.27 Stiffness recovery model of pellet with cracks [47]

3.3.4 Implementation of Fuel Creep

The gap width, $G(B)$ (μm), with the burnup effect included can be expressed as following equation:

$$G(B) = C_1'(2 - C_3)e^{-C_2A} - C_1'(1 - C_3)e^{-(C_2A+C_4B)} \quad (3.16)$$

where

$A = P/60$ (W/cm), P = linear heat generation rate

B = burnup (GWD/MTU)

$C_1' = G_0 - (\Delta D_j + K)$, G_0 is the initial gap (μm),

$\Delta D_j = 3.6\Delta D$ (μm) pellet jump distance, ΔD = pellet diameter change due to thermal expansion

K = diametral change of pellet caused by swelling, densification, and creep

$C_2 = 0.0039$

$C_3 = 1.41$

$C_4 = 0.95$

Implement fuel creep into the term K will decrease C_1' and also the overall gap width. The creep behavior of UO_2 will be discussed in greater detail in Chapter 4. Elastic deformation of pellet is not considered because the pressure exerted on the fuel pellet from the gap gas pressure is considered as a hydrostatic force. Once true PCMI occurs, a pressure of much larger magnitude, hence called “interfacial pressure” is created by the cladding constraint. This significance of interfacial pressure will then determine the magnitude of the elastic deformation of fuel pellet.

3.4 Soft Pellet Model

FRAPCON calculates the total radial and axial change of the fuel by considering thermal expansion, swelling, and densification. Relocation is only included in the thermal response to model the temperature profile more accurately. No hard contact between the

fuel and cladding is allowed until other fuel expansion components recover 50% of the relocation strain in the mechanical analysis. FRAPCON's mechanical model, FRACAS-I assumes that no pellet deformation is induced by fuel-cladding interfacial pressure; therefore it is also called the rigid pellet model. Additional pellet deformations are evaluated to provide an understanding of the significance of pellet deformations due to the large interfacial pressure during hard-contact.

3.4.1 UO₂ Elastic Modulus

All stress-induced deformations of the fuel are neglected in current FRAPCON, because of the high elastic modulus of the ceramic UO₂ fuel and insignificant interfacial pressure created when using the ductile metallic (lower elastic modulus and capable of creep) Zircaloy cladding. Using a stiff ceramic cladding such as SiC, it can only relieve excessive stresses through minor elastic deformation, will result a much larger interfacial pressure at the pellet surface. The elastic modulus of UO₂ can be expressed as a function of porosity and temperature shown in **Fig. 3.28** [46].

$$E \text{ (GPa)} = 229 - 0.0201T - 587P \quad (3.17)$$

where

T = average temperature of the fuel

P = as-fabricated porosity of fuel

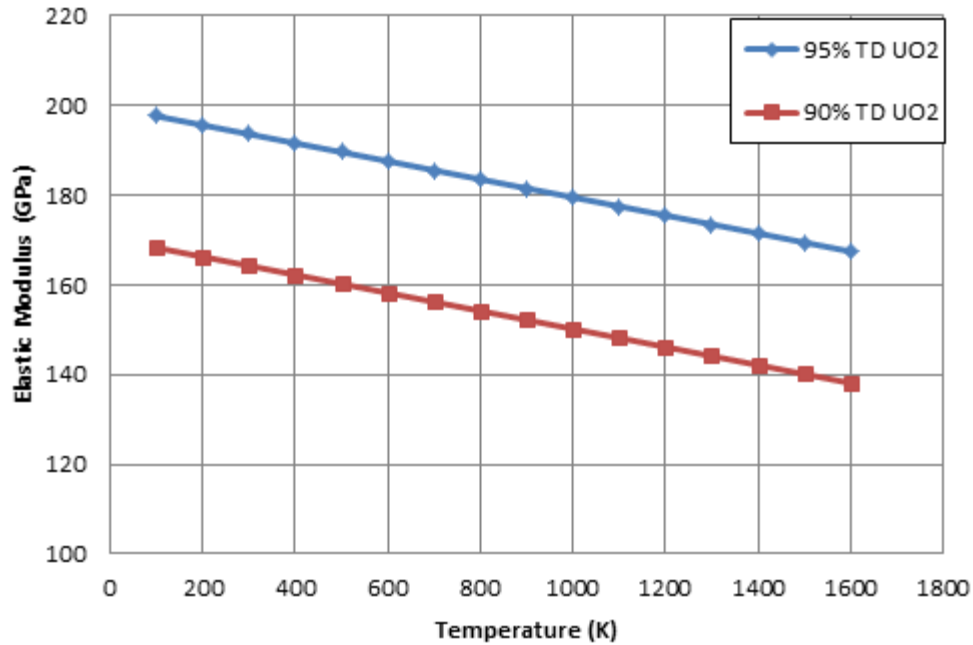


Figure 3.28 Elastic modulus of UO_2 as a function of temperature

3.4.2 Implementation of the soft-pellet model

An approach to consider the effect of pellet deformation to the interfacial pressure in developed in this research. The solution scheme of the soft-pellet model contains four steps: **(1)** pellet elastic deformation due to the feedback of interfacial pressure **(2)** apply the modified radial and axial deformations of pellet to meet the closed-gap criterion for radial/axial continuity **(3)** calculates new cladding radial/axial deformation based on the closed-gap criterion **(4)** obtain new cladding hoop stress and interfacial pressure. A schematic showing the solution scheme for the soft-pellet model is given in **Fig. 3.31**.

(a) Stress-strain calculations during closed gap

During closed-gap, the elastic stress-strain calculations of cladding can be calculated using a sequence of Hooke's equation. The radial stress is neglected because the cladding is assumed to be a thin-walled cylindrical shell. However, radial strain still

needs to be considered because of the Poisson's effect. The stress/strain equations are listed below:

$$\sigma_{\theta}(\text{hoop stress}) = \frac{r_i P_{int} - r_o P_{ext}}{t} \quad (3.18)$$

$$\sigma_z(\text{axial stress}) = \frac{r_i^2 P_{int} - r_o^2 P_{ext}}{t} \quad (3.19)$$

P_{ext} = external coolant pressure

P_{int} = interfacial pressure

r_o, r_i = cladding outer/inner radius

t = cladding thickness

$$\varepsilon_{\theta}(\text{hoop strain}) = \frac{1}{E} (\sigma_{\theta} - \nu \sigma_z) \quad (3.20)$$

$$\varepsilon_z(\text{axial strain}) = \frac{1}{E} (\sigma_z - \nu \sigma_{\theta}) \quad (3.21)$$

$$\varepsilon_r(\text{radial strain}) = \frac{-\nu}{E} (\sigma_z + \sigma_{\theta}) \quad (3.22)$$

And the displacement of cladding can be obtained

$$u_{co}(\text{outer surface displacement}) = \tilde{r} \varepsilon_{\theta} + \frac{t}{2} \varepsilon_r \quad (3.23)$$

$$u_{ci}(\text{inner surface displacement}) = \tilde{r} \varepsilon_{\theta} - \frac{t}{2} \varepsilon_r \quad (3.24)$$

$$\varepsilon_{cz}(\text{cladding axial strain}) = \varepsilon_z \quad (3.25)$$

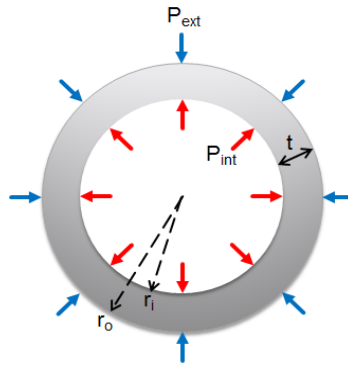


Figure 3.29 Cladding at closed-gap

(b) Closed-gap criterion

Closed-gap criterion in both radial and axial direction must be satisfied to maintain the closed-gap status. In the radial direction, the pellet outer surface displacement and cladding inner surface displacement must be equal to satisfy the closed-gap criterion. In the axial direction, any additional strain from the pellet is transferred entirely to the cladding. Therefore, cladding deformation is totally dominated by the pellet deformation model during closed-gap.

$$u_{fo} = u_{ci} \text{ (radial continuity)} \quad (3.26)$$

u_{fo} = fuel pellet outer radial displacement

u_{ci} = cladding inner surface radial displacement

$$\varepsilon_z^{clad} - \varepsilon_{z,o}^{clad} = \varepsilon_z^{fuel} - \varepsilon_{z,o}^{fuel} \text{ (axial continuity)} \quad (3.27)$$

$\varepsilon_{z,o}^{clad}$, $\varepsilon_{z,o}^{fuel}$ are the axial strains at contact

(c) Pellet-cladding interfacial pressure

After the cladding radial displacement and axial strain are determined by the closed-gap criterion, they are used in a thin cylindrical shell with prescribed external pressure from coolant to determine the pellet/clad interfacial pressure

$$\sigma_\theta = \frac{E[2u_{ci} - \varepsilon_z v(t - 2\tilde{r})]}{2\tilde{r} + v(t + vt + 2\tilde{r}v)} \quad (3.28)$$

$$\sigma_z = \frac{E[2\varepsilon_z \tilde{r} + v(\varepsilon_z t + 2u_{ci})]}{2\tilde{r} + v(t + vt + 2\tilde{r}v)} \quad (3.29)$$

where

E = elastic modulus of cladding

v = Poisson's ratio

$$\tilde{r} = \frac{r_o + r_i}{2}$$

Finally, the interfacial pressure can be expressed as:

$$P_{int} = \frac{t\sigma_{\theta} + r_o P_o}{r_i} \quad (3.30)$$

P_o = external coolant pressure

(d) Pellet elastic deformations

When the fuel and cladding are in hard-contact, the elastic deformation of the fuel pellet is introduced to the total fuel deformation model by considering the effect of the fuel-cladding interfacial pressure, P_{int} . The radial stress at the pellet periphery is determined directly from the interfacial pressure, while the pellet axial stress is determined by the surrounding plenum gas pressure.

$$\sigma_{rf} = -P_{int} \quad (3.31)$$

$$\sigma_{zf} = -P_g \quad (3.32)$$

P_g = plenum gas pressure

$$\varepsilon_{rf} = \frac{1}{E_f} (\sigma_{rf} - \nu_f \sigma_{zf}) \quad (3.33)$$

$$\varepsilon_{zf} = \frac{1}{E_f} (\sigma_{zf} - \nu_f \sigma_{rf}) \quad (3.34)$$

E_f, ν_f = elastic modulus and Poisson's ratio of the fuel

Fuel radial displacement

$$u_{fo} = r_{fo} \varepsilon_{rf} \quad (3.35)$$

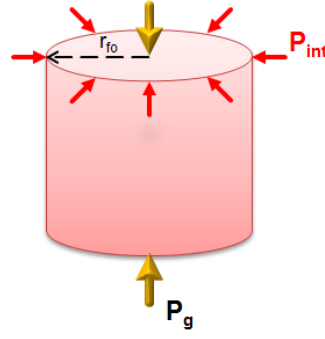


Figure 3.30 Interfacial pressure exerted on pellet at closed-gap

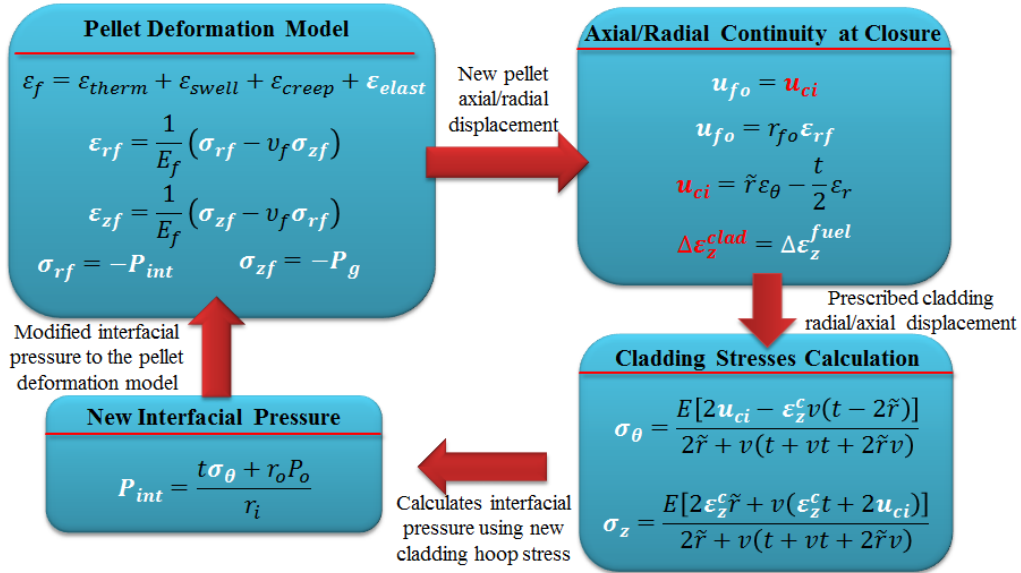


Figure 3.31 Flow chart of the soft-pellet model solution scheme

3.4.3 Fuel Creep

Beside the dominating thermally-induced creep of UO_2 above 1200°C , an irradiation-induced creep also needs to be considered at temperature below 1200°C [46]. This steady-state strain rate was reported to be dependent on the fission rate and stress. The strain rate equation can be expressed by Eq. 37 [48]. The in-reactor creep behavior of UO_2 comprises of an **(a)** high-temperature regime which the normal thermal-induced creep is enhanced by irradiation, and **(b)** a low-temperature regime where the fission process induces athermal creep.

$$\dot{\epsilon}(\text{hr}^{-1}) = A(F)\sigma^{4.5} \exp\left(\frac{-Q}{RT}\right) + A_1(F)\sigma G^{-2} \exp\left(\frac{-Q_1}{RT}\right) + c\sigma F \quad (3.36)$$

where

$$A(F) = \frac{1.38 \times 10^{-4} + 4.6 \times 10^{17}}{-90.5 + \varrho}$$

$$A_1(F) = \frac{9.73 \times 10^6 + 3.24 \times 10^{-5} F}{-87.7 + \varrho}$$

$$Q = 552.3 \text{ kJ/mol}$$

$$Q_1 = 376.6 \text{ kJ/mol}$$

$$C = 7 \times 10^{-23}$$

$$G = 10 \text{ } \mu\text{m (grain size)}$$

ϱ = use % TD if above 92%, otherwise use 92%

$R = 8.314 \text{ J/mol-K (universal gas constant)}$

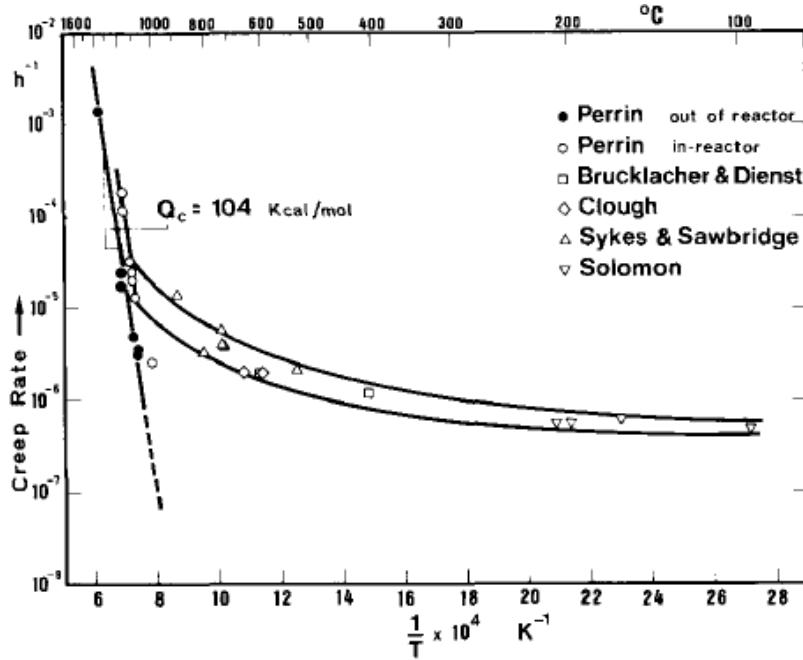


Figure 3.32 Creep of UO_2 vs. temperature (stress of 24 N/mm^2 and fission rate of $1.2 \times 10^{13} \text{ fission/cm}^3 \text{ s}$)

It is found in **Fig. 3.32** that the temperature between 1200 and 500 °C, the in-reactor creep is always greater than the out-of-reactor creep, and it is always temperature dependent. Below 500 °C the creep rate is athermal. These two regions are called the irradiation-enhanced thermal creep and the irradiation-induced creep [49].

Hard-contact between fuel and cladding creates large interfacial pressure which then accelerates the steady-state creep rate; however, pellet fragments can only creep down if there are any remaining spaces. Creep rate reduces the overall swelling rate, and ultimately results a longer soft-contact regime and a lower interfacial pressure. Creep will continue to have an effect until all void spaces have been consumed.

$$\dot{\epsilon}_{creep} = \dot{\epsilon}_{swell} \quad (3.37)$$

The stress exerted on the fuel pellet surfaces increases due to hard-contact, and the fuel creep rate will achieve the swelling rate eventually. The critical stress, σ_c , can be determined from the corresponding interfacial pressure. The overall effects of irradiation-induced creep on PCMI are the extended soft-contact and reduced buildup of interfacial pressure which is predicted in **Fig. 3.33**.

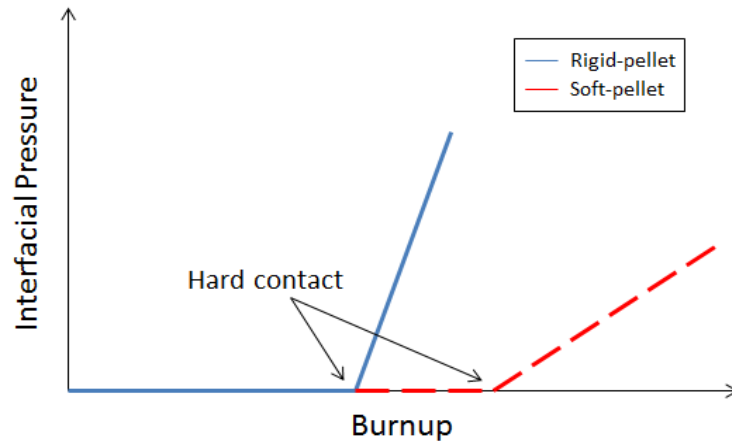


Figure 3.33 Interfacial pressure vs. burnup plot of the rigid-pellet and soft-pellet model

CHAPTER IV

RESULTS AND DISCUSSION

4.1 Low Burnup Test Case

With the implementation of SiC properties, the modified FRAPCON-3.4, hence called FRAPCON-USC, is now capable of predicting the performance of the monolithic SiC-clad fuel rods. Two test cases with different power histories were selected to predict the fuel behavior. Constant power low-burnup test case removes the disruption due to sudden power level change and the extreme effects of large fission gas release due to higher burnup. It can reveal the possible advantages and concerns of applying SiC-clad fuels in current operating condition. The high-burnup test case provides insight into the fuel rod behavior in the operations where the monolithic SiC-clad fuel is needed to exceed the performance of the conventional Zircaloy-clad fuel.

The design parameters are the same for both SiC and Zircaloy fuel rods, as indicated in **Table 4.1**. These dimensions represent a typical 17x17 assembly PWR design, which is a more practical case for modeling fuel performance under LWR condition.

Table 4.1.1 Initial fuel and cladding dimensions for both cladding design

Dimension	Units	Value
Cladding OD	cm	0.9144
Cladding ID	cm	0.8
Cladding thickness	cm	0.0572
Gap width	cm	0.0079
Fuel pellet diameter	cm	0.7842
Fuel stack height	m	3.6576
Fuel rod pitch	cm	1.2598
Filled gas pressure	MPa	2.41
Coolant pressure	MPa	15.51
Inlet temperature	K	564.43
Neutron flux	n/m ² s	2.21 x 10 ¹⁶

4.1.1 Constant power analysis:

Case 1 is a PWR test case with power history of a constant LHGR of 16.4 kW/m as shown in **Fig. 4.1**. The fuel rod is discharged at a burnup of 56 GWD/MTU after 1500 days as shown in **Fig. 4.2**. The first major difference between the SiC and Zircaloy cladding is the thermal conductivity. Plotted in **Fig. 4.3**, the thermal conductivity of SiC degrades significantly from 117 W/m-K at BOL to a saturated value of 3.6 W/m-K after 1 dpa due to the accumulation of the irradiation-induced defects. Since the cladding temperature does not fluctuate largely during operation, as the thermal conductivity of Zircaloy stays close to 16 W/m-K. At discharge, the thermal conductivity of SiC is less than Zircaloy by a factor of 4.6.

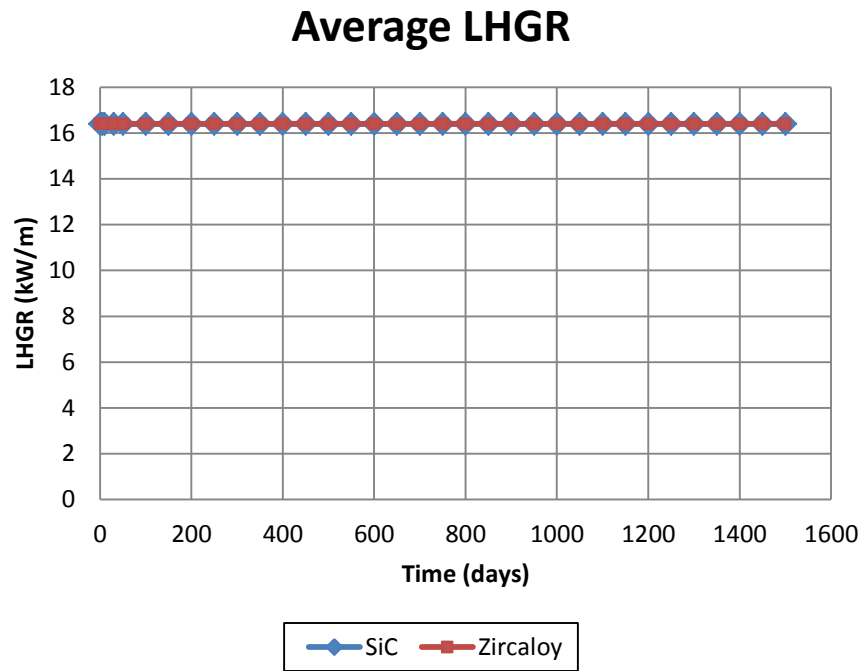


Figure 4.1 Linear heat generation rate vs. time

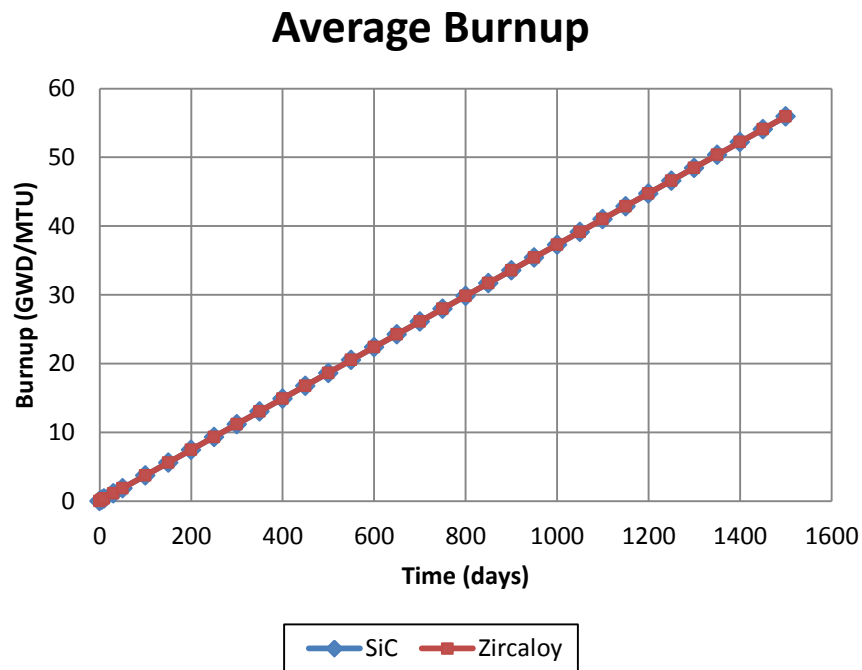


Figure 4.2 Average burnup vs. time

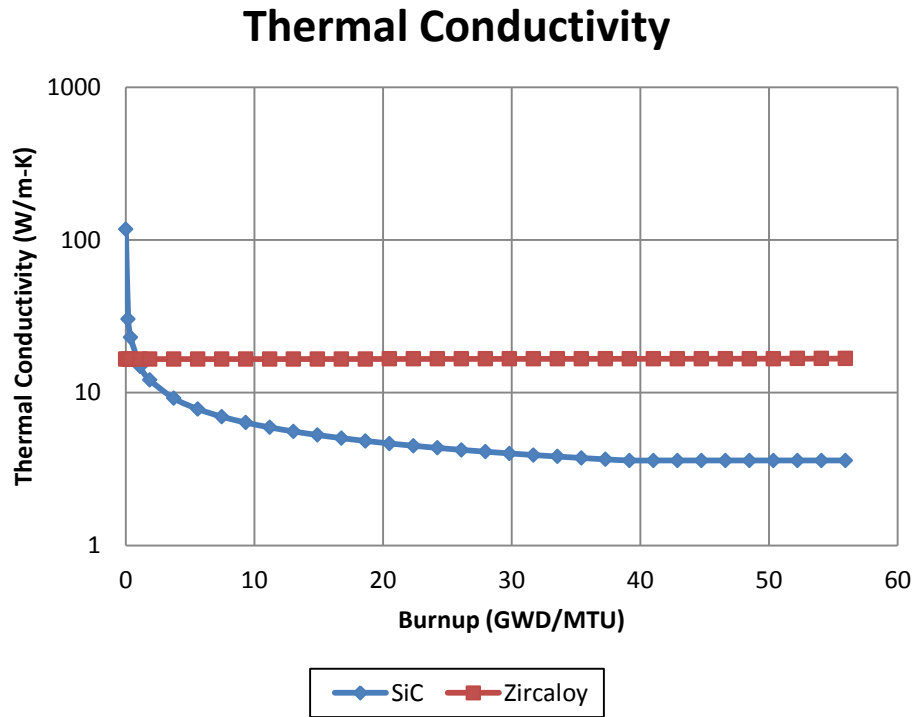


Figure 4.3 Cladding thermal conductivity degradation vs. burnup

4.1.2 Fuel/Cladding temperature

The drawback of lower thermal conductivity is the larger temperature drop across the cladding, and therefore increases the average temperature of the fuel as shown in **Fig. 4.4** and **4.5**. The inner cladding temperature of SiC is hotter than Zircaloy by 60 K at EOL, while the fuel centerline and surface temperatures of SiC are around 80 K hotter than the value for Zircaloy.

Cladding Temperature

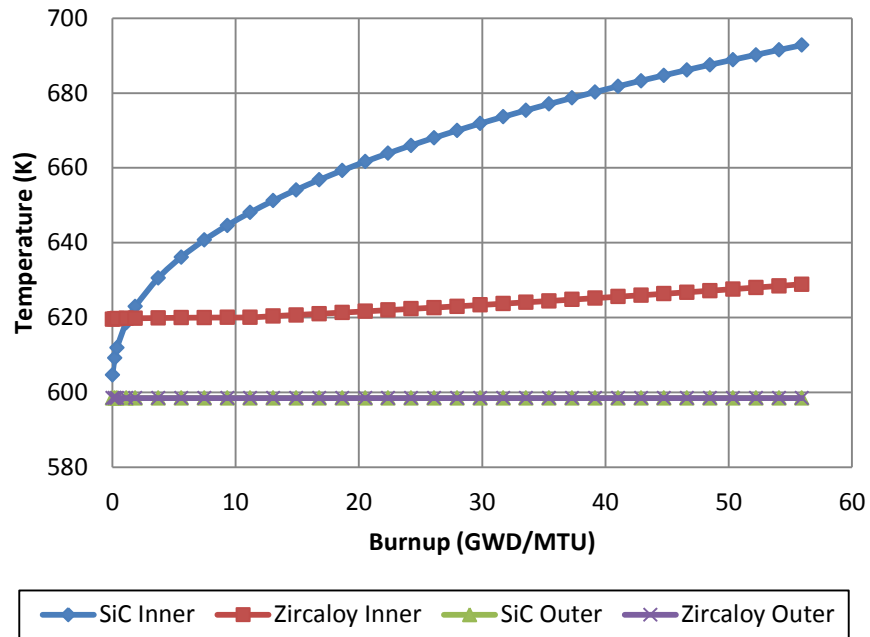


Figure 4.4 Cladding inner/outer surface temperature vs. burnup

Fuel Temperature

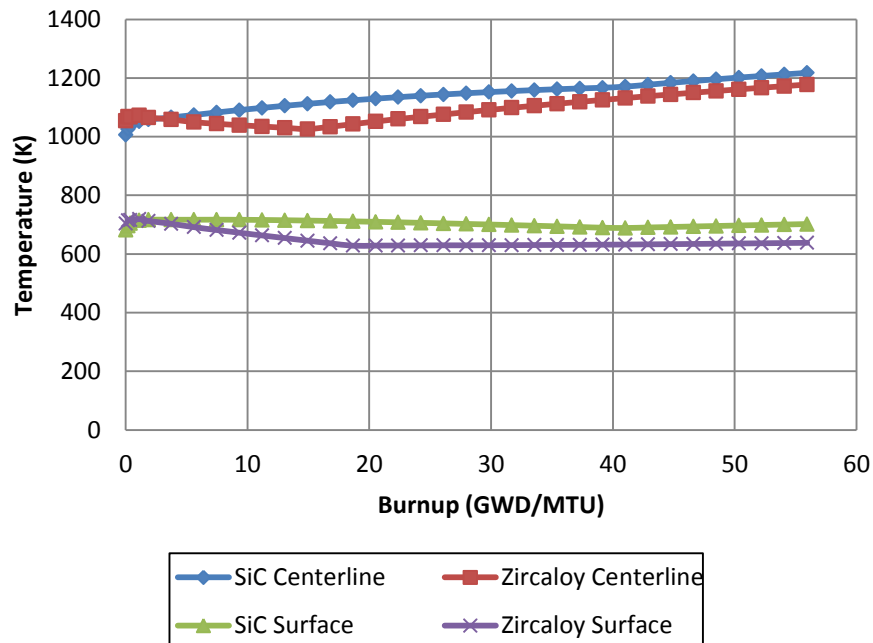


Figure 4.5 Fuel centerline/surface temperature vs. burnup

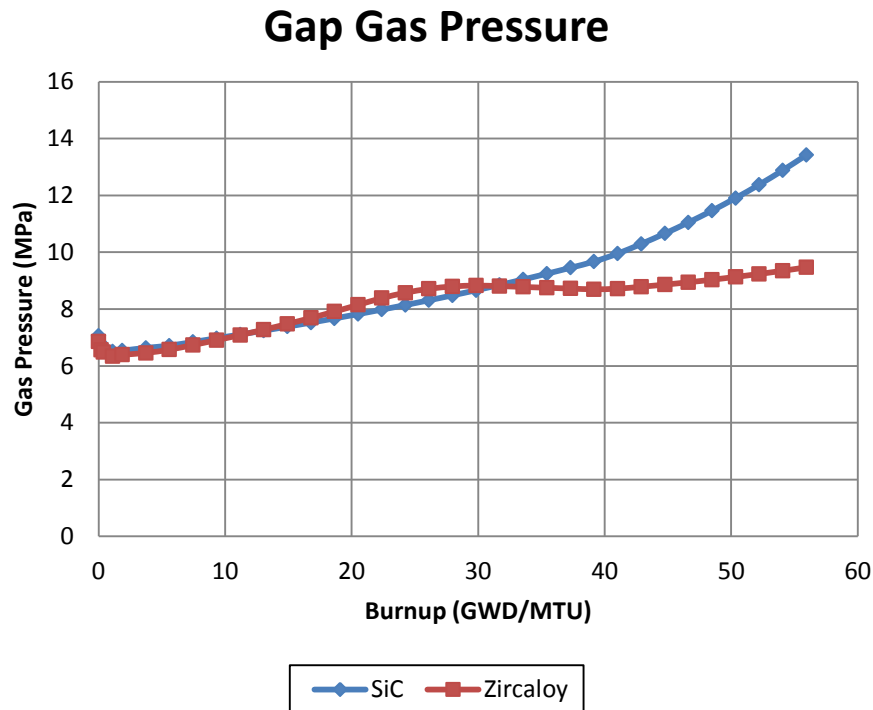


Figure 4.6 Gap gas pressure vs. burnup

4.1.3 Pellet-cladding gap width

The pellet-cladding gap width increases initially due to the densification of the fuel pellet shown in **Fig. 4.7**. After the as-fabricated pellet porosity is consumed, fuel swelling will start to serve as the dominating mechanism for fuel expansion. In addition, Zircaloy cladding begins to creep inward to the fuel achieving soft-contact with the pellet at 18.65 GWD/MTU, and eventually reaching hard-contact at 26.1 GWD/MTU. However, for SiC cladding with negligible creep, soft-contact occurs at a much higher burnup of 41 GWD/MTU, and no hard-contact was observed. The gap width of SiC-clad fuel rods is only determined by fuel swelling, thermal expansion, and cladding deformation caused by the coolant/gap pressure difference.

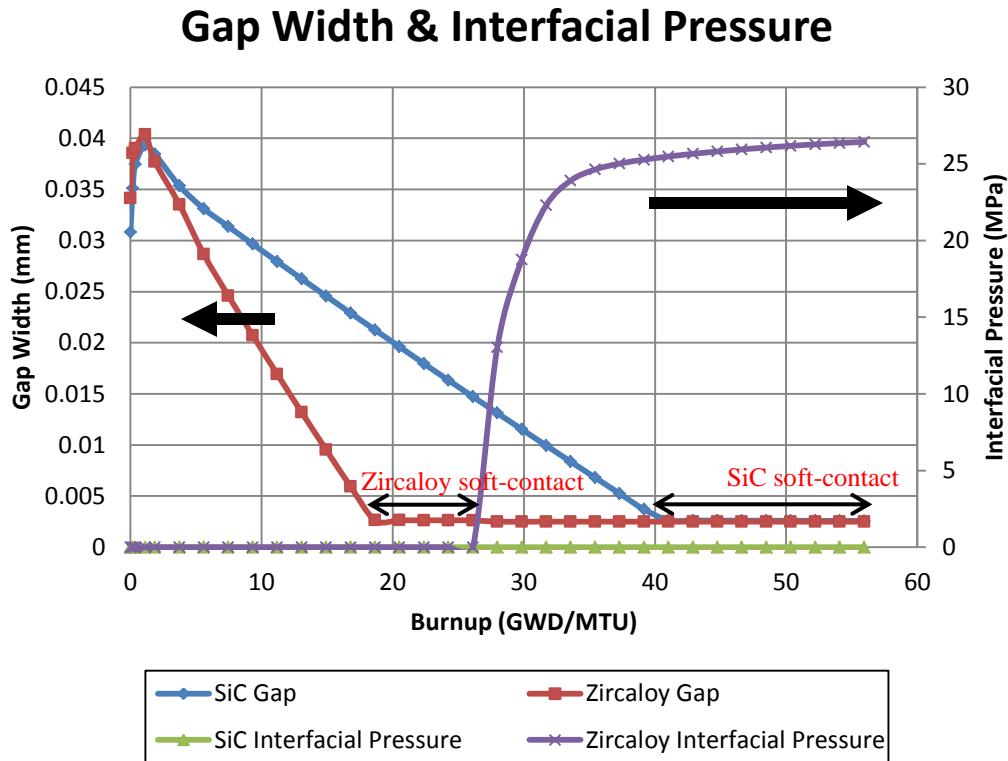


Figure 4.7 Gap width & interfacial pressure vs. burnup

4.1.4 Interfacial pressure

The buildup of interfacial pressure at the interface between pellet and cladding is observed at a low burnup of 26.1 GWD/MTU for Zircaloy fuel rods. Initially, the interfacial pressure between the relocated pellet fragments and the cladding is low, due to the closure of some cracks. This is called the soft-contact regime, and only after this regime will FRAPCON starts to calculate the interfacial pressure. As cladding continues to creep down, and after recovering 50% of the relocated pellet strain, hard-contact will ultimately occur. Other mechanisms such as fuel swelling and expansion may also accelerate this process.

Interfacial pressure builds up quickly with burnup after hard-contact achieving a maximum stress of 26 MPa at EOL. Hard-contact between pellet and cladding is not

necessarily unacceptable if the cladding is able to relieve the excessive accumulated stresses by creep and plastic deformations. As a result, high interfacial pressure will increase the cladding hoop stress, and leads to the transition of cladding state from compressive to tensile. The cladding is initially at a compressive state before contact because the gap gas pressure, shown in **Fig. 4.6**, is much lower than that of the external coolant. However, the buildup of interfacial pressure along with a minor contribution of fission gas release will decrease the magnitude of compressive cladding hoop stress as shown in **Fig. 4.8**. Beyond burnup of 28 GWD/MTU, the cladding will be in a tensile state that is favorable for stress-corrosion cracking.

Fig 4.9 shows the hoop strain of both claddings. The transition from compressive to tensile strain occurs again at the moment of hard-contact. The overall insignificant hoop strain of SiC cladding is a result of its high elastic modulus and a lower hoop stress (30 MPa in compression at EOL).

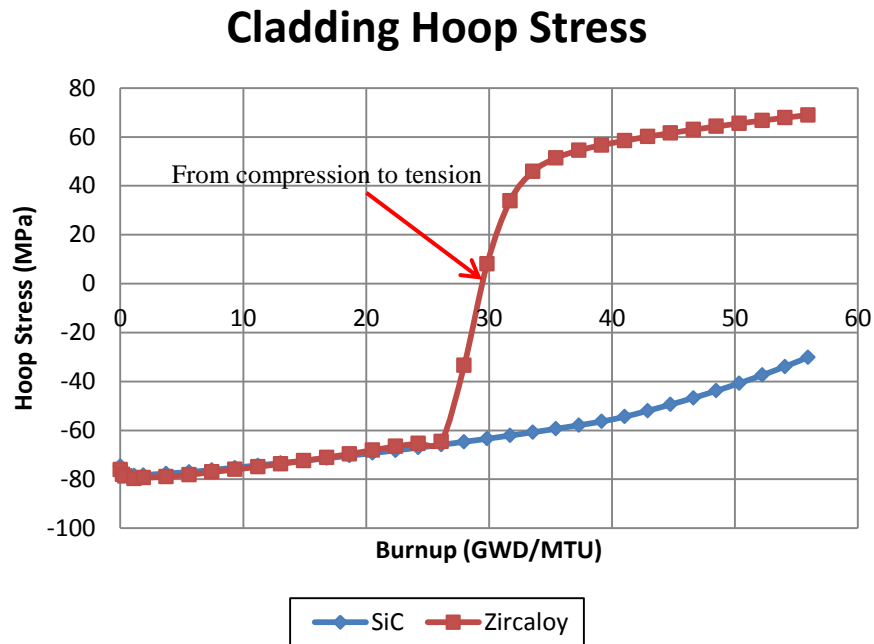


Figure 4.8 Cladding hoop stress vs. burnup

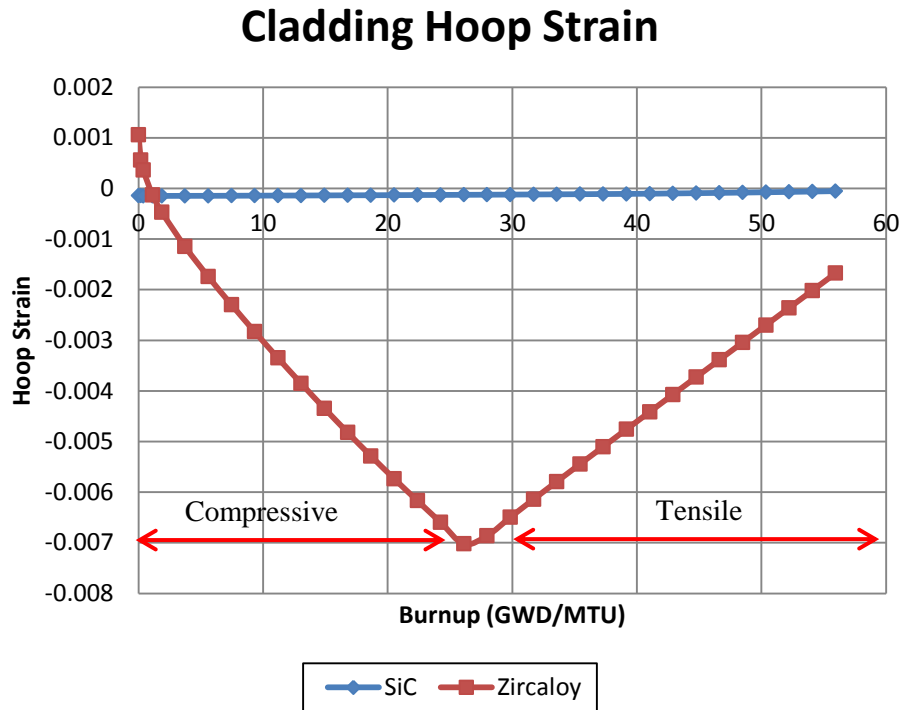


Figure 4.9 Cladding hoop strain vs. burnup

4.1.5 Consideration of fuel pellet deformation

FRAPCON uses the rigid pellet model for PCMI calculations. After hard-contact, only the cladding deformations will be calculated, there is no feedback stresses to the pellet deformation model. FRAPCON also assumes that there is no axial slip of the pellet once the gap has closed.

The fuel pellet cracking and relocation are taken into account to adjust the thermal model based on the assumption of **relocation strain recovery**, which implicitly accounts for the partial recovery of the radial cracks. However, FRAPCON does not consider the effect brought by the compressive fuel surface pressure as shown in **Fig. 4.10**. Before hard-contact, fuel surface pressure is indicated by the gap gas pressure and will be dominated by interfacial pressure after contact. In current model, this fuel surface

pressure will deform the UO_2 pellet elastically and serve as one of the sources for fuel creep (with irradiation and temperature). Since only 50% of the relocation strain is recovered at the soft-contact regime, it is assumed that the pellet can still deform inwards at the hard-contact regime due to the remaining 50% void spaces.

In this analysis, the elastic deformation and the thermal/irradiation-induced creep of the UO_2 fuel are calculated using the corresponding UO_2 material properties under current operating condition. Their effect is later considered in the fuel deformation model.

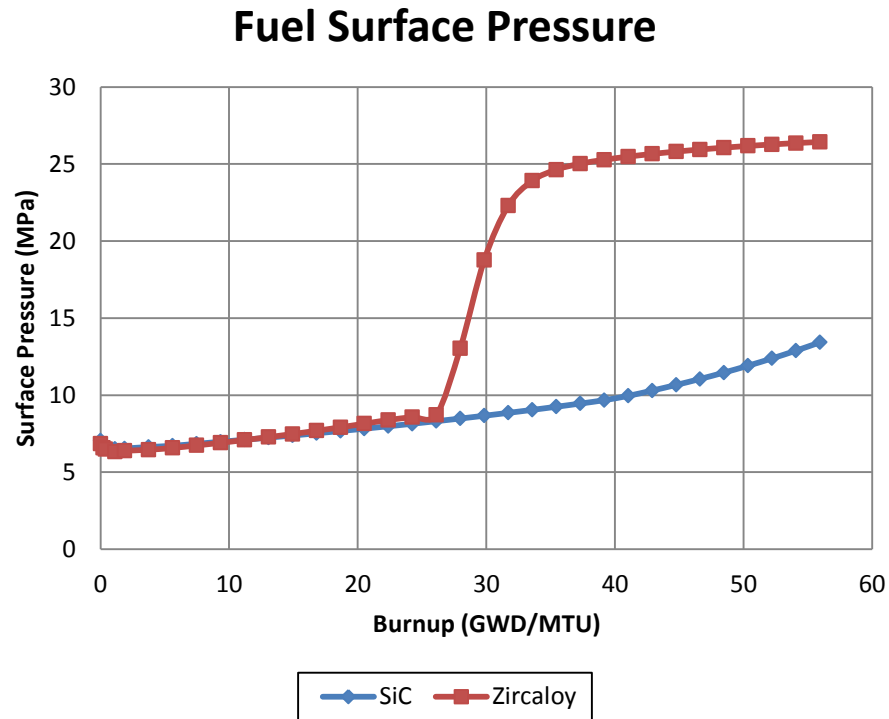


Figure 4.10 Fuel surface pressure vs. burnup

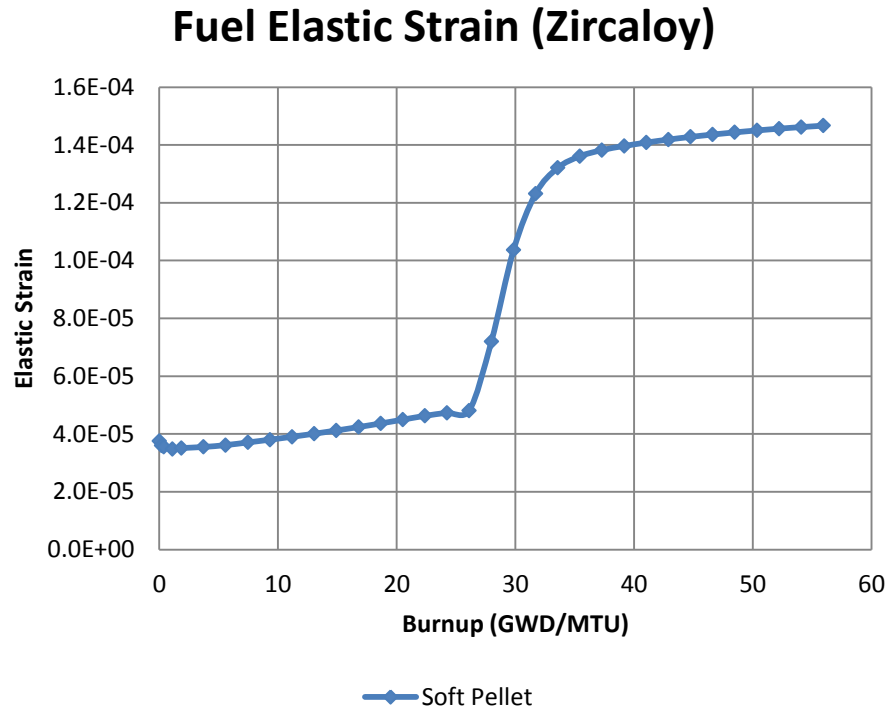


Figure 4.11 Fuel pellet elastic deformation due to fuel surface pressure

4.1.6 Fuel creep

The steady-state creep of UO_2 can be categorized into three regimes: the low-stress, intermediate/high-stress, and the irradiation-induced creep regime. It is well-known that in ceramic materials, the thermally-induced creep will not serve as the dominate mechanism until temperatures higher than $0.5T_m$ (~ 1600 K). This behavior is clearly demonstrated in **Fig. 4.12**, where the fuel temperature in case 1 is below $0.5 T_m$, and the thermally-activated creep rate is smaller than the irradiation-induced creep rate by 4 to 10 orders of magnitude.

The outward fuel swelling of Zircaloy-clad is affected by the additional fuel inward creep. As shown in **Fig. 4.13**, the effect of this stress-activated creep to the swelling rate is insignificant. The fuel creep of SiC-clad is ignored due to its small fuel

surface pressure. However, if the interfacial pressure, fuel temperature, or neutron flux are higher, the inward creep rate may be significant and therefore retard the swelling rate to some degree.

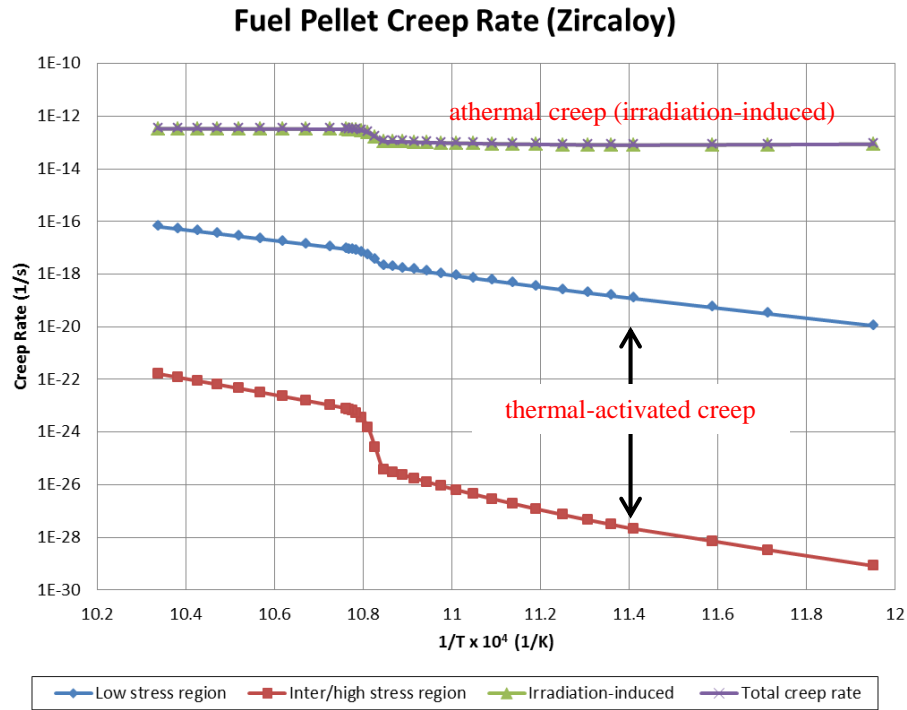


Figure 4.12 UO_2 steady-state creep rate vs. $1/T$

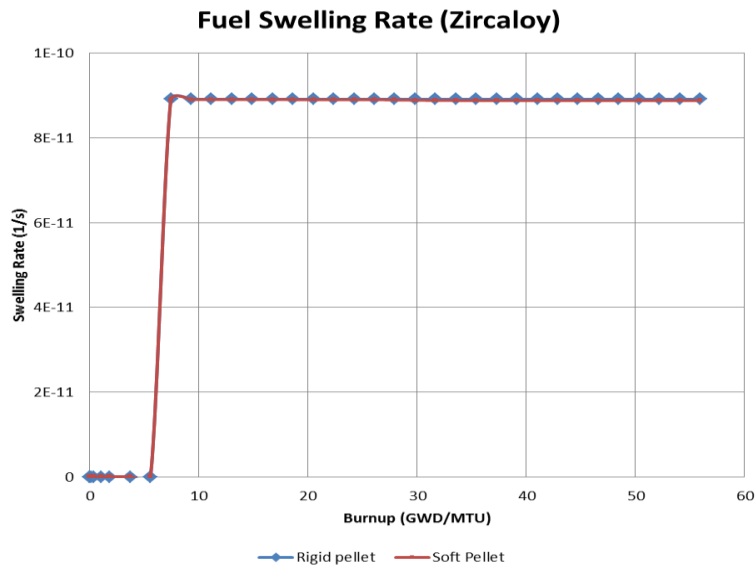


Figure 4.13 Fuel swelling rate using rigid and soft pellet model vs. burnup

4.1.7 Fuel radial displacement using soft-pellet model

The fuel pellet radial displacement using the soft-pellet model is calculated and compared with the result of rigid-pellet model, as shown in **Fig. 4.14**. The radial displacement difference between the two models is insignificant, with merely a $1.5\ \mu\text{m}$ difference at EOL. This small value is due to the lower fuel surface pressure and the negligible thermal-induced creep.

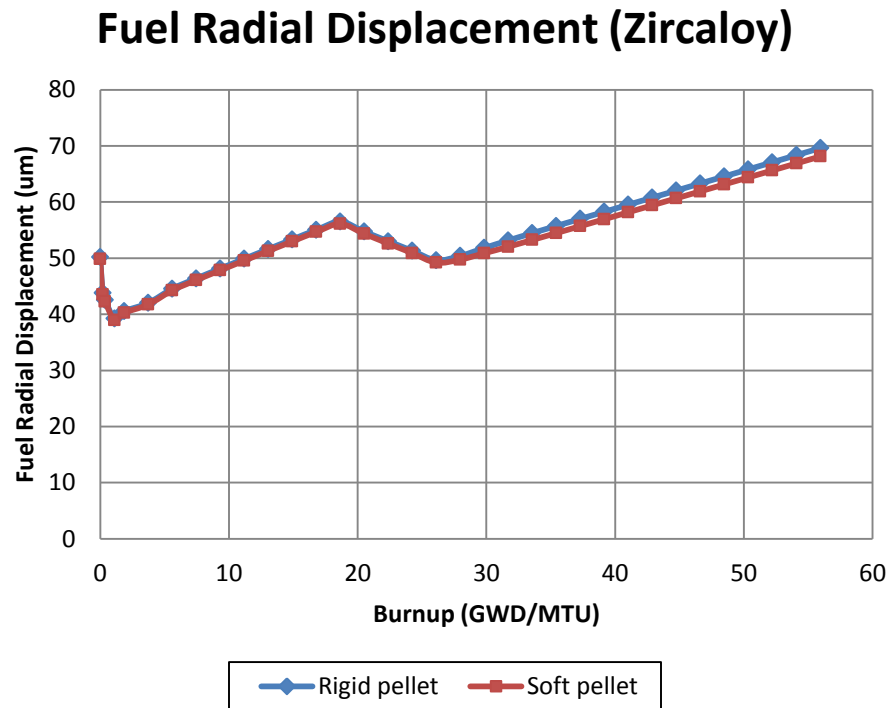


Figure 4.14 Fuel radial displacement using rigid and soft pellet model vs. burnup

4.1.8 Critical interfacial pressure for fuel swelling rate

In FRAPCON's fuel deformation model, fuel swelling serves as the major deformation mechanism after densification and thermal expansion at BOL. However, if the interfacial pressure from the cladding is high enough, there is a possibility for the inward creep to partially or even fully accommodate the outward swelling. This critical

interfacial pressure can be calculated using **Eq. 4.1** and **4.2**, where the thermally-induced terms are neglected due to their insignificant value. The irradiation-induced creep is comprised of three factors: creep compliance B , applied stress σ , and the neutron flux F . Creep compliance for UO_2 pellet is an experimental value reported by Solomon and Brucklacher [50, 51], the neutron flux is set as a constant in the FRAPCON modeling, therefore, the only variable for the irradiation-induced creep is the applied stress resulting from interfacial pressure.

$$\dot{\epsilon}_{creep} = \dot{\epsilon}_{swell} \quad (4.1)$$

$$\dot{\epsilon}_{swell} = B\sigma F \quad (4.2)$$

where

$B = 3.79 \times 10^{-24}$ (creep compliance, no unit)

σ = applied stress on the fuel surface, coming from the interfacial pressure (MPa)

F = neutron flux ($\text{n/cm}^2\text{s}$)

Provided a constant neutron flux to the calculation, $2.21 \times 10^{16} \text{ n/m}^2\text{s}$, the critical stress for full accommodation of fuel swelling can be obtained, with an extremely high value of **7000 MPa**. This stress level is well beyond the interfacial pressure created from the hard-contact of UO_2 pellet with Zircaloy cladding. From previous analyses, considering the fuel as a deformable, soft pellet does not create a significant difference compare to the current assumption of a rigid pellet, shown in **Fig. 4.1.14**. Therefore, the application of the soft-pellet model to the PCMI analysis may not be of practical use for UO_2 -Zircaloy fuel rod.

4.2 High-Burnup Constant Power Analysis

The low-burnup constant power test case provides an insight to the performances of the SiC-clad fuel rods without the effect of PCMI, due to the delayed gap closure of SiC-clad fuel rods. A second analysis using a high-burnup constant power test case is carried out to extend the burnup of the fuel rod, so that PCMI (particularly hard-contact) between the fuel pellet and the ceramic SiC cladding eventually occur. The distinctive material properties of the SiC such as high stiffness, lower thermal expansivity, and negligible creep and plastic deformation may lead to distinctive PCMI effects.

4.2.1 Power History

The power history for this high-burnup test case is the same for both Zircaloy and SiC fuel rods, using a constant linear heat generation rate of 16.4 kW/m. The discharge burnup is 64 GWD/MTU after 1730 effective full-power days, which is shown in **Fig. 4.2.2**. This burnup is 8 GWD/MTU higher than the previous test case, with a discharge burnup of only 56 GWD/MTU, typical of most commercial PWRs in the United States. However the trend is toward higher burnup to accommodate power uprates and longer cycle lengths.

Burnup and fission gas release as a function of time is plotted **Fig. 4.16**, it is also indicated that the fission gas release is dependent of burnup. Two distinctive regimes were observed, a moderate fission gas production rate at lower burnup, and transit on a rapid release rate after 39 GWD/MTU.

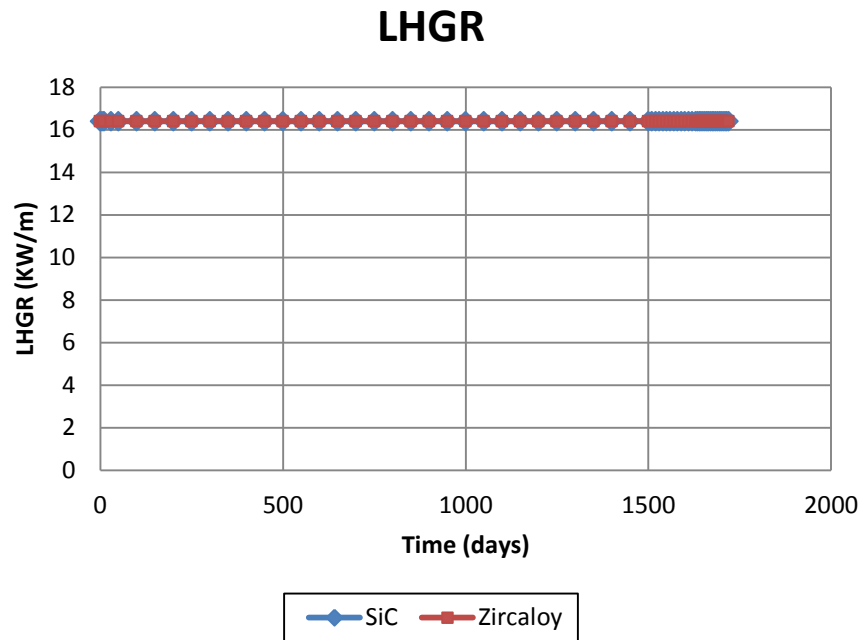


Figure 4.15 Linear heat generation rate vs. time

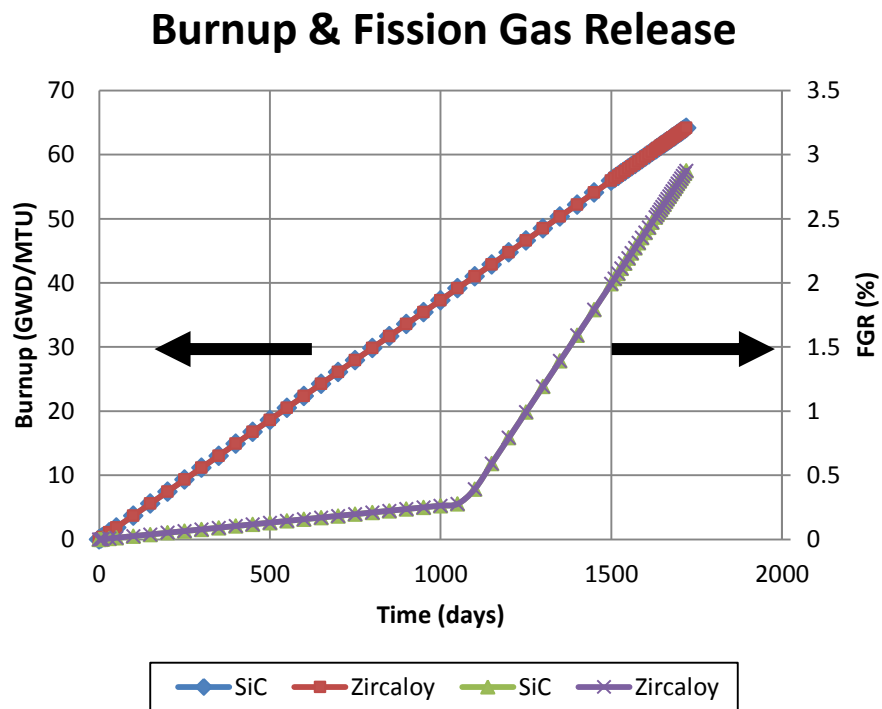


Figure 4.16 Average burnup & fission gas release vs. time

4.2.2 Thermal Conductivity

The degradation of thermal conductivity behaves in a similar fashion as the lower-burnup test case, shown in **Fig. 4.17**. In both cases, the DPA increases monotonically with burnup, therefore, the strongly DPA-dependent SiC thermal conductivity will show similar degradation behavior.

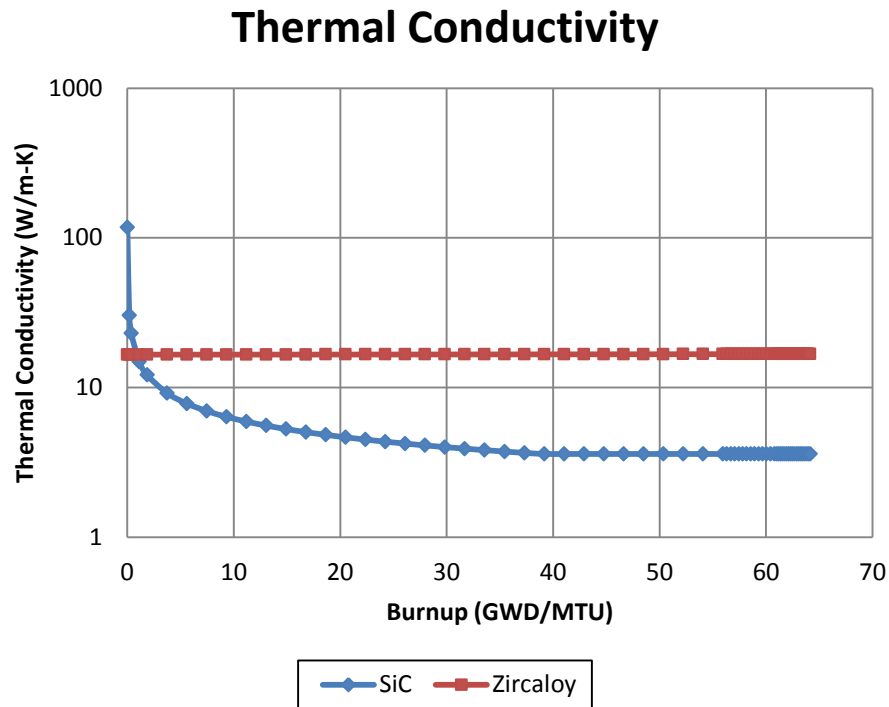


Figure 4.17 Degradation of thermal conductivity vs. burnup

4.2.3 Gap Width

The lack of creep in SiC cladding allows soft-contact to exist for 510 days after first contact, as indicated in **Fig. 4.18** and **Table 4.2**. Compared to Zircaloy cladding, SiC cladding extends the soft-contact regime by 310 days. The extension of the soft-contact regime is because now the assumption for 50% recovery of the relocation strain is only attributed by fuel swelling, whereas for Zircaloy cladding, it is recovered by fuel swelling and cladding inward creep. In addition, the time for soft-contact is also delayed by 600

days. Overall, SiC cladding fuel rod results in a delayed occurrence of PCMI and a extended time of soft-contact.

One should notice after hard-contact, the significant rise of interfacial pressure. This phenomenon was discussed previously for the hard-contact of Zircaloy, however, now the interfacial pressure accumulation is much more severe for SiC cladding, due to its high elastic modulus and lower degradation with temperature and irradiation. At EOL, the interfacial pressure for SiC cladding is 64.15 MPa, which is 2.3 times larger than what of Zircaloy cladding.

Significant interfacial pressure buildup causes the cladding hoop stress to also increase rapidly with hard-contact, and this behavior is again more severe for SiC cladding as shown in **Fig 4.19**. After the initial increase upon hard-contact, the hoop stress of Zircaloy starts to increase at a moderate rate. This is because of Zircaloy's ability to creep, which relieves the excessive accumulated stress coming from fuel swelling. SiC's deficiency to creep will allows the accumulation of stress on the cladding until it finally fails. Monolithic SiC cladding fails in a brittle fashion immediately upon reaching its maximum flexural strength, which has a lower limit of 260 MPa from reports by Ross et al.[9].

Cladding hoop stress again shows the same trend from compressive to tensile after hard-contact. The magnitude of SiC hoop strain is very small, shown in **Fig. 4.20**, until reaching hard-contact. After hard-contact, the compressive-to-tensile transition soon occurs. Tensile stress in SiC may leads to stress corrosion cracking, which is another major failure mechanism for cladding. The effect of stress corrosion cracking is not in the scope of focus in this research.

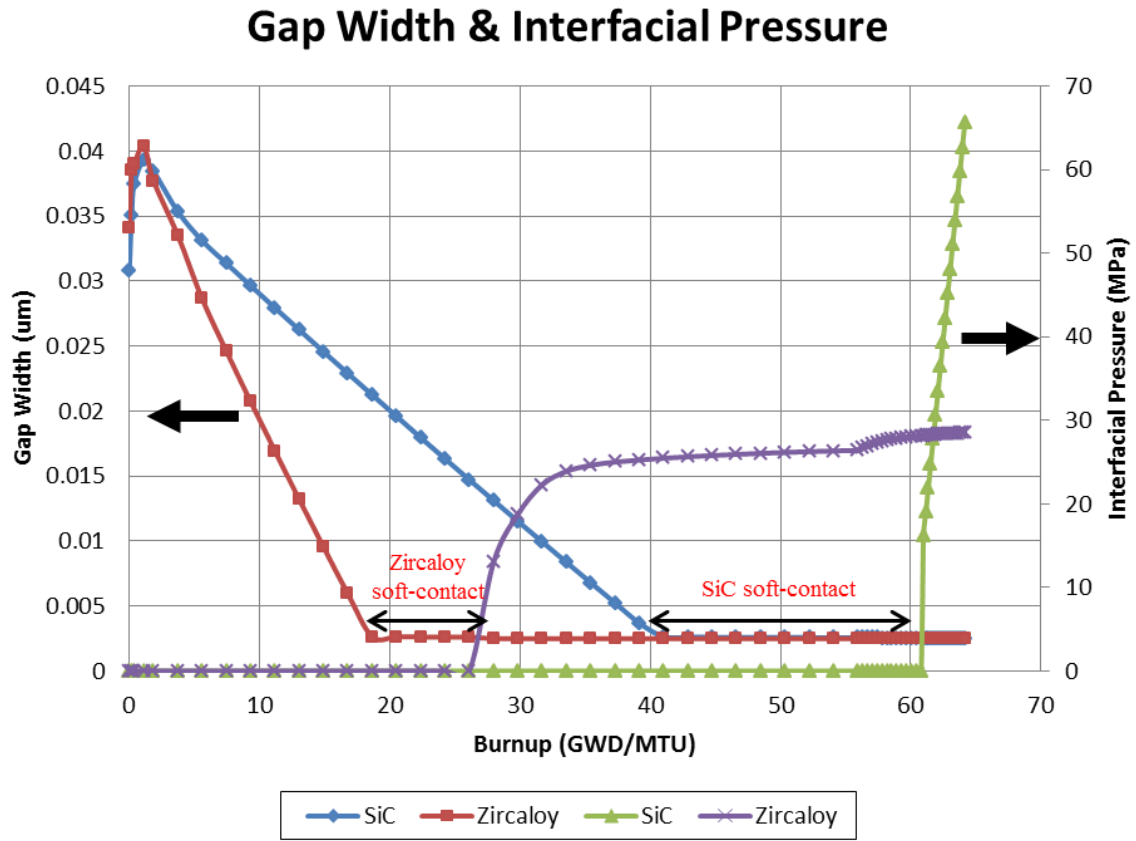


Figure 4.18 Gap width & interfacial pressure vs. burnup

Table 4.2 Time & burnup comparison for soft/hard contact in Zircaloy/SiC clad fuel

Cladding type	Soft contact	Hard contact
Zircaloy	18.6 GWD/MTU (500 days)	26.1 GWD/MTU (700 days)
SiC	41 GWD/MTU (1100 days)	60 GWD/MTU (1610 days)

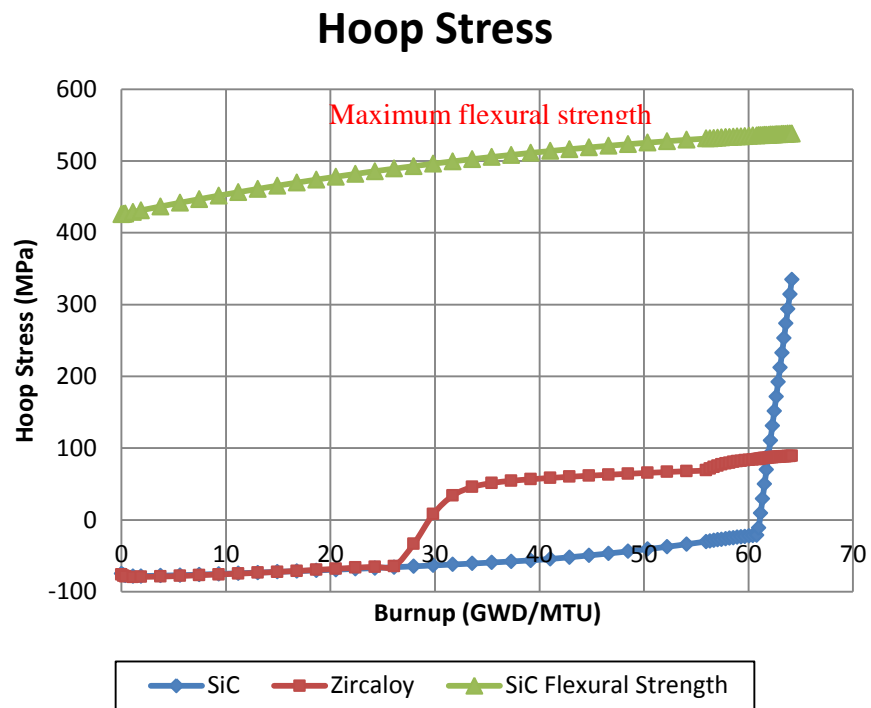


Figure 4.19 Cladding hoop stress vs. burnup

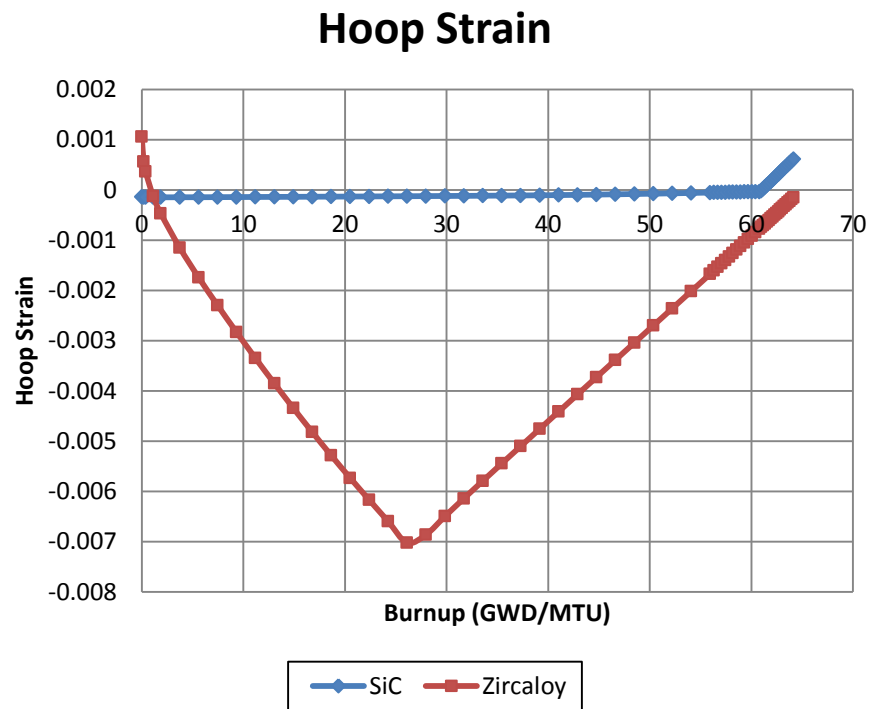


Figure 4.20 Cladding hoop strain vs. burnup

4.2.4 Fuel Radial Displacement vs. Gap Width

The fuel radial displacement is plotted with gap width in **Fig. 4.21** to demonstrate how FRAPCON models the soft-contact regime with the assumption of relocation strain recovery during soft-contact. For fuel rods with distinctive material properties, soft-contact always occurs at initial gap closure. During soft-contact, pellet deforms differently: Zircaloy pellet shrinks and SiC pellet expands in a very small rate. The shrinkage of pellet is due to the reduction of fuel swelling that is caused by cladding inward creep and relocation strain accommodation. Since SiC cladding does not creep down, this additional relocation strain will only be accommodated by fuel swelling, which results a longer time for the recovery of the 50% of relocation strain.

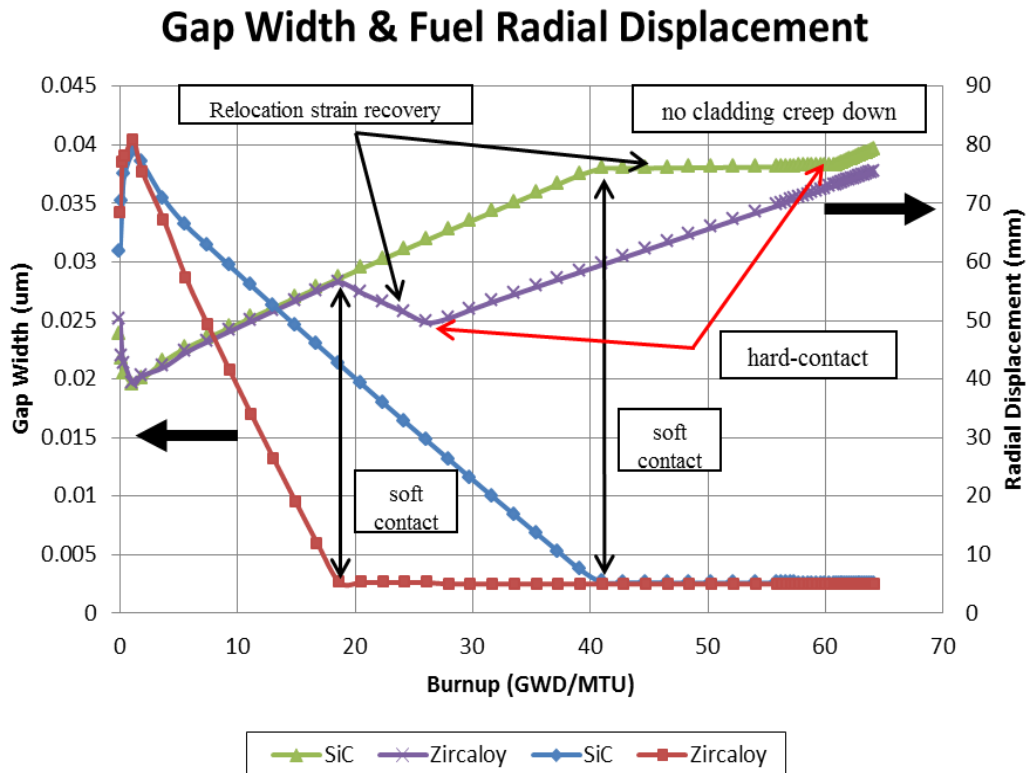


Figure 4.21 Gap width & fuel radial displacement vs. burnup

4.2.5 Fuel Surface Pressure

The fuel surface pressure serves as the driving force for elastic deformation and creep, shown in **Fig. 4.22**. The larger interfacial pressure of SiC fuel rods will exert higher pressure on the fuel surface. Consider UO_2 's high elastic modulus, the corresponding elastic deformation is also very small, shown in **Fig. 4.23**.

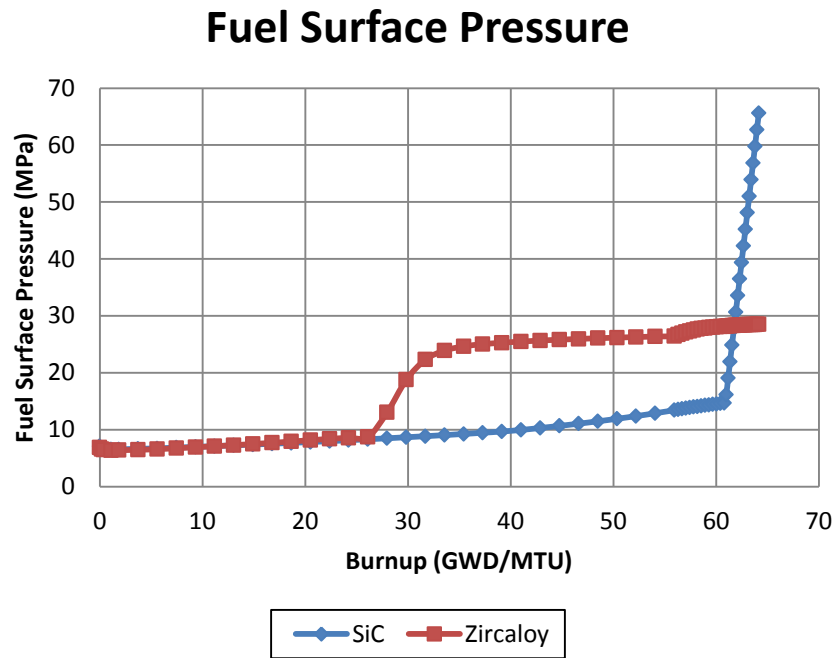


Figure 4.22 Fuel surface pressure vs. burnup

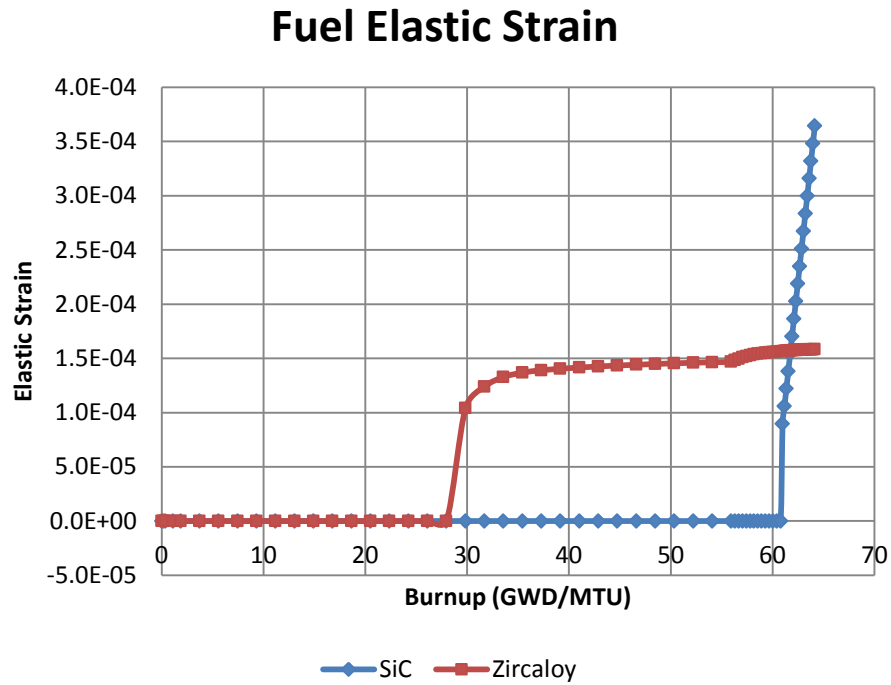


Figure 4.23 Fuel elastic strain vs. burnup

4.2.6 Fuel creep

The steady-state creep rate of UO_2 is presented in **Fig. 4.24**, where the irradiation-induced creep is again the dominating creep mechanism in the low-temperature regime. However, thermal-induced creep will surpass the irradiation-induced creep at higher fuel temperature of 1176 K, which is a result for SiC's lower thermal conductivity. The thermal-induced creep of Zircaloy rod is less significant because of its lower cladding temperature.

The stress-induced fuel strains were then used for calculating additional fuel radial displacement. The results were presented in **Fig. 4.25**, where the compressive stress reduces the displacement by 8.8 μm at EOL. This is higher than the 1.5 μm calculated for Zircaloy in case 1, due to its larger creep rate in UO_2 induced by higher fuel surface pressure and fuel temperature with SiC cladding.

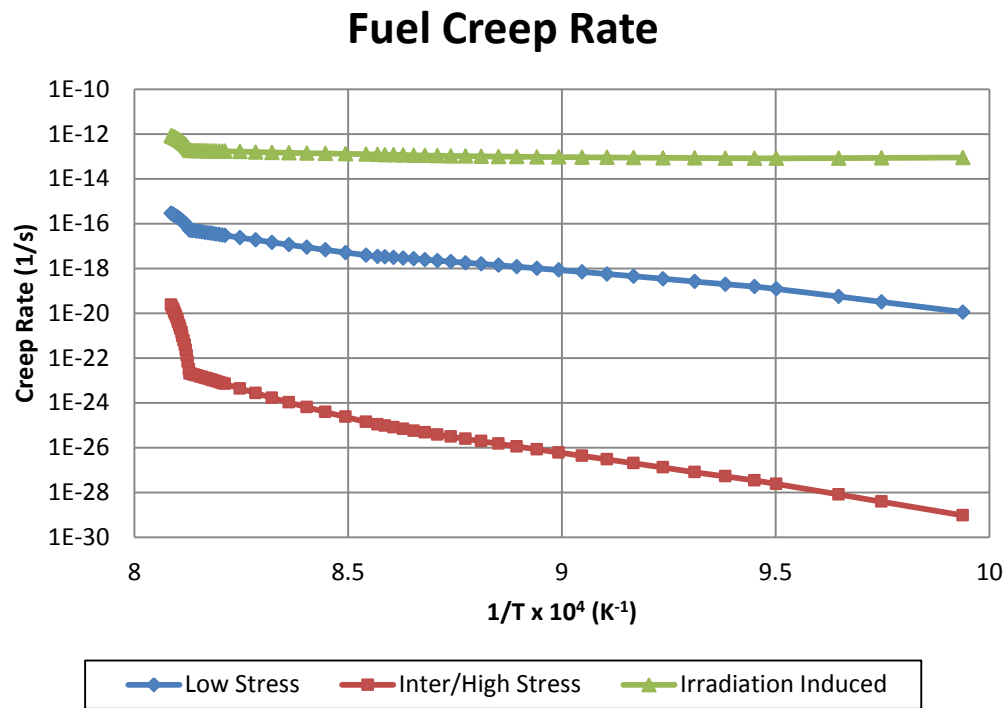


Figure 4.24 UO_2 steady-state creep rate vs. $1/T$

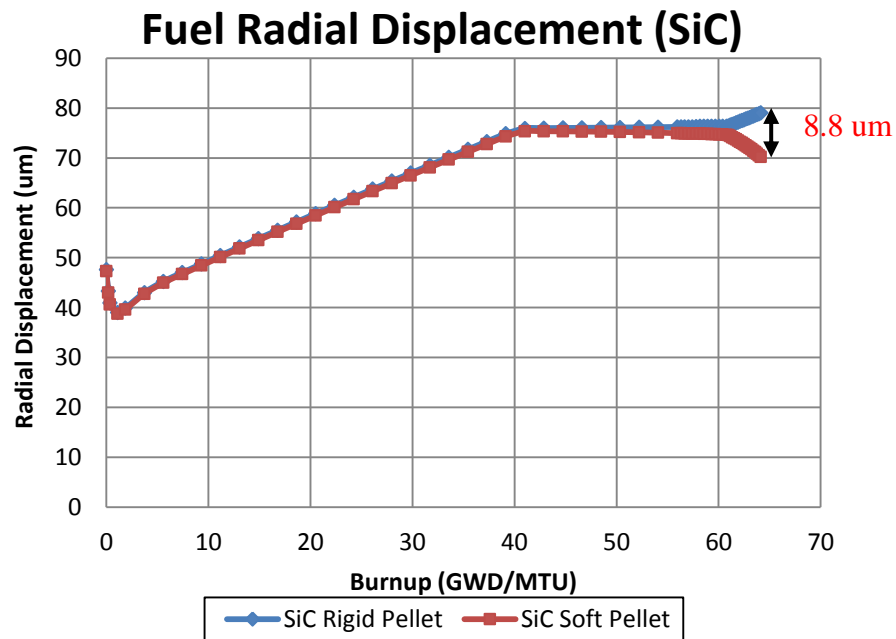


Figure 4.25 Fuel radial displacement using the rigid/soft pellet model vs. burnup

The higher-burnup test case allows for evaluation of PCMI effect to the performances of the SiC-clad fuel rod. Rapid accumulation of interfacial pressure creates larger hoop stress that may eventually lead to cladding fracture once achieving maximum flexural stress. Larger interfacial pressure along with higher fuel temperature also induces a more significant fuel creep, which decreases the fuel radial displacement. The possible effect of the reduced fuel deformation will be discussed in the next section. Overall, PCMI of SiC cladding creates a large interfacial pressure that must be mitigated for applications in LWR fuel rods.

4.3 Improved Modeling of Hoop Stress & Modified Rod Design

Previous results indicated the problem of high interfacial pressure, particularly in ceramic SiC cladding. This will create large hoop stress upon hard-contact with the possibility of complete cladding failure. Two ways are proposed to mitigate this disastrous effect: (1) modify fuel rod design, and (2) reduced pellet deformation. Effects of both approaches are discussed, and the results are compared with the original design.

4.3.1 Fuel Rod Design Modification

Modifying fuel rod design is a possible approach to mitigate the accumulated cladding hoop stress. In the thin cylindrical shell assumption that is adopted by FRAPCON, increasing the thickness of the shell will decrease its hoop stress. Therefore, a fuel rod with larger cladding thickness is used for PCMI calculations, and results are compared with original design.

Table 4.3 Modified fuel rod dimensions

Dimension	Units	Original	Case 1
Cladding OD	cm	0.9144	1
Cladding ID	cm	0.8	0.8
Cladding thickness	cm	0.0572	0.1
Gap width	cm	0.0079	0.0079
Fuel pellet diameter	cm	0.7842	0.7842

(a) Interfacial pressure

Hard-contact takes place earlier, shown in **Fig. 4.26**. Thicker cladding leads to higher fuel temperature because of its higher thermal resistance. As a result, the pellet will be hotter and exhibits larger thermal expansion. Overall, thicker cladding leads to an earlier hard-contact of pellet and cladding.

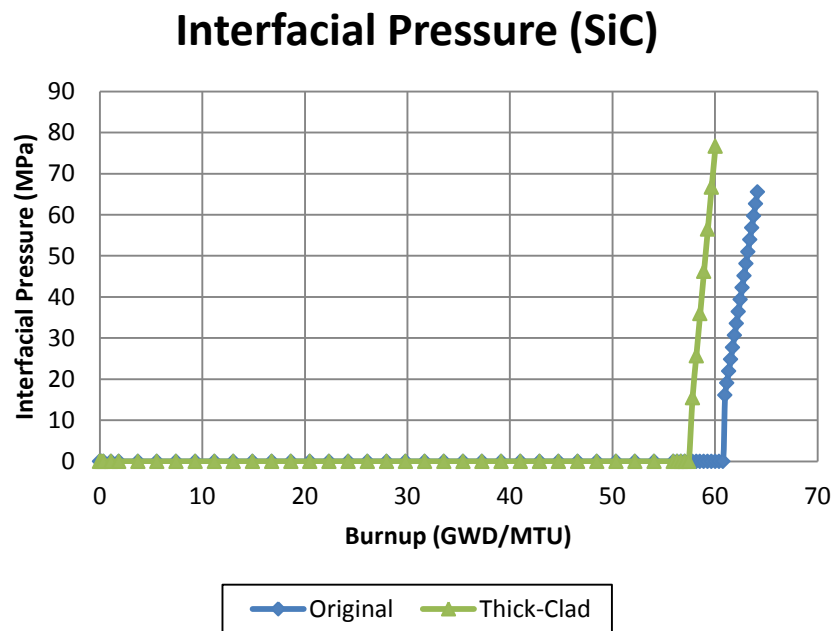


Figure 4.26 Interfacial pressure vs. burnup using thicker cladding

(b) Hoop stress

It is shown in **Fig. 4.27** that cladding hoop stress benefits from thicker cladding by allowing for a smaller magnitude of compressive hoop stress at BOL and a smaller tensile stress at EOL. The hoop stress of the thicker cladding at EOL is decreased to 68% of the value of original design, which is below the maximum flexural strength as indicated. This beneficial result of thicker cladding by allowing lower hoop stress will effectively extend the service lifetime of SiC cladding.

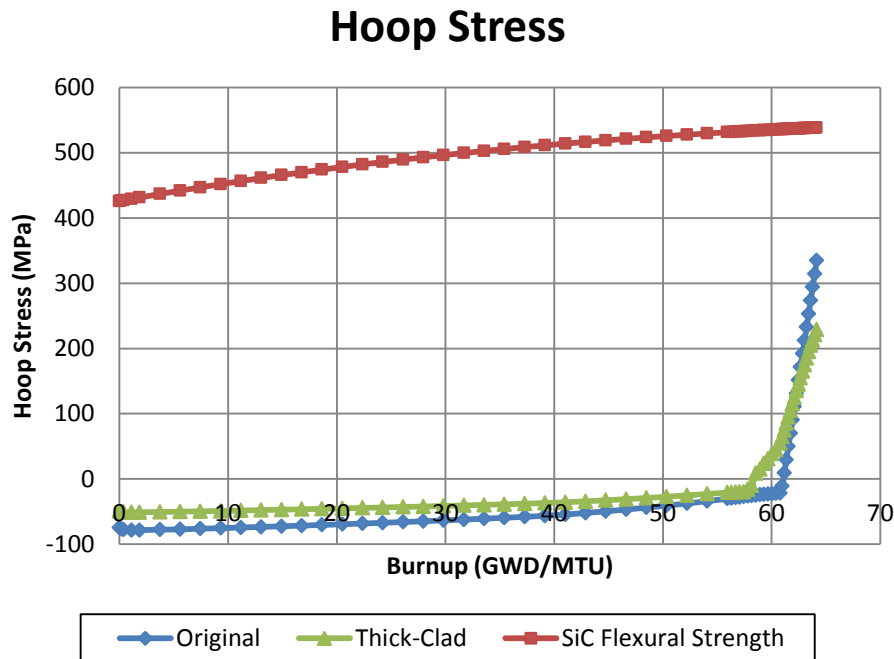


Figure 4.27 Hoop stress vs. burnup using thicker cladding

(c) Rise of fuel temperature

In addition to the beneficial effect of decreased hoop stress, increasing cladding thickness also brings the drawback of higher fuel temperature due to its larger cladding thermal resistance. Indicated in **Fig. 4.28**, the fuel centerline temperature for thicker cladding is about 72 K higher than that of the original design at EOL. This leads to higher

fission gas release and larger thermal expansion of pellet at startup that are generally not favorable for fuel performances.

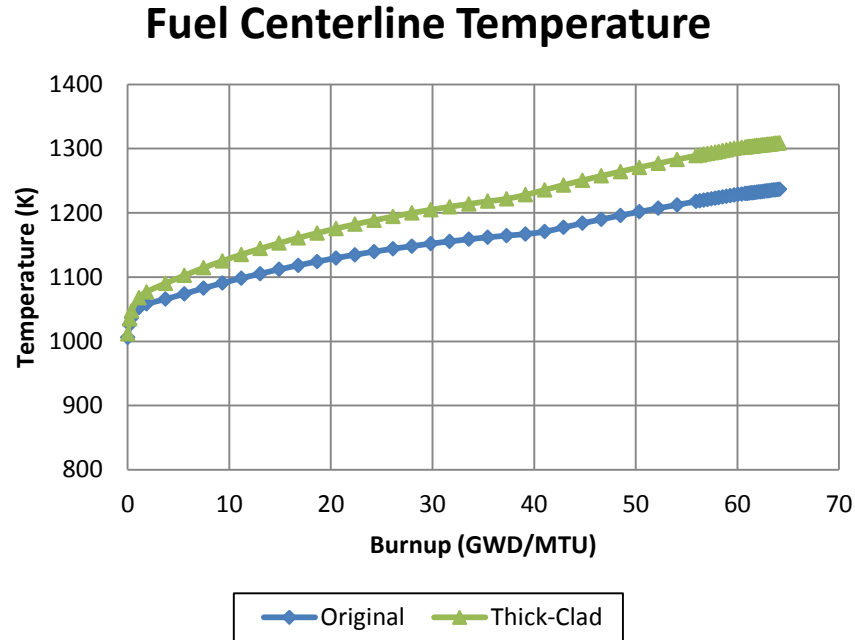


Figure 4.28 Fuel centerline temperature vs. burnup using thicker cladding

4.3.2 Reduced Fuel Radial Displacement

The reduced fuel displacement estimated in the previously will also correspond in reduced cladding displacement. This is to satisfy the closed-gap criterion used in FRAPCON, where the fuel radial displacement must equals to the cladding inner radius. The cladding hoop stress will also be reduced because of the smaller displacement. However, this approach is only developed and has not yet been implemented into FRAPCON-USC. In order to quantify the effect of reduced fuel displacement, the corresponding change in hoop stress should also be evaluated.

Table 4.4 Fuel radial displacement at EOL consider the soft-pellet model

Fuel Radial Displacement (um)	Rigid Pellet	Soft Pellet
Zircaloy	69.616	68.1
SiC	79.031	70.22

CHAPTER V

CONCLUSIONS

5.1 Monolithic Ceramic Cladding Modeling

High-strength ceramic materials such as SiC are considered as one the most promising candidate cladding materials for accident tolerant fuel design. Despite its significant degradation of thermal conductivity, the ceramic SiC possesses a number of advantages including: high melting point, negligible creep under LWR condition, dimensional stability under irradiation, high temperature strength, and low oxidation rate. These favorable properties may allow SiC-clad fuel rods to push beyond the current limits for fuel burnup and operation temperature.

The proposed fuel rod design in this research uses a single monolithic SiC layer that retains the fission gas. Appropriate SiC material properties were implemented into the FRAPCON material module in order to simulate fuel rod performance with monolithic SiC cladding. Hence, the updated fuel performance code, FRAPCON-USC, was developed. FRAPCON-USC models the material properties listed on **Table 5.1.1**, as a function of temperature, neutron flux, and porosity. The models for material properties were obtained from literatures on high-purity CVD SiC.

Table 5.1 Material properties of implemented and their governing factors
(T, Φ , P represents temperature, neutron flux, and porosity)

Material Properties	Governing Factor
Thermal Conductivity	T, Φ
Thermal Expansion	T
Irradiation Swelling	Φ
Elastic Modulus	P, T
Shear Modulus	T
Yields Strength	experimental
Poisson's Ratio	constant
Hardness	P, T
Cladding Creep	T, Φ
Pellet Modulus	T
Pellet Creep	T, Φ

5.1.1 SiC-Cladding Fuel Performances

Two test cases were modeled using the updated FRAPCON-USC code. Case 1 uses a constant LHGR of 16.4 kW/m with a discharge burnup of 52 GWD/MTU, and Case 2 uses the same LHGR but to a higher burnup of 64 GWD/MTU. The significant degradation of thermal conductivity and negligible creep are among the most distinctive properties. The following advantages of SiC cladding fuel rods were clearly indicated when compared with the traditional Zircaloy cladding: **(1)** gap closure delayed until higher burnup **(2)** delayed and extended time of soft-contact. However, lower thermal conductivity of SiC increases the cladding temperature drop across the cladding, hence increasing the fuel temperature and fission gas release.

SiC cladding does not creep inward to the fuel, the reduction of pellet-clad gap is only contributed by fuel swelling and thermal expansion. This will allow the gap to remain open longer. Pellet-clad gap creates additional thermal resistance that further

increases the fuel temperature. Higher fuel temperature is generally not a favored fuel performance parameter because it creates larger amount of fission gas release that leads to the ballooning of the fuel rod.

5.1.2 Pellet Cladding Mechanical Interactions

PCMI is initiated after the first contact of pellet and cladding. However, no interfacial pressure is yet being accumulated due to the partial recovery of relocation strain. Hard-contact will eventually occurs after 50% of the relocation strain has been accommodated by fuel swelling. After hard-contact, interfacial pressure accumulates at a rapid rate due to the high elastic modulus of SiC and negligible creep and incapability of plastic deformation. The buildup of interfacial pressure contributes to the large cladding hoop stress. It also induces additional elastic deformation and creep of the fuel pellet that was neglected in FRAPCON's rigid-pellet model.

In conclusion, PCMI analysis using the rigid pellet model may give reasonable stress/strain estimation for a ductile metallic cladding (Zircaloy) with a brittle ceramic fuel (UO_2). However, PCMI analysis of brittle ceramic cladding (SiC), the rigid-pellet model may misrepresent the true stresses induced in the cladding by neglecting the possible fuel deformations.

5.1.3 Better Modeling and Mitigation of Cladding Hoop Stress

Both type of rods experience hard-contact at the higher-burnup test case. The corresponding cladding hoop stresses for SiC cladding at the EOL are 334 and 88 MPa. This high cladding hoop stress must be mitigated before applying it to practical use. The following methods were adapted in this research to provide better modeling and also

mitigation of the hoop stress: (1) creep of the cladding and fuel (2) optimize fuel rod design

(a) Creep of cladding and fuel

The creep behavior of both cladding and fuel is indispensable for relieving the excessive stresses resulting from PCMI. With the assistance of cladding creep, rapid accumulation of Zircaloy cladding hoop stress can be alleviated once the creep rate achieves the fuel swelling rate. This can be explained as a reduced fuel swelling rate. After hard-contact, cladding expansion is controlled by fuel swelling and cladding inward creep. If the cladding creep increases, then the net fuel swelling rate will decrease. This will result in an overall smaller fuel expansion. However, lack of creep in SiC will allow buildup of stresses on the pellet/cladding interface without any mechanisms to retard the fuel swelling.

A better modeling accounting for the stress-induced pellet deformation is discussed for better modeling of the accumulated hoop stress due to hard-contact. Larger fuel surface pressure and higher fuel temperature of SiC cladding induces higher fuel creep rate, which reduces the outward fuel swelling rate. The fuel creep acts similar to the cladding creep, as their main purpose is also to reduce the overall swelling rate. From previous analysis that considers the stress-induced deformations, the radial displacement of the fuel is reduced by 8.8 μm . Reduced fuel deformation will reduce the cladding deformation; therefore the cladding hoop stress is reduced.

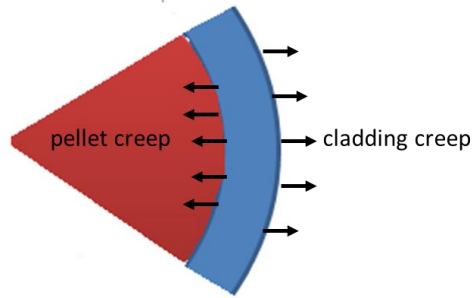


Figure 5.1 Two creep mechanisms for cladding hoop stress mitigation

(b) Fuel Rod Design

Fuel rods with thicker cladding design also decrease the cladding hoop stress. It is shown that increasing the cladding thickness from 0.0572 to 0.1 cm will reduce the EOL hoop stress by 68%. The downside of thicker cladding is the larger thermal resistance, which will increase the fuel temperature by 72 K, therefore, aggravates the fission gas release.

Table 5.2 Results of PCMI mitigation

	Before	After
Thicker Cladding (0.0572 to 0.1 cm)	Reduced Hoop Stress	
	335 MPa	221 MPa
Soft-Pellet Model	Reduced Fuel Radial Deformation	
	79 μm	70.2 μm

PCMI (hard-contact) must be ultimately avoided to ensure the integrity of SiC cladding under high burnup operation due to the large cladding hoop stress. Applying thicker cladding or more creep-susceptible fuel provides an approach to mitigate the large hoop stress, but it also brings drawbacks such as increased fuel temperature, and enhanced fission gas release. An optimized fuel rod design with more accurate modeling is needed for estimate the PCMI effect of ceramic cladding.

REFERENCES

1. GOLDNER, F., DEVELOPMENT STRATEGY FOR ADVANCED LWR FUELS WITH ENHANCED ACCIDENT TOLERANCE, 2012.
2. DOBISESKY, J.P., ET AL., *HIGH BURNUP PWR CORE DESIGN WITH SILICON CARBIDE CLADDING*. TRANSACTIONS OF THE AMERICAN NUCLEAR SOCIETY, 2011. **104**: P. 727-8.
3. K.J. GEELHOOD, W.G.L., C.E. BEYER, FRAPCON-3.4: A COMPUTER CODE FOR THE CALCULATION OF STEADY-STATE THERMO-MECHANICAL BEHAVIOR OF OXIDE FUEL RODS FOR HIGH BURNUP. NUREG/CR-6534, 2011. **VOLUME-2**.
4. ALAM, T., ET AL., *A REVIEW ON THE CLAD FAILURE STUDIES*. NUCLEAR ENGINEERING AND DESIGN, 2011. **241**(9): P. 3658-77.
5. ROVNER, L., G. HOPKINS, AND K.Y. CHEN. CERAMIC MATERIALS FOR FUSION. IN AMERICAN NUCLEAR SOCIETY 1975 WINTER MEETING. (SUMMARIES), 16-21 Nov. 1975. 1975. USA.
6. CECA-002820, NP-MHTGR MATERIAL MODELS OF PYROCARBON AND PYROLYTIC SILICON CARBIDE. CECA CORPORATION, 1993.
7. ALKAN, Z., ET AL. SILICON CARBIDE ENCAPSULATED FUEL PELLETS FOR LIGHT WATER REACTORS. IN INERT MATRIX FUEL 6. 6TH WORKSHOP ON INERT MATRIX FUEL, E-MRS SYMPOSIUM B, 30 MAY-2 JUNE 2000. 2001. UK: ELSEVIER.
8. HASEGAWA, A., ET AL., *CRITICAL ISSUES AND CURRENT STATUS OF SiC/SiC COMPOSITES FOR FUSION*. JOURNAL OF NUCLEAR MATERIALS, 2000. **283-287**(PART I): P. 128-137.

9. ROSS, D.F., JR. AND W.R. HENDRICH. STRENGTH TESTING OF MONOLITHIC AND DUPLEX SILICON CARBIDE CYLINDERS IN SUPPORT OF USE AS NUCLEAR FUEL CLADDING. IN CERAMICS IN NUCLEAR AND ALTERNATIVE ENERGY APPLICATIONS. A COLLECTION OF PAPERS PRESENTED AT THE 30TH INTERNATIONAL CONFERENCE ON ADVANCED CERAMICS AND COMPOSITES, 22-27 JAN. 2006. 2006. HOBOKEN, NJ, USA: JOHN WILEY.
10. SNEAD, L.L. LIMITS ON IRRADIATION-INDUCED THERMAL CONDUCTIVITY AND ELECTRICAL RESISTIVITY IN SILICON CARBIDE MATERIALS. IN 11TH INTERNATIONAL CONFERENCE ON FUSION REACTOR MATERIALS (ICFRM-11), 7-12 DEC. 2003. 2004. NETHERLANDS: ELSEVIER.
11. CANES. *NSUF IRRADIATION OF NOVEL SiC CLADDING FOR ADVANCED LWRs*. AVAILABLE FROM: [HTTP://CANES.MIT.EDU/RESEARCH](http://canes.mit.edu/research).
12. HALLSTADIUS, L., S. JOHNSON, AND E. LAHODA. *CLADDING FOR HIGH PERFORMANCE FUEL*. 2012. LANGFORD LANE, KIDLINGTON, OXFORD, OX5 1GB,
13. SNEAD, L.L., ET AL., *HANDBOOK OF SiC PROPERTIES FOR FUEL PERFORMANCE MODELING*. JOURNAL OF NUCLEAR MATERIALS, 2007. **371**(1-3): p. 329-77.
14. WRIGHT W.V. BARTELS, F.T. IN PROCEEDINGS OF THE CONFERENCE FOR SILICON CARBIDE HIGH TEMPERATURE SEMICONDUCTORS. 1960.
15. OLANDER, D. *NUCLEAR FUELS - PRESENT AND FUTURE*. IN *2010 MRS SPRING MEETING, APRIL 5, 2010 - APRIL 9, 2010*. 2010. SAN FRANCISCO, CA, UNITED STATES: MATERIALS RESEARCH SOCIETY.

16. CARPENTER, D., G. KOHSE, AND M. KAZIMI. MODELING OF SILICON CARBIDE DUPLEX CLADDING DESIGNS FOR HIGH BURNUP LIGHT WATER REACTOR FUEL. IN SOCIETE FRANCAISE D'ENERGIE NUCLEAIRE - INTERNATIONAL CONGRESS ON ADVANCES IN NUCLEAR POWER PLANTS - ICAPP 2007, "THE NUCLEAR RENAISSANCE AT WORK", MAY 13, 2007 - MAY 18, 2007. 2008. NICE, FRANCE: UNAVAILABLE.
17. FEINROTH, H., ET AL. MECHANICAL STRENGTH OF CTP TRIPLEX SIC FUEL CLAD TUBES AFTER IRRADIATION IN MIT RESEARCH REACTOR UNDER PWR COOLANT CONDITIONS. IN CERAMICS IN NUCLEAR APPLICATIONS - 33RD INTERNATIONAL CONFERENCE ON ADVANCED CERAMICS AND COMPOSITES, JANUARY 18, 2009 - JANUARY 23, 2009. 2010. DAYTONA BEACH, FL, UNITED STATES: AMERICAN CERAMIC SOCIETY.
18. W.G. LUSCHER, K.J.G., *MATPRO: MATERIAL PROPERTIES FOR FUEL PERFORMANCE MODELING*. NUREG/CR-7024 PNNL-19417, 2011.
19. CANER, M. AND E.T. DUGAN, *THO2-UO2 ANNULAR PINS FOR HIGH BURNUP FUELS*. ANNALS OF NUCLEAR ENERGY, 2000. **27**(9): p. 759-770.
20. HEJZLAR, P. AND M.S. KAZIMI, ANNULAR FUEL FOR HIGH-POWER-DENSITY PRESSURIZED WATER REACTORS: MOTIVATION AND OVERVIEW. NUCLEAR TECHNOLOGY, 2007. **160**(1): p. 2-15.
21. BROCHARD, J., ET AL., *SPECIFIC FUEL ROD THERMOMECHANICAL STUDIES FOR THE ADVANCED PLUTONIUM FUEL ASSEMBLY CONCEPT*. PROGRESS IN NUCLEAR ENERGY, 2001. **38**(3-4): p. 399-402.

22. HEJZLAR, P., ET AL. THE DESIGN AND MANUFACTURING OF ANNULAR FUEL FOR HIGH POWER DENSITY AND IMPROVED SAFETY IN PWRs. IN 2004 INTERNATIONAL MEETING ON LWR FUEL PERFORMANCE, SEPTEMBER 19, 2004 - SEPTEMBER 22, 2004. 2004. ORLANDO, FL, UNITED STATES: AMERICAN NUCLEAR SOCIETY.
23. YI, Y., M.S. KAZIMI, AND P. HEJZLAR, *THERMOMECHANICAL PERFORMANCE OF HIGH-POWER-DENSITY ANNULAR FUEL*. NUCLEAR TECHNOLOGY, 2007. **160**(1): P. 135-49.
24. LONG, Y., ET AL., *A FISSION GAS RELEASE MODEL FOR HIGH BURNUP THO₂-UO₂ FUEL*. TRANSACTIONS OF THE AMERICAN NUCLEAR SOCIETY, 2001. **85**: P. 54-6.
25. COLLINS, A.K., M.A. PICKERING, AND R.L. TAYLOR, GRAIN SIZE DEPENDENCE OF THE THERMAL CONDUCTIVITY OF POLYCRYSTALLINE CHEMICAL VAPOR DEPOSITED -SiC AT LOW TEMPERATURES. JOURNAL OF APPLIED PHYSICS, 1990. **68**(12): P. 6510-12.
26. MARUYAMA, T. AND M. HARAYAMA. RELATIONSHIP BETWEEN DIMENSIONAL CHANGES AND THE THERMAL CONDUCTIVITY OF NEUTRON-IRRADIATED SiC. IN PROCEEDINGS OF THE 11TH CONFERENCE ON FUSION RESEARCH, DECEMBER 7, 2003 - DECEMBER 12, 2003. 2004. KYOTO, JAPAN: ELSEVIER.
27. SNEAD, L.L., S.J. ZINKLE, AND D.P. WHITE, THERMAL CONDUCTIVITY DEGRADATION OF CERAMIC MATERIALS DUE TO LOW TEMPERATURE, LOW DOSE NEUTRON IRRADIATION. JOURNAL OF NUCLEAR MATERIALS, 2005. **340**(2-3): P. 187-202.
28. BOURGOIN, J.C., *ELECTRONIC EFFECTS ON DEFECT BEHAVIOR IN SEMICONDUCTORS*. RADIATION EFFECTS AND DEFECTS IN SOLIDS, 1989. **111-112**(1-2): P. 29-36.
29. PRICE, R.J., PROPERTIES OF SILICON CARBIDE FOR NUCLEAR FUEL PARTICLE COATINGS. NUCLEAR TECHNOLOGY, 1977. **35**: P. 320-36.

30. HUANG, H. AND N. GHONIEM, A SWELLING MODEL FOR STOICHIOMETRIC SiC AT TEMPERATURES BELOW 1000C UNDER NEUTRON IRRADIATION. JOURNAL OF NUCLEAR MATERIALS, 1997. **250**(2-3): p. 192-9.
31. SNEAD, L.L., T.D. BURCHELL, AND A.L. QUALLS, *STRENGTH OF NEUTRON-IRRADIATED HIGH-QUALITY 3D CARBON FIBER COMPOSITE*. JOURNAL OF NUCLEAR MATERIALS, 2003. **321**(2-3): p. 165-9.
32. GROW, J.M. AND R.A. LEVY, *MICROMECHANICAL CHARACTERIZATION OF CHEMICALLY VAPOR DEPOSITED CERAMIC FILMS*. JOURNAL OF MATERIALS RESEARCH, 1994. **9**(8): p. 2072-8.
33. RUH, R., A. ZANGVIL, AND J. BARLOWE, *ELASTIC PROPERTIES OF SiC, ALN, AND THEIR SOLID SOLUTIONS AND PARTICULATE COMPOSITES*. AMERICAN CERAMIC SOCIETY BULLETIN, 1985. **64**(10): p. 1368-73.
34. GULDEN, T.D., *STACKING FAULTS IN CHEMICALLY-VAPOR-DEPOSITED BETA SILICON CARBIDE*. JOURNAL OF THE AMERICAN CERAMIC SOCIETY, 1971. **54**(10): p. 498-501.
35. TERSOFF, J., MODELING SOLID-STATE CHEMISTRY: INTERATOMIC POTENTIALS FOR MULTICOMPONENT SYSTEMS. PHYSICAL REVIEW B (CONDENSED MATTER), 1989. **39**(8): p. 5566-8.
36. NEWSOME, G., ET AL., *EVALUATION OF NEUTRON IRRADIATED SILICON CARBIDE AND SILICON CARBIDE COMPOSITES*. JOURNAL OF NUCLEAR MATERIALS, 2007. **371**(1-3): p. 76-89.
37. RYSHKEWITCH, E., *COMPRESSION STRENGTH OF POROUS SINTERED ALUMINA AND ZIRCONIA*. AMERICAN CERAMIC SOCIETY -- JOURNAL, 1953. **36**(2): p. 65-68.

38. CARTER JR, C.H., R.F. DAVIS, AND J. BENTLEY, *KINETICS AND MECHANISMS OF HIGH-TEMPERATURE CREEP IN SILICON CARBIDE: II, CHEMICALLY VAPOR DEPOSITED*. JOURNAL OF THE AMERICAN CERAMIC SOCIETY, 1984. **67**(11): p. 732-740.
39. DICARLO, J.A., *CREEP OF CHEMICALLY VAPOUR DEPOSITED SiC FIBRES*. JOURNAL OF MATERIALS SCIENCE, 1986. **21**(1): p. 217-24.
40. EHRLICH, K., IRRADIATION CREEP AND INTERRELATION WITH SWELLING IN AUSTENITIC STAINLESS STEELS. JOURNAL OF NUCLEAR MATERIALS, 1981. **100**(1-3): p. 149-66.
41. PRICE, R.J., PROPERTIES OF SILICON CARBIDE FOR NUCLEAR FUEL PARTICLE COATINGS. NUCLEAR TECHNOLOGY, 1977. **35**(2): p. 320-336.
42. OSBORNE, M.C., ET AL., NEUTRON IRRADIATION EFFECTS ON THE DENSITY, TENSILE PROPERTIES AND MICROSTRUCTURAL CHANGES IN HI-NICALON AND SYLRAMIC SiC FIBERS. JOURNAL OF NUCLEAR MATERIALS, 1998. **253**: p. 67-77.
43. LANNING, D.D., THE POSSIBLE IMPACT OF FUEL PELLET CRACKING ON INFERRED GAP CONDUCTANCE AND FUEL STORED ENERGY. NUCLEAR TECHNOLOGY, 1982. **56**(3): p. 565-74.
44. OGUMA, M., CRACKING AND RELOCATION BEHAVIOR OF NUCLEAR FUEL PELLETS DURING RISE TO POWER. NUCLEAR ENGINEERING AND DESIGN, 1983. **76**(1): p. 35-45.
45. UFFELEN, P.V., *MODELING OF NUCLEAR FUEL BEHAVIOR*. FREDERIC JOLIOU & OTTO HAHN SUMMER SCHOOL ON NUCLEAR REACTORS: PHYSICS, FUEL, SYSTEMS, 2006.

46. STEHEL, H., H. ASSMANN, AND F. WUNDERLICH, *URANIUM DIOXIDE PROPERTIES FOR LWR FUEL RODS*. NUCLEAR ENGINEERING AND DESIGN, 1975. **33**(2): P. 230-260.
47. NUCLEAR SAFETY RESEARCH CENTER, J., FEMAXI-6: CODE SYSTEM FOR LIGHT WATER REACTOR FUEL ANALYSIS 2006.
48. FROST, B.R.T., MATERIALS SCIENCE AND TECHNOLOGY: NUCLEAR MATERIALS PART I. VOL. 10A. 1994.
49. ROBERTS, J.T.A. AND J.C. VOGLEWEDE, *APPLICATION OF DEFORMATION MAPS TO THE STUDY OF IN-REACTOR BEHAVIOR OF OXIDE FUELS*. JOURNAL OF THE AMERICAN CERAMIC SOCIETY, 1973. **56**(9): P. 472-475.
50. SOLOMON, A.A., *RADIATION-INDUCED CREEP OF UO₂*. JOURNAL OF THE AMERICAN CERAMIC SOCIETY, 1973. **56**(3): P. 164-171.
51. BRUCKLACHER, D. AND W. DIENST, *CREEP BEHAVIOR OF CERAMIC NUCLEAR FUELS UNDER NEUTRON IRRADIATION*. JOURNAL OF NUCLEAR MATERIALS, 1972. **42**(3): P. 285-296.